

**A comprehensive simulation study of dissolved Barium and Oxygen
isotope ratio in the Arctic Ocean**

by

Yingkai Sha

B.Sc. Atmospheric Science, Nanjing University of Information Science and Technology, 2014

A THESIS SUBMITTED IN PARTIAL FULFILLMENT
OF THE REQUIREMENTS FOR THE DEGREE OF

Master of Science

in

THE FACULTY OF GRADUATE AND POSTDOCTORAL STUDIES
(Atmospheric Science)

The University of British Columbia
(Vancouver)

March 2017

© Yingkai Sha, 2017

Abstract

The Arctic Ocean freshwater plays important roles in regional and global climate. Dissolved Barium and the Oxygen isotope ratio are two tracers that provide key information on the river runoff and the sea-ice melt water as two Arctic Ocean freshwater components. In this research, an offline tracer model was developed with dissolved Barium and Oxygen isotope ratio modules and appropriate boundary conditions were applied to the Arctic Ocean to simulate the spatial and temporal variations of the two tracers. The tracer model was run from 2002 to 2013 after a 24-year spin-up. The simulation results show reasonable tracer climatology and seasonal cycles, agree well with field observations and the Arctic freshwater cycle. The tracer model was applied to investigate the atmospheric driven freshwater variabilities in the upper 130m through linear trend and Empirical Orthogonal Function (EOF) analysis. The linear trend result shows the increase in the transport of Eurasian runoff from the Makarov Basin to the Beaufort Sea and concurrent with the increase in the winter-spring Arctic Oscillation (AO). The three EOF modes show the role of the dipole anomaly, the interannual impact of the North Atlantic Oscillation (NAO) and the Beaufort Sea anticyclonic anomalous wind, respectively on changing the pathway of the high Barium concentration North American runoff and the impact of the Eurasian runoff along the continental shelves and in the central Arctic. A case study of the Beaufort Gyre freshwater in 2007-2008 revealed the change of Eurasian runoff pathways in three stages with the dipole anomaly and the transport of Eurasian runoff in the developing stage, the strong anti-cyclonic wind in the Beaufort Sea in the mature stage and the weakening of the Beaufort Gyre in the final stage. A linear mixing model result confirms the increase of the Eurasian runoff in the Beaufort Gyre in the winter of 2007.

Preface

This thesis contains details of parameterizations, numerical experiments and analysis of the results undertaken primarily by the author, Yingkai Sha and supported by the GEOTRACES program funded by Climate Change and Atmospheric Research (CCAR). Susan Allen was the supervisor and was involved in the concept formation, interpretation of the results and manuscript edits. A manuscript based on Chapter 3, and Chapter 4 will be submitted for publication in the future.

Table of Contents

Abstract	ii
Preface	iii
Table of Contents	iv
List of Tables	vii
List of Figures	viii
Glossary	xii
Acknowledgments	xiv
1 Introduction	1
2 Background	3
2.1 Arctic Ocean freshwater	3
2.1.1 Freshwater components	3
2.1.2 The indicator: Freshwater Content	4
2.1.3 Freshwater budget and implications	5
2.2 Dissolved Barium	6
2.2.1 The geochemical behavior of dissolved Barium	6
2.2.2 External sources and the utility as a tracer	7
2.3 Oxygen isotope ratio	7
2.3.1 Definition and physicochemical properties	7
2.3.2 Role in the hydrological cycle	8
2.4 Modeling of Arctic freshwater and tracers	9
3 Methodology	10
3.1 Model and regional Arctic configuration	10
3.2 Tracer parameterizations	11
3.2.1 Riverine tracer input	11

3.2.2	Sea-ice and precipitation	15
3.3	Configuration of numerical experiments	16
3.4	Methods and data for analyzing the results	17
3.4.1	Data applied in model parameterization and evaluations	18
3.4.2	Methods in the model evaluation	19
3.4.3	Physical calculations	19
3.4.4	Statistical methods	21
3.4.5	Indices applied in the research	21
3.4.6	Linear mixing model	21
4	Results	24
4.1	Climatology and seasonal cycles	24
4.1.1	Dissolved Barium	24
4.1.2	Oxygen isotope ratio	27
4.2	Data model comparisons	29
4.2.1	Dissolved Barium	29
4.2.2	Oxygen isotope ratio	30
4.3	Linear trends of tracers and Arctic freshwater	32
4.4	Tracer anomaly patterns and freshwater variability	34
4.4.1	Mode I: Dipole anomaly	34
4.4.2	Mode II: The interannual effect of NAO	38
4.4.3	Mode III: The Beaufort Sea high	41
4.5	Application: A case study of Beaufort Gyre 2007-2008	44
4.5.1	Evolution of the FWC anomaly	45
4.5.2	Linear mixing model	50
5	Discussion	52
5.1	Model configuration and operations	52
5.2	Tracer parameterizations, model output and evaluations	52
5.2.1	dissolved Barium	52
5.2.2	Oxygen isotope ratio	54
5.3	Freshwater, tracers and atmospheric driving factors	54
5.4	Insights from the Beaufort Gyre case study	55
5.5	Summary	55
6	Conclusions	56
6.1	Research questions	56
6.2	Contributions to the existing knowledge	57
6.2.1	The Canadian Arctic GEOTRACES Program	57
6.2.2	Arctic Ocean freshwater studies	57

6.3	Future research	58
	Bibliography	60
A	Climatology fields of the physical model	70
B	Statistical methods	72
B.1	Correlation	72
B.2	Composite anomaly	73
B.3	Linear regression and trends	73
B.3.1	Least squares method	73
B.3.2	Significance test	74
B.4	Empirical Orthogonal Function (EOF)	74
B.4.1	Spatial pattern and principal component	74
B.4.2	Explained variance	76
B.4.3	Rule of thumb	76
B.4.4	Spectral analysis	77
C	The derivation of wind stress curl	78
D	Atmospheric tele-connection patterns and CGRF indices	79

List of Tables

Table 3.1	The riverine Oxygen isotope ratio input of the tracer scheme	15
Table 3.2	Meta data of the field observations	18
Table 3.3	Tracer end-member settings in Beaufort Sea	23
Table 4.1	Total annual riverine dissolved Barium input in this research and the estimate from Guay and Falkner [1998]	27
Table 4.2	Mean bias and NRSMD of dissolved Barium comparisons	29
Table 4.3	Mean bias and NRSMD of Oxygen isotope ratio comparisons	31

List of Figures

Figure 2.1	Map of the Arctic Ocean with the bathymetry (shaded), continental shelves (black text), seas (black, italic), basins (white, bold) and ridges (white, italic).	4
Figure 3.1	MY_TRC open boundaries (in black) and internal grid (in dark gray). Grid of ANHA4 experiments covers all the MY_TRC domain (both black and dark gray) and extends to the Atlantic Ocean (light gray).	10
Figure 3.2	The classification of river estuaries in the Arctic Ocean. Rectangular frame on the bottom right is a zoom in CAA	12
Figure 3.3	Normalized ensemble seasonal cycle of dissolved Barium for the six largest Arctic rivers. The grey solid line is the ensemble result. Black markers indicate all ensemble members. Blue bars show the standard deviation. The hatch shows the “drop down” signal.	13
Figure 3.4	The seasonal cycle of dissolved Barium input in all parameterized Arctic rivers. . .	14
Figure 3.5	Domain-wide mean dissolved Barium (a) and Oxygen isotope ratio (b) in two spin-up experiments and the formal run. Each of the spin-up experiment was run under AHNA4-EXH005 forcing from 2002 to 2013.	17
Figure 3.6	The ANHA4 grid based transects in the the Baffin Bay and Hudson Bay (a), Fram Strait and Barents Sea openings (b), and the Bering Strait (c).	20
Figure 3.7	The 2002-2013 mean ANHA4-EXH005 velocities above 130 m and regions that define the TDS intensity (orange) and the Beaufort Gyre intensity (cyan) indices. . .	22
Figure 4.1	Simulated 2002-2013 climatology state of dissolved Barium above 130 m. (a) is the annual mean state. (b) is the difference between the mean state in May and (a). (c) is the domain-wide mean dissolved Barium monthly mean timeseries. (d) is the seasonal cycle of (c).	25

Figure 4.2	Simulated dissolved Barium fluxes through different pathways (a) and their seasonal cycles (b). Negative in (a) means out flux and the black line is the net result. (c) and (d) are simulated riverine dissolved Barium input and its seasonal cycle. (d) shows the time range of 2002-2008, and the 2007-2008 pattern was repeated in the 2009-2013 period. (e) is the riverine dissolved Barium input minus the net in/out flux. (f) is the seasonal cycle of (e). The calculation of (a-d) is based on equation (3.11) and equation (3.12). Rivers input on the southern part of transects (figure 3.5) is small and not considered.	26
Figure 4.3	Simulated 2002-2013 climatology state of Oxygen isotope ratio at the surface (1.05 m) (a) is the annual mean. (b) is the histogram between the mean surface Oxygen isotope ratio and the sea surface salinity. The shade shows the number of points in each hist bin, the black box indicates the sea-ice melt water. (c) is the Oxygen isotope ratio timeseries that has been averaged in the hatched region. (d) is the seasonal cycle of (c). (e) is the domain-wide mean surface Oxygen isotope ratio. (f) is the seasonal cycle of (e).	28
Figure 4.4	The model output of dissolved Barium comparing with BGEP 2003-2005 (a), CBL32PZ 2002 (b), NPEO 2004-2008 and 2013 (c), ARK-XXII/2 2007 (d) and HLY0301 2003 (e) observations. (f) is the timeseries comparison of BGEP data. (g) is the timeseries comparison of NPEO data. (h) shows the locations of all samples. Two red circles are the regions that calculate the model mean, minimum and maximum in (f) and (g).	30
Figure 4.5	Same as figure 4.4 but for Oxygen isotope ratio and without ARK-XXII/2 data. . .	31
Figure 4.6	The linear trends of FWC (a), sea surface height and ocean velocities (b), dissolved Barium (c) and Oxygen isotope ratio (d). All variables except sea surface height were averaged from 0 to 130 m depth. Dotted regions have trends that have passed a two-sided t-test. Negative/positive sea surface height in (b) delineates regions of cyclonic/anti-cyclonic surface geostrophic flow. The velocity trends shown imply that the eastern side of the Beaufort Gyre and the TDS are intensifying.	33
Figure 4.7	The October to next year May averaged AO indices and the linear trend from 1950 to 2015. The orange line is the NOAA-CPC AO index, the brown solid line is the CGRF AO index. The dark green solid line is the result of linear regression with the trend of 0.0097. The R-square is 0.098 and the trend passed 0.01 two-sided t-test. .	34
Figure 4.8	The FWC EOF mode one spatial pattern (left), PC (top right green solid line) and the spectral energy of PC (bottom right). The gray line on the top right is the TDS intensity estimated by the mean horizontal speed of surface ocean currents in the hatched region (see section 3.4.5). The red dashed line is the 95% red noise test confidential interval.	35

Figure 4.9	The composite anomalies for mode one PC. Composite anomalies are difference between high phase and low phase (section 3.4.4). sea level pressure, 10 m winds (a), wind stress, wind stress curl (b), sea surface height, ocean velocities above 130 m (c) and E-P flux (d). Dotted regions have composite anomalies pass the 0.05 level t-test.	36
Figure 4.10	The composite anomaly of dissolved Barium (a) and Oxygen isotope ratio (b) in mode one PC and averaged above 130 m. Hatched regions in (a-b) are shallower than 30 m. Dotted regions in (a-b) have composite anomaly pass the 0.05 level two-sample t-test. (c) is the sketch of anomalous flow pattern, both in the lower atmosphere (top plane) and the surface ocean (lower plane). On the upper plane, the dipole anomaly with enhanced high pressure over the Beaufort Sea and enhanced low pressure over the Eurasian Side. Wind barbs show the anomalous winds. On the lower plane, circles show the major anomalous currents; ① and ② transports the Eurasian runoff to the Makarov Basin; ③ is the anomalously strong TDS; ④ indicates the weak CAA - Baffin Bay transport and ⑤ is the intensified Beaufort Gyre.	37
Figure 4.11	The FWC EOF mode two spatial pattern (left), PC (top right green solid line) and the spectral energy of PC (bottom right). On the top right plot, the gray dashed line and gray solid line are the 1-year moving averaged NOAA-CPC NAO and CGRF NAO indices (see section 3.4.5). The red dashed line is the 95% red noise test confidential interval.	39
Figure 4.12	Same as figure 4.9, but for mode two	40
Figure 4.13	Same as figure 4.10, but for mode two. (c) is the sketch of anomalous flow pattern. In the the lower atmosphere (top plane), the NAO-like anomaly with positive pressure over the North Atlantic and enhanced low pressure over the central Arctic/-Nansen Basin. In the surface ocean (lower plane), circles show the major anomalous currents; ① and ② are the intensified CAA - Baffin Bay transport with a weak Beaufort Gyre; ③ is the transport of Laptev Sea runoff; ④ is the accumulation of runoff water in the Makarov Basin.	41
Figure 4.14	The FWC EOF mode three spatial pattern (left), PC (top right green solid line) and the spectral energy of PC (bottom right). The gray line on the top right plot is the Beaufort Gyre intensity estimated as the maximum sea surface height in the Beaufort Sea (see section 3.4.5). The red dashed line is the 95% red noise test confidential interval.	42
Figure 4.15	Same as figure 4.9, but for mode three	43

Figure 4.16	Same as figure 4.10, but for mode three. (c) is the sketch of anomalous flow pattern. In the the lower atmosphere (top plane), the enhanced low pressure over the North Atlantic and Eurasian side of the Arctic intensifies the Beaufort Gyre. In the surface ocean (lower plane), circles show the major anomalous currents; ① is the weak CAA - Baffin Bay transport; ② and ③ are the anticyclonic flow in the Beaufort Sea and the northern side of New Siberian Island; ④ is the transport of East Siberian Sea runoff.	44
Figure 4.17	The Beaufort Gyre freshwater anomaly above 130 m as volume (red, left axis) and the Beaufort Gyre intensity (black, right axis, see section 3.4.5), the hatched region is the time span of the case study.	45
Figure 4.18	2007 June-August mean sea level pressure and 10 m wind anomaly (a). August-October mean sea surface height, ocean velocities (b), FWC (c), $E - P$ (d), dissolved Barium (e) and Oxygen isotope ratio (f) anomalies.	46
Figure 4.19	Same as figure 4.18, but for December-February mean, no $E - P$ and $\delta^{18}\text{O}$ anomalies.	48
Figure 4.20	Same as figure 4.18, but for 2008 and no $E - P$ and $\delta^{18}\text{O}$ anomalies.	49
Figure 4.21	The timeseries of Eurasian (red) and North American (black) runoff fractions in the Beaufort Gyre (as defined in figure 3.7) from 0-130 m depth. The shade is the variation range. The time span of the case study is hatched.	50
Figure A.1	CGRF 2002-2013 mean winter (DJF) and summer (JJA) sea level pressure and 10m-wind.	70
Figure A.2	ANHA4-EXH005 2002-2013 mean sea surface height, ocean velocities (a) and FWC relative to the 34.8 salinity (b) above 130m. The dashed line in (b) is the isoline of 2002-2013 mean March sea-ice larger than 70%; the hatch is the mean September sea-ice larger than 70%.	71
Figure D.1	Spatial patterns of sea level pressure EOF modes (a-c), timeseries in dark red are the PCs. NOAA-CPC AO and NAO indices were plotted as black dashed lines. . .	79

Glossary

AGRO	Arctic Great River Observatory
ANHA4	Arctic and North Hemisphere Atlantic 1/4 degree
AO	Arctic Oscillation
BGEP	Beaufort Gyre Exploration Project
CAA	Canadian Arctic Archipelago
CGRF	<u>C</u> anadian Meteorological Centre <u>G</u> lobal Deterministic Prediction System <u>R</u> eforecasts
EOF	Empirical Orthogonal Function
FWC	Freshwater Content
GLORYS	<u>G</u> lobal Ocean Reanalyses and Simulations
LIM2	Louvain-la-Neuve Sea Ice Model version 2
NAO	North Atlantic Oscillation
NPEO	North Pole Exploration Observatory
NOAA	National Oceanic and Atmospheric Administration
CPC	Climate Prediction Center
NRMSD	Normalized Root Mean Square Deviation
PARTNERS	Pan-Arctic River Transport of Nutrients, Organic Matter, and Suspended <u>S</u> ediments
PC	Principal Component

- SCARFS** Small Canadian Arctic River Flows
- TDS** Transpolar Drift Stream
- NEMO 3.4** Nucleus for European Modelling of the Ocean version 3.4
- VSMOW** Vienna Standard Mean Ocean Water

Acknowledgments

Here my sincere thanks to my M.Sc supervisor Dr. Susan Allen for providing me the opportunity to pursue my new research in her GEOTRACES group. She encourages me to practice my own ideas and I feel fully respected as a young researcher. Also, thanks Susan for both your knowledge about NEMO and your critical thinking on scientific problems which make my research moving forward.

Thanks to Xianmin Hu and Dr. Paul Myers in University of Alberta for providing me physical oceanographic simulation results in the Arctic Ocean. Xianmin's help on the offline model configuration was important in my research.

Thank you Dr. Phil Austin and Dr. Roland Stull for all the help in my courses, TA, and sharing opinions on my scientific questions which promoted my enthusiasm on the atmospheric science.

Thank you to Cindy Yu and Melanie Grenier as members in Allen's GEOTRACES group for the discussion in the weekly group meeting. Thanks to everyone in the office and everyone in Allen's research groups in the past two years for staying together and sharing our good memories.

Finally, thanks to my parents, friends and roommates for their daily concerns and contacts.

- Yingkai Sha

Chapter 1

Introduction

The hydrological cycle plays a central role in the earth climate system, of which Arctic Ocean is an important member. The Mediterranean structure of the Arctic Ocean [Aagaard et al., 1985] plus the large amount of freshwater input from Arctic rivers, Pacific inflow, precipitation and sea-ice melt, makes Arctic the most freshwater-influenced of all oceans [Aagaard et al., 1981, Carmack et al., 2016]. The increase of Arctic Ocean freshwater in the past decade [McPhee et al., 2009, Proshutinsky et al., 2009, Rabe et al., 2011] has a strong impact on the stratification state [Aagaard and Carmack, 1989, 1994], Arctic sea-ice cover [Polyakov et al., 2013] and ecological systems [Tremblay and Gagnon, 2009]. In addition, the increased Arctic Ocean freshwater export, which participates in the dense water formation in the Greenland, Iceland, Norwegian and Labrador seas, affects the overturning circulation and is thus of global importance [Dickson et al., 1988, Holland et al., 2001, Weaver et al., 1993]. Arctic freshwater has different components, including runoff, Pacific inflow, sea-ice melt and precipitation. It is necessary to track the spatial and temporal variability of different freshwater components to further investigate their climatological and environmental impacts.

For this objective, several physical and chemical tracers, including salinity, alkalinity (e.g. Yamamoto-Kawai et al. [2005]), dissolved Barium (e.g. [Falkner et al., 1994], Nitrate and Phosphate (e.g. Yamamoto-Kawai et al. [2008]) and Oxygen isotopes (e.g. Ekwurzel et al. [2001], Schlosser et al. [2002]) have been measured and analyzed since the 1980s to uncover the distribution and residence time of different freshwater components. In the meantime, with the development of ocean general circulation models, simulation studies were widely applied to investigate the variability of Arctic Ocean freshwater (e.g. Holland et al. [2006]). The coupling of these two approaches: freshwater tracer simulation, was impeded in the past due to lack of data. Remarkable work from Jahn et al. [2010] shows that, simulated freshwater tracers provide unique information on the variability of freshwater components and large-scale atmospheric circulation. Work of Manizza et al. [2009] on the other hand, shows the possibility of modeling certain bio-geochemical processes in a numeric system.

In this research, with the assistance of field measurements and insights from other tracer modeling research, a simulation study of two freshwater tracers: dissolved Barium and Oxygen isotope ratio is presented. The whole simulation was done by a newly developed tracer parameterization scheme with given physical oceanographic states from 2002 to 2013. The model output was analyzed, compared with

field measurements and used to investigate the underlying dynamics of the Arctic Ocean freshwater. In general, this research answers the following questions:

1. How can oceanic distributions of dissolved Barium and Oxygen isotope ratio be simulated in a numeric model?
2. What are the distribution and statistical features of the simulated tracers and how does the model output compare with field measurements?
3. How does atmospheric variability change the freshwater content in the Arctic?

In the coming pages, chapter 2 contains background information about Arctic Ocean freshwater, modeled tracers and previous research on numeric simulations in this field. Chapter 3 introduces the methodology part, includes model configuration, parameterizations, methods and data applied for the analysis of the output. In chapter 4, all the results are shown, including the climatology, seasonal cycle, model evaluations, linear trends, anomaly patterns and a case study. Chapter 5 gives the discussion and chapter 6 is the conclusions.

Chapter 2

Background

2.1 Arctic Ocean freshwater

2.1.1 Freshwater components

The topography of the Arctic Ocean contains of about half continental shelves and half ridges and basins. The connections between the Arctic Ocean and other ocean basins through Bering Strait (Pacific Ocean), Fram Strait, Barents Sea openings and Davis Strait (Atlantic Ocean) are all limited in horizontal and vertical scale (figure 2.1). These two factors make the Arctic Ocean relatively isolated and to behave like the Mediterranean sea [Aagaard et al., 1985].

Even through the Arctic Ocean contains only 1% of the global volume of sea water and 3% of the world ocean surface, it receives 13% of the world river flow [Dai and Trenberth, 2002, Vörösmarty et al., 2000]. The net precipitation over the open ocean, sea-ice melt and salinity deficient Pacific inflow provide additional freshwater. The input of these freshwater sources can be summarized as “freshwater components”. The spatial distribution of freshwater components in the Arctic Ocean is not uniform. In total, the biggest freshwater reservoir is the Beaufort Gyre [Proshutinsky et al., 2002, 2009], the North American side of the Arctic contains more freshwater than the Eurasian side. According to Yamamoto-Kawai et al. [2005], in 1929-2002, the highest sea-ice melt component was located in Barents and Kara Seas, meanwhile the sea-ice melt fraction in Canada Basin is negative, overshadowed by the ice transport. The Canada Basin - Baffin Bay and the Chukchi Sea have high fractions of runoff, precipitation and Pacific inflow (described as “other freshwaters” in Yamamoto-Kawai et al. [2005]).

The temporal change of freshwater components has linkages with other processes in the climate system on different complexity levels. For example, Pacific origin freshwater input depends on the Bering Strait inflow. The net precipitation at the north pole is affected by processes varying from regional evaporation increase [Bintanja and Selten, 2014] to enhanced polar ward moisture transport [Bengtsson et al., 2011] and anthropogenic greenhouse gases and aerosols [Min et al., 2008]. The river discharge is affected by land surface processes since it is a term in the terrestrial water budget in the drainage basin (e.g. Landerer et al. [2010] for Eurasian runoff). The sea-ice melt freshwater release is

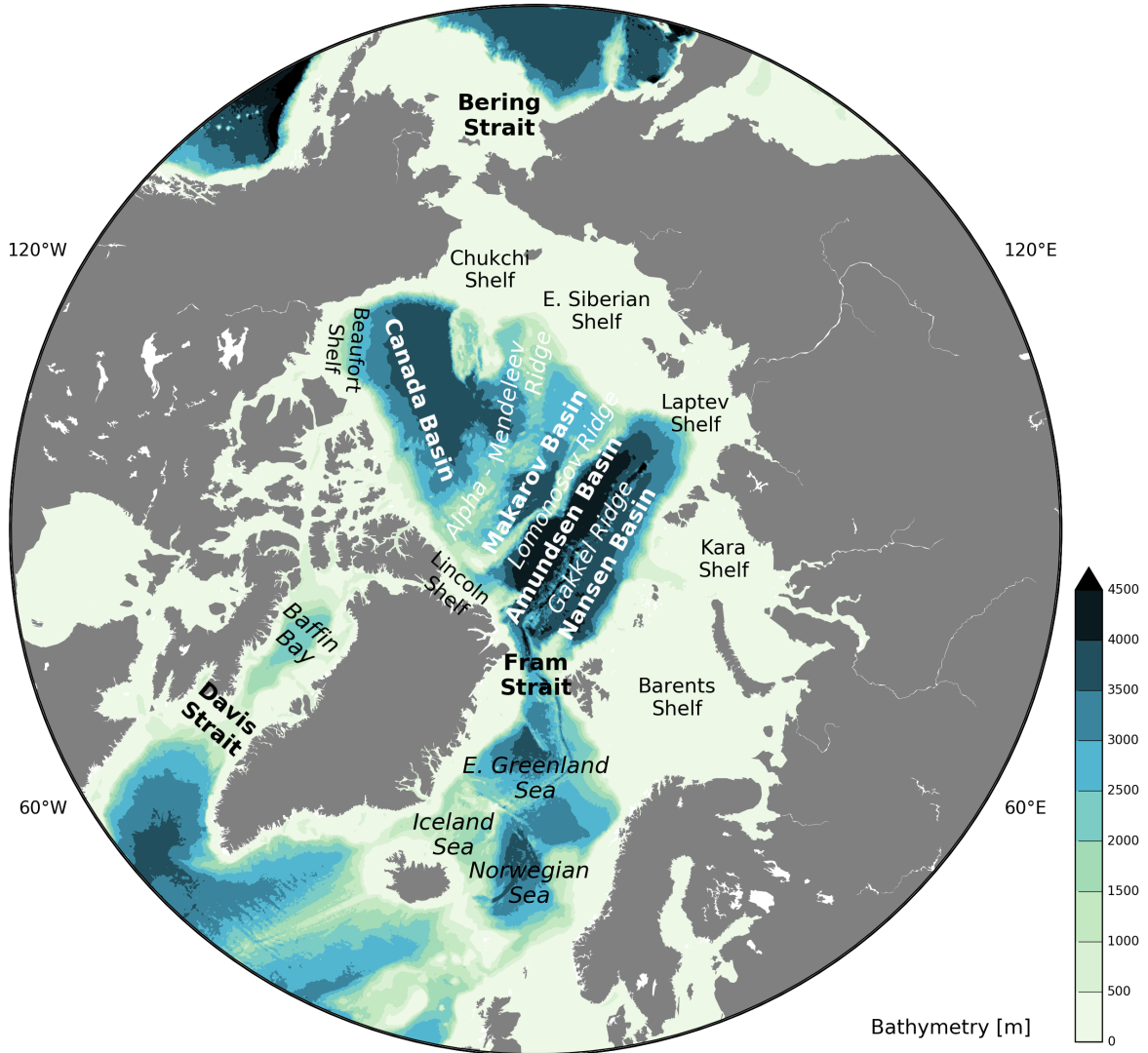


Figure 2.1: Map of the Arctic Ocean with the bathymetry (shaded), continental shelves (black text), seas (black, italic), basins (white, bold) and ridges (white, italic).

affected by the seasonal freeze-thaw cycle [Parkinson and Cavalieri, 1989], ice-albedo feedback [Curry et al., 1995] and atmospheric oscillation patterns (e.g. Arctic Oscillation (AO), Rigor and Wallace [2004]; dipole anomaly, Wang et al. [2009]; North Atlantic Oscillation (NAO), Deser et al. [2000]).

2.1.2 The indicator: Freshwater Content

Freshwater Content (FWC) measures the relative abundance of the freshwater in a certain depth range based on a salinity reference. In the Arctic Ocean, following the choice of Aagaard and Carmack [1989], equation (2.1) shows the calculation of FWC from the surface to depth z .

$$FWC = \int_0^z \left(1 - \frac{S(z)}{34.8}\right) dz \quad (2.1)$$

Here 34.8 is the salinity reference using the practical salinity scale [UNESCO et al., 1981]. The choice is consistent with other previous research (e.g. Aagaard et al. [1985], Jackson et al. [2011], Morison et al. [2012]). FWC has units of m, which means it is the vertical span of zero salinity water above pure reference salinity water. By multiplying with its correspond surface area, FWC can be converted to the volume of freshwater. Equation (2.1) has been widely used in observational (e.g. Rabe et al. [2011]) and modeling (e.g. Jahn et al. [2010]) studies. Its advantage is that, it is constrained by the dynamics in the system, since the calculation directly relates to the stratification. A limitation of it could be the representativeness of the reference salinity [Carmack et al., 2008].

In this research, the choice of the depth is $z = 130$ m which in general captures the freshwater above the halocline layer (e.g. in Makarov Basin, the estimation by Steele and Boyd [1998] is 117 m) and shows good response to the atmospheric forcing. For the numeric calculation of FWC, equation (2.1) is discretized onto the model grid (see section 3.1) and the integral was approximated by trapezoidal quadrature.

2.1.3 Freshwater budget and implications

The estimation of the Arctic freshwater budget, specifically, the balance between freshwater sources and sinks, started in the 1960s [Mosby, 1962]. Then based on FWC as a standardized variable, remarkable works continued from the 1980s to 2015 [Aagaard and Carmack, 1989, Haine et al., 2015, Serreze et al., 2006]. To summarize, river runoff is the biggest component of freshwater input. Comparing the gauge measurements [Lammers et al., 2001] and the 2000-2010 study [Haine et al., 2015], high discharge Eurasian rivers are the biggest fluvial freshwater input ($1813 \text{ km}^3\text{yr}^{-1}$ Eurasian runoff v.s. $4200 \pm 420 \text{ km}^3\text{yr}^{-1}$ total freshwater input). Pacific inflow through Bering Strait is the second largest Arctic freshwater source; it has practical salinity lower than 34.8 because it has mixed with Bering Sea runoff (i.e. Yukon River, Woodgate and Aagaard [2005]). Net precipitation is the other Arctic freshwater source and is the input from the atmosphere.

Eurasian freshwater mainly flows into the Transpolar Drift Stream (TDS), heading toward Fram Strait, and North American freshwater either circles in the Beaufort Gyre and then moves on to the TDS or goes through the Canadian Arctic Archipelago (CAA) - Baffin Bay route from the Beaufort Shelf. The tracer measurement based estimate of runoff transport time from the East Siberian Sea to Fram Strait through the TDS is 2-3 years [Van Der Loeff et al., 1995] and the Eurasian runoff residence time on average is 3.5 ± 2 years [Schlosser et al., 2002]. The freshwater export via Fram Strait is slightly higher than Davis Strait [Haine et al., 2015, Serreze et al., 2006]. The liquid phase export prior to 1989 was estimated to be lower than the ice phase [Aagaard and Carmack, 1989] but then to be higher in the 21st century [Haine et al., 2015, Serreze et al., 2006], which potentially illustrates the Arctic sea-ice decline and the compensation of ice-phase export decrease by liquid-phase export increase [Serreze et al., 2007]. The residual of the Arctic Ocean freshwater budget in 2000-2010 was estimated as $1200 \pm 730 \text{ km}^3\text{yr}^{-1}$ [Haine et al., 2015] which implies an accumulation of surface Arctic freshwater in the past decade [White et al., 2007].

Arctic freshwater plays an important role in ocean, atmosphere and ecological systems. The ex-

istence of surface freshwater causes salt stratification in the Arctic Ocean. This stratification forms a cold halocline layer in the subsurface which hinders the upward diffusive heat flux and thermally driven convection from the Atlantic layer, preserves the Arctic sea-ice [Polyakov et al., 2013] and affects the ice-albedo feedback [Aagaard and Carmack, 1989, 1994].

Arctic freshwater is also an important factor on marine productivity. Terrestrial origin freshwater flushes dissolved and particulate materials into the river estuaries, which is then further advected into the Arctic Ocean and provides nutrients for phytoplankton growth (e.g. Dittmar and Kattner [2003]; also see Klunder et al. [2012] for dissolved iron). The Pacific origin freshwater is enriched in phosphate, plays an import role in the biological nitrogen fixation and benefits the productivity in both Arctic and Atlantic Ocean [Yamamoto-Kawai et al., 2006]. Also, as previously mentioned, Arctic freshwater causes salt stratification. This stratification blocks nutrient supply from the deep water and is thus a negative factor on marine productivity [Tremblay and Gagnon, 2009].

The Arctic Ocean freshwater goes to the North Atlantic Ocean through Fram Strait, Davis Strait and Barents Sea openings, in both liquid-phase and ice-phase [Aagaard and Carmack, 1989, Haine et al., 2015, Serreze et al., 2006]. This freshwater transport affects the stratification of the water column in the sensitive deep water formation regions of the Greenland, Iceland, Norwegian and Labrador seas, affects the Overturning Circulation [Dickson et al., 1988, Holland et al., 2001, Weaver et al., 1993] and therefore the global climate [Zickfeld et al., 2007].

2.2 Dissolved Barium

2.2.1 The geochemical behavior of dissolved Barium

Dissolved Barium (Ba_d) is a type of bio-intermediate element which in general behaves like hard-part nutrients [Chan et al., 1977, Falkner et al., 1993]. In many parts of the world oceans, dissolved Barium concentration has a strong correlation with dissolved Silicon and alkalinity [Bacon and Edmond, 1972, Chan et al., 1977]. Different from either Silicon which is a bio-limiting element and has almost zero concentration in the surface and alkalinity which reflects the Calcium Carbonate ($CaCO_3$) cycle and is only slightly affected by biological activities, dissolved Barium is depleted in the surface but still measurable and is enriched along the deep advective flowline [Chan et al., 1977, Falkner et al., 1993]. The main reason for this depletion is the uptake of Barium at the surface as barite ($BaSO_4$). The newly formed barite is associated with biological particulate matter on the micro-scale and sinks in the ocean. During the sinking process, some of the biological particulate matter decomposes and releases barite which results in a Barium maxima in the subsurface, but most of the barite reaches the sediments and then can be mobilized back to the ocean by remineralization [Bishop, 1988, Dymond et al., 1992, Falkner et al., 1993, 1994]. Research shows that barite formation could be induced by diatoms' Barium accumulation behavior [Esser and Volpe, 2002]. Acantharia and siliceous radiolaria collect Barium in their celestite ($SrSO_4$) shells, and the sinking of these shells also contributes to vertical Barium cycling [Bernstein et al., 1992, 1998]. The residence time of Barium was estimated as 1×10^4 years [Libes, 2011].

2.2.2 External sources and the utility as a tracer

River input (e.g. Arctic Ocean, Guay [1997], Guay and Falkner [1998]) and hydrothermal venting (e.g. East Pacific, Von Damm et al. [1985]) are the main external sources of Barium to the world oceans. Hydrothermal Barium is thought to precipitate inorganically as barite around hot spring sources in the mid-ocean ridge systems [Von Damm et al., 1985]. For the fluvial input, Barium in the river-borne clays will be desorbed by exchange with other cations in the seawater and thus the dissolved Barium concentration increase in the river estuaries. [Edmond et al., 1978, Falkner et al., 1993, Li and Chan, 1979].

Dissolved Barium was first posed as a tracer of Arctic river and halocline water by Falkner et al. [1994]. Then the on-going field measurements in Beaufort Sea, Chukchi Sea, Laptev Sea and Eurasian marginal seas found that North American rivers like Yukon and Mackenzie have dissolved Barium concentration significantly higher than major Eurasian rivers. Therefore, dissolved Barium is able to separate North American runoff from Eurasian runoff. [Guay, 1997, Guay and Falkner, 1997, 1998, Taylor et al., 2003]. Since the “background” surface dissolved Barium level in the Arctic Ocean is lower than both Eurasian and North American runoff, dissolved Barium also acts as a proxy of Arctic runoff water in general [Falkner et al., 1994].

Dissolved Barium was described previously as a quasi-conservative tracer in the Arctic Ocean since its biological modification above the halocline can be roughly averaged out over a long timescale [Taylor et al., 2003]. However, with the sea-ice decline in the past decade [Comiso et al., 2008], the increase of primary production in the Arctic Ocean, especially continental shelves [Arrigo et al., 2008] causes concerns regarding the conservative behavior of Barium [Abrahamsen et al., 2009]. According to Roeske et al. [2012], the biological Barium uptake and remineralization may undermine the conservative behavior of Barium, and only if the effect of riverine input is stronger than the biological signal, can the separation between North American and Eurasian runoff can be done unequivocally. In general, dissolved Barium is still a useful tracer of riverine freshwater in the Arctic Ocean but should be used with care in high productivity regions.

2.3 Oxygen isotope ratio

2.3.1 Definition and physicochemical properties

Naturally Oxygen has three stable isotopes in water (H_2O), Oxygen-16 (^{16}O), Oxygen-17 (^{17}O) and Oxygen-18 (^{18}O) with abundances of 99.76%, 0.04% and 0.2%. Considering the greater mass difference between Oxygen-16 and Oxygen-18, the term “Oxygen isotope ratio” is usually taken as $^{18}\text{O}/^{16}\text{O}$ [Rohling, 2013]. The way to quantitatively estimate the abundance of a minor isotope in water is to compare the sample with a standard, and the comparison result is known as “ δ ”. For the Oxygen isotope ratio, its form in δ is defined in equation (2.2) [Dansgaard, 1964].

$$\delta^{18}\text{O} = \left(\frac{\frac{^{18}\text{O}}{^{16}\text{O}}_{sam}}{\frac{^{18}\text{O}}{^{16}\text{O}}_{std}} - 1 \right) \times 1000\text{‰} \quad (2.2)$$

Here parts per thousand (‰) is the unit, subscript *sam* means the sample and *std* is the standard based on Vienna Standard Mean Ocean Water (VSMOW), which is 2005.20 ± 0.43 ppm of $^{18}\text{O}/^{16}\text{O}$. A positive $\delta^{18}\text{O}$ means the enrichment of heavier Oxygen-18 and vice versa.

Since all Oxygen isotopes have the same number of protons and electrons, they behave in the same way in chemical reactions [Rohling, 2013]. However, Oxygen isotopes can be differentiated by their mass and vibration energy difference. The separation of isotopes between substances with different isotopic compositions is called “isotopic fractionation” [Rohling, 2013]. In detail, the fractionation can be divided into the equilibrium fraction and the kinetic fraction. Equilibrium fractionation happens during phase changes in which heavier molecules (i.e. H_2^{18}O) prefer to stay in the more condensed phase. Kinetic fractionation on the other hand breaks the equilibrium isotopic distribution and is mostly caused by unidirectional processes (e.g. molecular diffusion, [Craig and Gordon, 1965]).

2.3.2 Role in the hydrological cycle

In the global hydrological cycle, isotopic fractionation occurs in evaporation, atmospheric water vapor transport, precipitation and oceanic phase changes such as sea-ice melt. Examining the main response in each of the process contributes to the understanding of the Oxygen isotope ratio as a freshwater tracer in the Arctic Ocean.

During the evaporation, lighter molecules (i.e. H_2^{16}O) have lower vibration energy, higher vapor pressure, and are easier to be evaporated into the atmosphere. Meanwhile heavier molecules tend to stay in the liquid phase and thus separation occurs. The equilibrium fractionation during evaporation is thought to decrease with increasing temperature in an exponential relation [Majoube, 1971]. Molecular diffusion, a kinetic fractionation process, also plays a role in enhancing the separation at the air-sea interface [Craig and Gordon, 1965]. The intensity of molecular diffusion during evaporation was found to be negatively related with the boundary layer humidity [Craig and Gordon, 1965, Rohling, 2013].

Precipitation includes a phase change from atmospheric water vapor to rain droplets. Due to the high humidity in the cloud, equilibrium fractionation is the only important fractionation process in this case. Since the heavier Oxygen-18 has lower vibration energy, it tends to go into the droplets and leaves the cloud. Thus, during meridional atmospheric vapor transport, heavier Oxygen-18 is precipitated and lighter Oxygen-16 accumulates. When the air finally reaches high latitudes, the Oxygen-18 depletion can actually be measured in the precipitated water. Since the precipitation strongly influences the terrestrial water budget, the Oxygen-18 depletion can also be found in high latitude rivers. Based on field measurements at the North Pole, the precipitation and runoff (together called “meteoric water”) Oxygen isotope ratio value is about -20‰ , significantly lower than mid, low latitude cases (e.g. $-8.8 - 7.1\text{‰}$ for Yellow River and Yangtze River, Zhang et al. [1990]).

In the Arctic Ocean, another factor that contributes to the variability of the Oxygen isotope ratio is the sea-ice freeze-thaw cycle. The equilibrium fractionation during sea-ice formation concentrates heavier Oxygen-18 into the ice, and releases it during sea-ice melt. Since high latitude meteoric water has low Oxygen isotope ratio values, but sea-ice melt water has Oxygen isotope ratios higher than the surface ocean, Oxygen isotope ratio has the ability to separate sea-ice melt water from meteoric water

in a $\delta^{18}\text{O}$ -Salinity graph. Thus, considering that Oxygen isotope ratio is conservative if the water is not evaporated, it is widely used as a tracer of sea-ice melt water in the Arctic Ocean (e.g. [Ekwurzel et al., 2001, Macdonald et al., 2002, Östlund and Hut, 1984, Yamamoto-Kawai et al., 2005, 2008]).

2.4 Modeling of Arctic freshwater and tracers

Modeling of the Arctic Ocean can be traced back to the 1960s [Campbell, 1965]. In the early stages, researchers were mainly focused on the circulation patterns [Galt, 1973] and sea-ice movement [Maykut and Untersteiner, 1971]. The first three-dimensional numerical study of the Arctic Ocean circulation was done by Semtner Jr [1976] with 110km horizontal resolution and 14 vertical levels. With the development of community ocean general circulation models, more studies were published in the early 2000s, under the topic of Arctic Ocean freshwater, including the freshwater budget (e.g. Miller and Russell [2000], Steele et al. [1996]), the position and size of the Beaufort Gyre (e.g. Proshutinsky et al. [2002]) and the role of atmospheric patterns on freshwater export (e.g. Zhang et al. [2003]). The appearance of climate models, which couple simulation cores of ocean, sea-ice, atmosphere and land, provided a comprehensive numeric environment. Arctic freshwater studies were therefore able to resolve more details, for example, Holland et al. [2006] discussed the freshening of Arctic Ocean in the 21st century with different freshwater components. Mysak et al. [2005] simulated the Fram Strait sea-ice transport and found correlation with NAO index in an intermediate complexity earth system model.

The impact of Arctic Ocean freshwater export in the North Atlantic Ocean is also a field of active research. The numerical study of it started at 1990s. Häkkinen [1993], simulated the effect of sea-ice export in the Nordic Seas during the Great Salinity Anomaly by using a coupled ice-ocean model. In a 500-year control experiment, Jungclauss et al. [2005] found the modulation of the overturning circulation by Arctic freshwater export. Using an eddy-permitting regional model, Myers [2005] found the freshwater export from Davis Strait has little impact on the freshening of the Labrador Sea.

The numeric study of freshwater relevant tracers in the Arctic is still a newly defined topic. Freshwater tracer simulation has advantages in investigating the deposition of different freshwater components (instead of just the total budget) and their responses to atmospheric forcing. Manizza et al. [2009] simulated the riverine input of dissolved organic carbon and provided insights on parameterizing fluvial tracer export. Jahn et al. [2010] used passive tracers as proxies of river, Pacific Ocean and sea-ice melt freshwater and investigated the role of atmosphere in the export of different freshwater components.

In addition to the integrated studies of Arctic Ocean freshwater mentioned above, many simulation studies also examined the Arctic precipitation (e.g. Walsh et al. [1998]) or runoff (e.g. Wu et al. [2005]) alone, as single terms in the freshwater budget and thus contributed to the understanding of the entire system.

Chapter 3

Methodology

3.1 Model and regional Arctic configuration

The numerical model employed in the study is the tracer model MY_TRC. MY_TRC is under the numeric framework of Nucleus for European Modelling of the Ocean version 3.4 (NEMO 3.4). We parameterized the tracer model with dissolved Barium and Oxygen isotope ratio chemistry and used NEMO 3.4 [Madec and the NEMO team, 2012] physical schemes. The model was configured on an orthogonal grid which covers the entire Arctic Ocean with two open boundaries. The open boundary on the North Atlantic side is set along the 60°N parallel, close to the southern edge of Greenland, the other open boundary, which is on the North Pacific side, is set in the Bering Strait, at approximately 64°N.

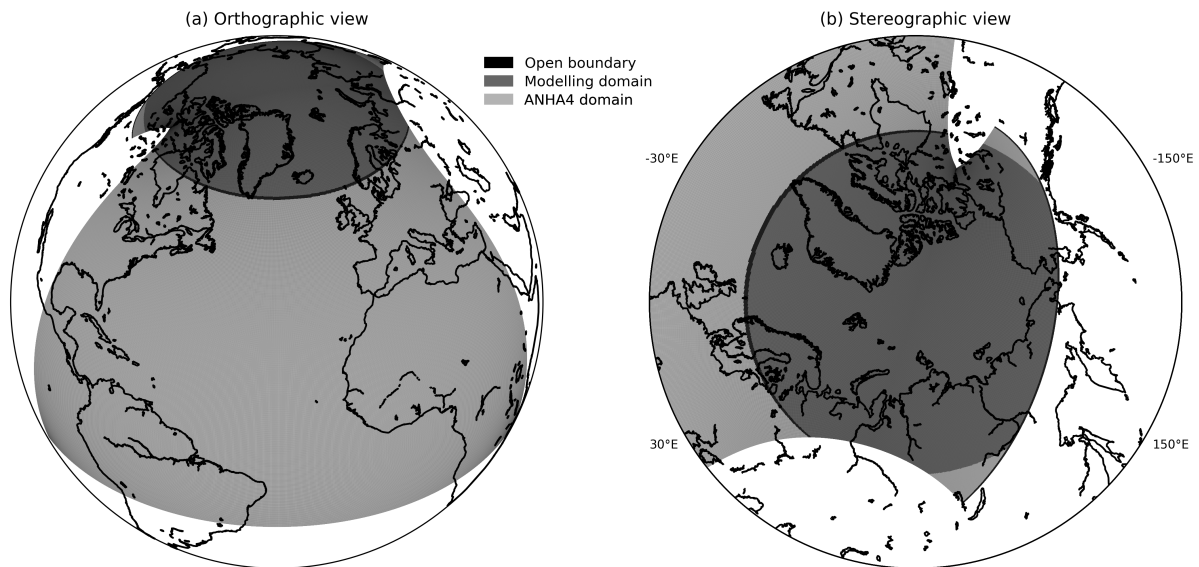


Figure 3.1: MY_TRC open boundaries (in black) and internal grid (in dark gray). Grid of ANHA4 experiments covers all the MY_TRC domain (both black and dark gray) and extends to the Atlantic Ocean (light gray).

Since both dissolved Barium and Oxygen isotope ratio are passive tracers, here MY_TRC was op-

erated offline (i.e. the tracer model is run using stored output files from the ocean and sea-ice model) with physical oceanographic and sea-ice output from the Arctic and North Hemisphere Atlantic 1/4 degree (ANHA4) experiments [Holdsworth and Myers, 2015]. ANHA4 experiments cover the entire domain of the tracer model and extend further southward in the Atlantic Ocean and have lateral boundaries along the 20°S parallel (figure 3.1).

In order to avoid the coordinate transfer between MY_TRC fields and ANHA4 forcing variables, the MY_TRC grid was chosen to coincide with the ANHA4 grid in the Arctic Ocean, The grid has about 11km resolution in the central Arctic and 50 vertical levels with a 1.05 m top layer, decreasing in resolution with increasing depth.

3.2 Tracer parameterizations

The tracer parameterization for dissolved Barium and Oxygen isotope ratio is prognostic. Different prescribed values were applied for tracers' sources and sinks near the surface, including river runoff, sea-ice variabilities and precipitation. The budget equation in the tracer model is [Foujols et al., 2000]:

$$\frac{\partial T}{\partial t} = \text{SMS} - \vec{v} \cdot \nabla T + \nabla_h \cdot (A_h \nabla_h T) + \frac{\partial}{\partial z} \left(A_v \frac{\partial T}{\partial z} \right) \quad (3.1)$$

Here T can be dissolved Barium (nM) or Oxygen isotope ratio (‰), $\vec{v} = (u, v)$ is the horizontal ocean velocity. ∇_h is the horizontal (x, y) gradient, A_h and A_v are the vertical eddy diffusivity parameters. SMS is the net impact of tracer sources and sinks:

$$\text{SMS} = \left(\frac{\partial T}{\partial t} \right)_R + \left(\frac{\partial T}{\partial t} \right)_{dil} + \left(\frac{\partial T}{\partial t} \right)_p + \left(\frac{\partial T}{\partial t} \right)_i \quad (3.2)$$

Where the right-hand side terms are the river input, the dilution effect, meteoric impact of Oxygen isotope ratio from precipitation and the fractionation during the sea-ice melting/formation, respectively. The river runoff term is explained in the next section and all the other terms are explained in section 3.2.2.

Dissolved Barium in this study is modeled as conservative which means the biological effects are not included. The small bias raised by this choice will be discussed in section 4.2. Also, the dissolved Barium contributed by hydrothermal venting is not included as the hydrothermal Barium is mainly in the particulate phase as barite and precipitates around the hot spring sources [Von Damm et al., 1985] and thus does not impact surface dissolved Barium. Oxygen isotope is modeled as conservative, as no major processes changes its value away from the ocean surface.

3.2.1 Riverine tracer input

In order to parameterize the riverine dissolved Barium and Oxygen isotope ratio export, the estuaries of all pan-Arctic rivers were grouped into multiple regions, and a seasonal cycle or a single value was assigned for each of the regions. In total, the tracer scheme has twenty regions for dissolved Barium (figure 3.2) input and seven regions for Oxygen isotope ratio (table 3.2) input.

During the simulation, the model checks the region of all grid points that have non-zero discharge values and calculates the tracer input by applying equation (3.3):

$$\left(\frac{\partial T}{\partial t}\right)_R = T_R \cdot R \cdot \frac{1}{d \cdot \rho_0} \quad (3.3)$$

Here the left of the equation is the fluvial tracer input, which has a unit of $c \cdot s^{-1}$, c is the unit of either dissolved Barium or Oxygen isotope ratio. R is the river discharge which contains non-zero values in coastal regions and over the top 15 m of the water column. In NEMO, runoff is added like rain over a grid cell with units of $kg \cdot m^{-2} \cdot s^{-1}$. d is the vertical scale of the grid. The density of freshwater is $\rho_0 = 1000.0 kg \cdot L^{-1}$. T_R is the prescribed tracer seasonal cycle or end-member value in given region in $c \cdot L^{-1} \cdot s^{-1}$.

Dissolved Barium

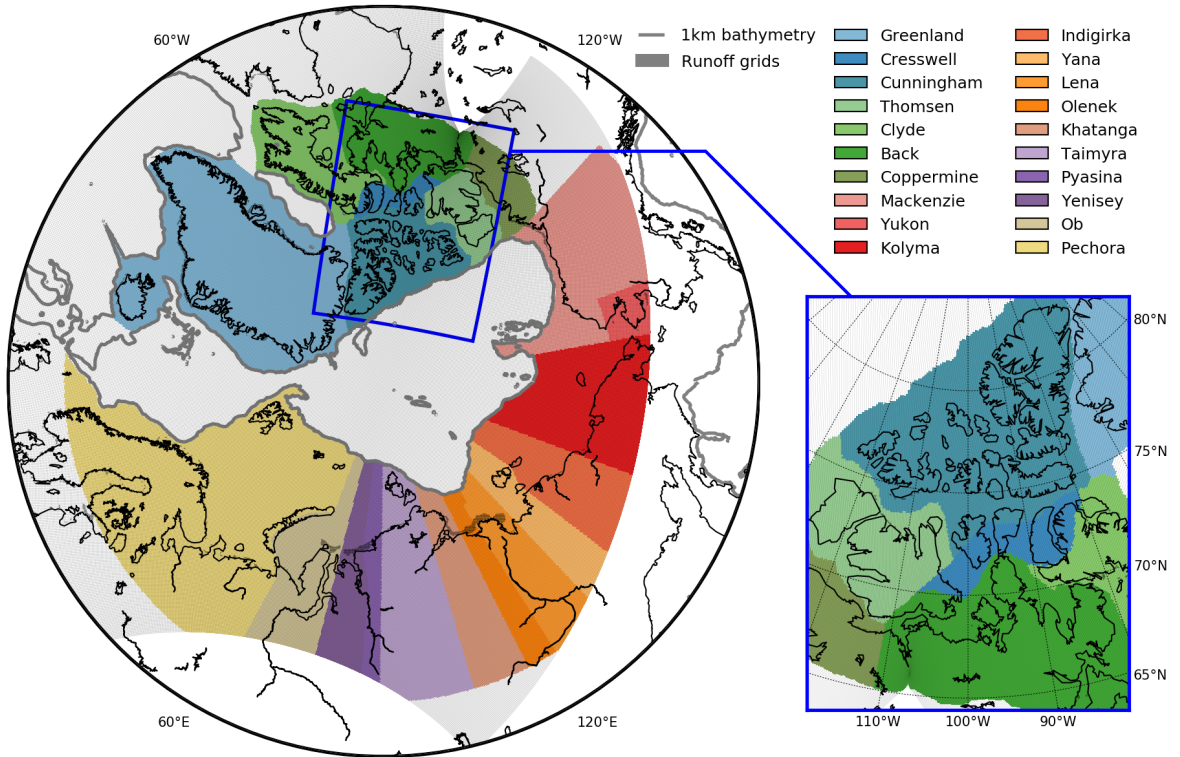


Figure 3.2: The classification of river estuaries in the Arctic Ocean. Rectangular frame on the bottom right is a zoom in CAA

For the riverine input of dissolved Barium, twenty different regions were used (figure 3.2). This division is based on the pan-Arctic watersheds defined in Lammers et al. [2001], the data availability of riverine dissolved Barium records and river discharge in different rivers. As described in section 2.2.1, the amount of Barium in the river depends on the type of river-born clays and sediment loads, so the fine classification in figure 3.2 reflects the diversity of geological environments of Arctic rivers.

The dissolved Barium input in “Greenland” was set as 0.0 nM by assuming that Greenland and Iceland river runoff is mainly glacial melt and has little Barium. For other regions, seasonal cycles were estimated. For each of the regions, except CAA, the biggest river of the region represents the dissolved Barium input of all other rivers. For regions inside the CAA, the river that has the dissolved Barium concentration closest to the average of all rivers in the region was chosen as the representative, since CAA rivers have no big differences in size. If a region has a representative river, then the name of the river is used to name the region (figure 3.2).

The Kolyma, Lena, Ob, Yenisey, Mackenzie and Yukon have the most frequent observations and are also the six largest Arctic rivers. Other rivers only have few measurements during the summer. So here, the seasonal cycle of these six largest rivers were first calculated, then the similarities among these seasonal cycles were identified and generalized to other, more poorly, observed rivers. This method is called the “Normalized ensemble seasonal cycle” calculation.

Fluvial dissolved Barium and Oxygen isotope ratio records were taken from ARCSS-107, Pan-Arctic River Transport of Nutrients, Organic Matter, and Suspended Sediments (PARTNERS), Arctic Great River Observatory (AGRO), Small Canadian Arctic River Flows (SCARFS) and River samples in the GEOTRACES Canadian Arctic Expedition (table 3.2). The data were used for the parameterization the riverine tracer input. The discharge of Yukon river was taken from the Piolet Station, United States Geological Survey (USGS) [USGS, 2016], the discharge of Mackenzie river was taken from Water Office, Environment Canada [EC-Wateroffice, 2016]. Other discharge records were taken from AGRO. The discharge data was used for calculating the flow weighted annual mean tracer input.

The discontinuous daily riverine dissolved Barium records were combined into monthly mean time-series. Then for the six largest Arctic rivers, linear interpolation was applied for the month that has no data, and the seasonal cycle is therefore calculated. After that, the seasonal cycle of the six largest rivers are normalized by dividing the flow weighted annual mean dissolved Barium concentration. Finally, the normalized seasonal cycle was ensemble averaged over the six rivers. For rivers with observations in only a few months, the normalized seasonal cycle was scaled by the available observations.

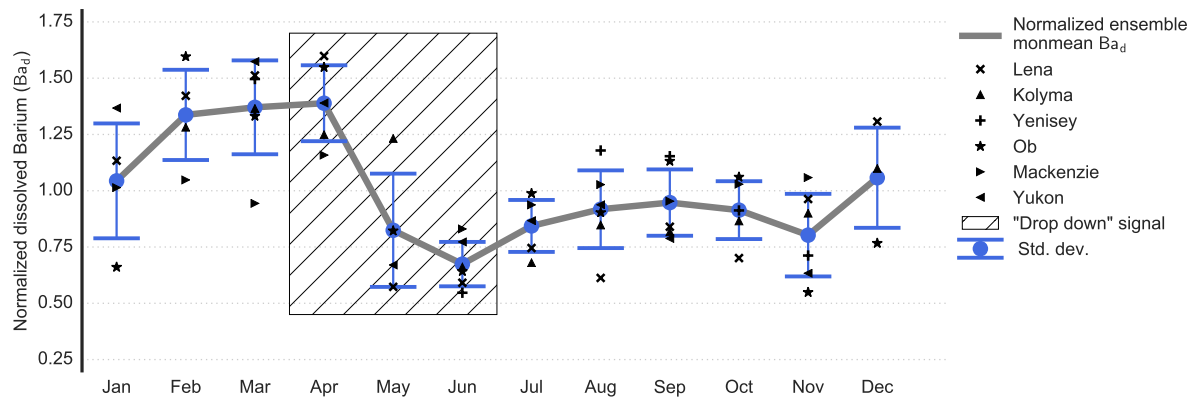


Figure 3.3: Normalized ensemble seasonal cycle of dissolved Barium for the six largest Arctic rivers. The grey solid line is the ensemble result. Black markers indicate all ensemble members. Blue bars show the standard deviation. The hatch shows the “drop down” signal.

Riverine dissolved Barium has strong seasonal variabilities, and this is the reason for using seasonal cycles instead of single end-member values (figure 3.3). The small standard deviations of the ensemble members indicate that the normalized seasonal cycles of these six rivers are similar. The biggest similarity is hatched and named as the “drop down” signal. The “drop down” signal is a significant decrease of normalized riverine Barium concentration from April to May. This “drop down” signal can be explained by the spring freshet which usually happens in mid-May. During this time, the river discharge increases strongly and dilutes the Barium concentration in the river. Previous studies of both Barium and alkalinity have seen a similar freshet dilution [Cooper et al., 2008], which supports that the “drop down” signal is not an artificial pattern. Since spring freshet is the dominant hydrological event in Arctic rivers, it is crucial to have the “drop down” signal in the dissolved Barium seasonal cycle of all Arctic rivers even though many of them do not have records in the late spring, early summer. This is also the motivation of “Normalized ensemble seasonal cycle” calculation.

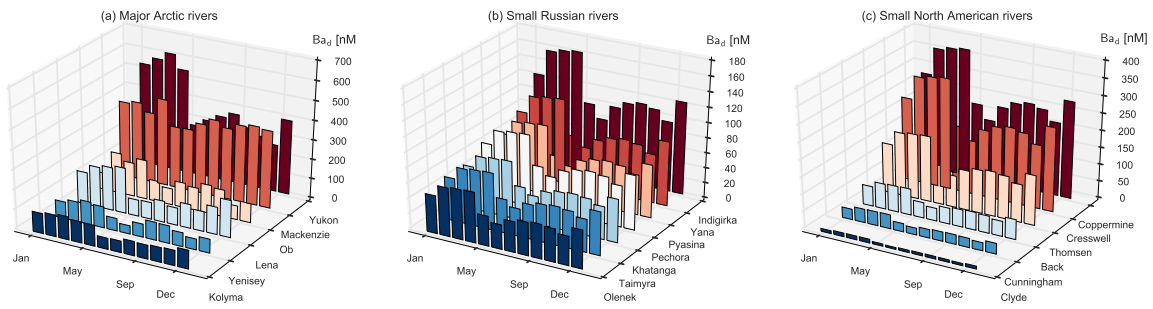


Figure 3.4: The seasonal cycle of dissolved Barium input in all parameterized Arctic rivers.

The variability due to the parameterized seasonal cycle is smaller than the difference in annual mean among rivers. North American rivers, like the Mackenzie River, always have dissolved Barium concentration higher than the Eurasian rivers (figure 3.4). In other words, dissolved Barium’s ability to separate the North American runoff from Eurasian runoff is not undermined by the parameterized strong seasonal cycle.

Note that, in this section, the term “the six largest Arctic rivers” is used, but the real difference in the parameterization are “well observed” rivers and “poorly observed” rivers. “Normalized ensemble seasonal cycle” calculation is a way that borrows information from the “well observed” group and uses it for the “poorly observed” group. The reason why we use “the six largest Arctic rivers” is because of the fact that big Arctic rivers are also the “well observed” rivers.

Oxygen isotope ratio

Compared with the large variation of dissolved Barium concentration in Arctic rivers, riverine Oxygen isotopes are more uniform because the diversity of river bed geological structure does not affect the variability of Oxygen isotopes. As previously mentioned in section 2.3.2, on the scope of the global hydrological cycle, all Arctic river runoff is generated from high latitude precipitation and called “meteoric water”.

In the tracer scheme, the riverine Oxygen isotope ratio input has seven different classifications: “Kolyma”, “Lena”, “Ob”, “Yenisey”, “Mackenzie”, “Yukon” and “others” (table 3.1). The riverine input ratios in these seven regions were set to the flow weighted annual mean records. For other rivers, an unified end-member value -20.0‰ was used, consistent with other research [Yamamoto-Kawai et al., 2008].

Table 3.1: The riverine Oxygen isotope ratio input of the tracer scheme

Kolyma	Lena	Yenisey	Ob	Yukon	Mackenzie	Others
-22.7‰	-21.6‰	-18.3‰	-15.9‰	-20.7‰	-29.8‰	-20.0‰

3.2.2 Sea-ice and precipitation

The dilution effect

Sea-ice formation/melting, net precipitation (precipitation minus evaporation) and river runoff can be viewed as extra input and output of ocean water and therefore affect the distribution of solute including modeled tracers. During the simulation, all the freshwater types dilute the tracer by the ratio of the flux to the cell depth:

$$\left(\frac{\partial T}{\partial t}\right)_{dil} = (E - P - R) \cdot \frac{T_t}{\rho_r \cdot d} \quad (3.4)$$

In the tracer scheme, $\rho_r = 1025.0 \text{ kg/m}^3$ is the reference density of sea water in NEMO 3.4, R is the amount of river runoff which enters into the Arctic. $E - P$ is the net water loss by net sea-ice formation and net evaporation, both terms have units of $\text{kg} \cdot \text{m}^{-2} \cdot \text{s}^{-1}$. R is the input from ANHA4 runoff forcing and $E - P$ can be calculated by using

$$E - P = -F_S \frac{S_r}{S} \quad (3.5)$$

which is the reverse of salt flux calculation in Schmitt et al. [1989]. Here F_S is the salt flux, which can be defined as the product of salinity and water flux in the ocean, $S_r = 34.7$ is the reference salinity of sea water on the practical salinity scale, and S is the sea-surface salinity. Both F_S and S can be taken from ANHA4 experiments. Noted that $E - P$ has values in the entire domain.

Isotopic fractionation

The amount of Oxygen-18 in sea-ice and precipitation is different due to the fractionation process. The parameterization of the precipitation input of Oxygen isotope ratio is

$$\left(\frac{\partial T}{\partial t}\right)_p = W_T \cdot W \cdot \frac{1 - I_c}{d \cdot \rho_0} \quad (3.6)$$

Here $(\partial T / \partial t)_p$ is the contribution of 5-day average precipitation, $W_T = -20.0\text{‰}$ is the Oxygen isotope

ratio end-member value for meteoric water, consistent with other research [Yamamoto-Kawai et al., 2005, 2008] and the riverine end-member settings. W is the net precipitation and I_c is the sea-ice cover in ANHA4 output, so that the precipitation over sea-ice does not impact the Oxygen isotope ratio in the ocean. For O^{18}/O^{16} , equilibrium fractionation dominates in the Arctic, so kinetic fractionation is not parameterized.

The $E - P$ in equation (3.5) can be used to calculate the isotopic fractionation of Oxygen isotopes during sea-ice melt or formation periods:

$$\left(\frac{\partial T}{\partial t}\right)_i = \frac{1}{d \cdot \rho_0} \cdot [I_T \cdot -(E - P) - W] \quad (3.7)$$

$I_T = 1.5\%$ is the Oxygen isotope ratio end-member value of sea-ice melt water, this uniform choice is reasonable for the isotopic fractionation in the central Arctic, Barents Sea and Fram Strait but is likely an overestimation for the Canada Basin. A detailed discussion is given in section 4.2.2 and section 5.2.2. Note that $-(E - P)$ is the total flux of net sea-ice melt and net precipitation, therefore, $-(E - P) - W$ is the flux from sea-ice melt water in $\text{kg} \cdot \text{m}^{-2} \cdot \text{s}^{-1}$.

3.3 Configuration of numerical experiments

The tracer model was operated offline from 2002 to 2013 by using the tracer model configuration described in section 3.1 and tracer parameterizations described in section 3.2. The initial field of dissolved Barium was created from field measurements through ordinary Kriging interpolation. ARCSS-102, ARK XIV/2A, CBL32PZ, HLY0301, ARK XXII/2, Beaufort Gyre Exploration Project (BGEP) 2003-2005 and North Pole Exploration Observatory (NPEO) 2000-2004 data (table 3.2) were used to estimate the initial field and the open boundary condition of the dissolved Barium in the tracer model. For the Oxygen isotope ratio, the reanalysis data from LeGrande and Schmidt [2006] was chosen and re-mapped to the model grid as the initial field.

For the built-in physical schemes in NEMO 3.4, Total Variation Diminishing (TVD) was chosen for the horizontal advection, Laplacian lateral diffusion was used with a horizontal eddy diffusivity of $300.0 \text{ m}^2 \cdot \text{s}^{-1}$, consistent with the salinity horizontal eddy diffusivity in ANHA4-EXH005 experiment. The model receives runoff with a mixing coefficient of $0.001 \text{ m}^2 \cdot \text{s}^{-1}$ over the top 15 m of the water column. The edge points of the MY_TRC model domain preserved tracer values of the initial field as the open boundary condition.

The oceanic forcing of this simulation is the five-day average output of ANHA4-EXH005. ANHA4-EXH005 is a member of ANAH4 experiment, it runs under the coupled NEMO 3.4 and Louvain-la-Neuve Sea Ice Model version 2 (LIM2) [Vancoppenolle et al., 2012]. The subgrid scale vertical mixing was parameterized through a turbulent kinetic energy based second-order turbulent closure scheme [Mellor and Yamada, 1982]. The open boundary condition of ANHA4-EXH005 was driven from Global Ocean Reanalyses and Simulations (GLORYS) with buffer zones in the Bering Strait, along the 20°S parallel in the Southern Atlantic and in the Mediterranean Sea. ANHA4-EXH005 was initialized with GLORYS sea surface height, temperature, salinity and velocities. The Coordinated OceanIce Reference

Experiments (CORE) bulk formulas [Large and Yeager, 2004] were applied to compute fluxes of heat, water, and momentum [Xianmin, 2016].

The atmospheric forcing of the ANHA4-EXH005 is Canadian Meteorological Centre Global Deterministic Prediction System Reforecasts (CGRF) data. This dataset has a temporal resolution of 6-hour and covers the period of 2002-2013. The CGRF is thought to have comparable quality with reanalysis data in terms of surface temperature, humidity and winds [Smith et al., 2014]. The high spatial and temporal resolution of the CGRF data permits detailed atmospheric structure at high latitudes when used as the forcing of ANHA4 experiments [Holdsworth and Myers, 2015]. The river discharge forcing of both the ANHA4-EXH005 and this simulation is a re-mapped monthly river discharge from Dai et al. [2009] and the Greenland glacier melt from Bamber et al. [2012]. The former is reanalysis data from gauge records and Community Land Model version 3 (CLM3), the latter is based on field observations.

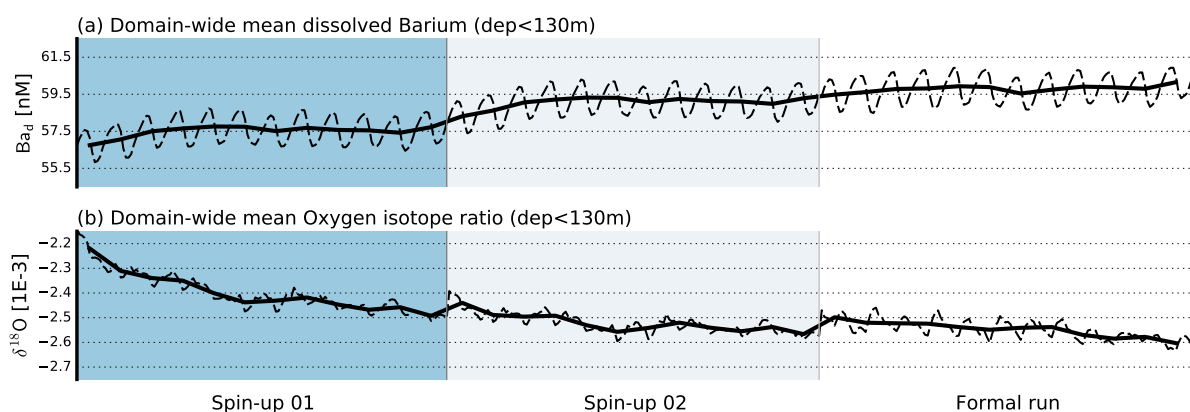


Figure 3.5: Domain-wide mean dissolved Barium (a) and Oxygen isotope ratio (b) in two spin-up experiments and the formal run. Each of the spin-up experiment was run under ANHA4-EXH005 forcing from 2002 to 2013.

Before the 2002-2013 simulation, the tracer model was spun-up for 24 years. The first 12-year used the ANHA4-EXH005 forcing from 2002-2013. The second 12-year used the same forcing again. A 24-year spin-up is longer than many other regional modeling studies. Such a long spin-up was needed to provide stable seasonal cycles and balance the riverine tracer input with the tracer flux going out of the Arctic Ocean (figure 3.5). The model simulation results above 130 m after spin-up were thought to be independent from the dissolved Barium measurements which were used as the initial field and then also used in the model evaluation. In the intermediate and deep layers, the tracer values were still trending due to the lack of vertical tracer dynamics. Both dissolved Barium and Oxygen isotope ratio fields were saved as monthly averages.

3.4 Methods and data for analyzing the results

The domain-wide average was calculated in the entire MY_TRC domain (section 3.1) to examine the time evolution of the tracer simulation result. The vertical mean from surface to 130 m is calculated for examining the tracer anomalies and dissolved Barium climatology which is consistent with the

depth range of FWC calculation and represents the distribution of tracers above the halocline layer (section 2.1.2). The climatology of Oxygen isotope ratio was calculated on the first model layer (i.e. 1.05 m) since it is directly modified by meteoric and sea-ice melt water and shows the highest variability.

3.4.1 Data applied in model parameterization and evaluations

Table 3.2: Meta data of the field observations

Project/Data	Cruise	Platform	Time	Source
ARCSS-107	Various	Various	1993-1996	1
PARTNERS	-	-	2004-2007	2
AGRO I/II	-	-	2009-2015	2
SCARFS	-	-	2014	3
GEOTRACES - Canadian Arctic Expedition	-	-	2014-2015	4
	HX171	R/V Alpha Helix	1993	
	ARCRAD-93	USCGC Polar Star	1993	
ARCSS-102	ARK IX/4	R/V Polarstern	1993	5
	Larsen-93	CCGS Henry Larsen	1993	
	HX174	R/V Alpha Helix	1993	
ARCSS-105	ARK XIV/2A	R/V Polarstern	1998	6
CBL32PZ	CBL32PZ	USCGC Polar Star	2002	7
HLY0301	HLY0301	R/V Healy	2003	8
GEOTRACES	ARK XXII/2	R/V Polarstern	2007	9
NPEO	Various	Various	2000-2013	10
BGEP	Various	Various	2003-2005	11

1. Falkner [2009c], <https://data.eol.ucar.edu/dataset/106.ARCSS107>
2. AGRO [2016], <http://www.arcticgreatrivers.org/data.html>
3. Alkire [2015], <https://arcticdata.io/catalog/#view/doi:10.18739/A2CP8H>
4. Kristina A. Brown (kbrown@whoi.edu)
5. Falkner [2009a], <https://data.eol.ucar.edu/dataset/106.ARCSS102>
6. Falkner [2009b], <https://data.eol.ucar.edu/dataset/106.ARCSS105>
7. Woodgate [2015], <https://cchdo.ucsd.edu/cruise/32PZ20020819>
8. Falkner [2014], <https://cchdo.ucsd.edu/cruise/32H120030721>
9. Roeske et al. [2012], http://www.bodc.ac.uk/geotraces/data/inventories/arkxxii_2/
10. NPEO [2015], <http://psc.apl.washington.edu/northpole/Data.html>
11. Proshutinsky and Krishfield [2016], <http://www.whoi.edu/website/beaufortgyre/expeditions>

Both field observations (table 3.2) and forcing variables were used in analyzing the model output. CGRF sea level pressure and horizontal 10 m-wind were used in the composite anomaly calculations. Sea level pressure was also used to calculate AO and NAO indices. ANHA4 salinity was used to calculate the FWC; sea surface height and horizontal velocities were used to investigate surface ocean circulation. ANHA4 wind stress was applied for diagnosing the intensity of Ekman divergence and convergence. $E - P$ which was calculated in the tracer scheme was also used for analyzing the variability of FWC and Oxygen isotope ratio.

3.4.2 Methods in the model evaluation

Normalized Root Mean Square Deviation (NRMSD) and mean bias were used in the model evaluation and their definitions are:

$$\text{NRMSD} = \frac{\text{RSMD}}{\max(x) - \min(x)}, \text{RSMD} = \sqrt{E[(\hat{x} - x)^2]} \quad (3.8)$$

$$\text{Mean bias} = E(x) - E(\hat{x})$$

Here, x is the field measurement, \hat{x} is the model output, \bar{x} is the average of x and E means expectation. Observations and model output are considered as two groups in the comparison. Each sample of the project/cruise is compared with the model output on its closest model grid. The date of samples are matched with the corresponding month in the model output. When the NRMSD and mean bias are calculated over different depths, observations were vertically interpolated to the model depth. If at a certain depth, the total number of samples is smaller than 10, then the NRMSD will not be calculated since the maximum minus minimum may not have an enough range for the normalization.

CBL32PZ, HLY0301, ARK XXII/2 (contains dissolved Barium only), BGEP 2003-2005, NPEO 2004-2008, 2010 (contains Oxygen isotope ratio only) and 2013 data were used in the model evaluation (table 3.2). BGEP and NPEO have observations in the Canada Basin and the central Arctic in multiple years (BGEP has data from 2003 to 2005; NPEO has data from 2004 to 2008 and 2010, 2013; 2010 data contains only Oxygen isotope ratio records). The data in all available years will be used for the NRMSD and mean bias calculation. Observations and all the model result in a certain area (the central Arctic for NPEO and the Beaufort Sea for BGEP) above 130 m will be averaged and compared as timeseries.

3.4.3 Physical calculations

Because the NEMO grid is not a simple rectilinear grid, the ANHA4-EXH005 wind stress curl was calculated by re-mapping the wind stress onto a Mercator grid and applying the finite difference calculation:

$$\text{curlz}(\vec{\tau}) = \frac{\Delta\tau_{\varphi}}{\Delta x} - \frac{\Delta\tau_{\lambda}}{\Delta y} + \frac{\tau_{\lambda}}{R} \tan \varphi \quad (3.9)$$

where τ is the wind stress, R is the radius of the earth, φ is latitude, λ is longitude, Δx and Δy are the sizes of grid.

$$\Delta x = R \cos \varphi \Delta \lambda \quad \Delta y = R \Delta \varphi \quad (3.10)$$

for all the Δ terms, first order forward and backward difference were applied for edge points and second order central difference was used for all the interior points. The derivation is in appendix C.

The dissolved Barium fluxes, through the Bering Strait, Fram Strait, the Barents Sea and Baffin Bay are calculated to estimate the total budget of dissolved Barium in the Arctic. The tracer flux is given by:

$$F(Ba_d) = \sum_{\substack{i=i_0 \\ j=j_0}}^{i_1, j_1} T_{i,j} A_{i,j} (\vec{v}_{i,j} \cdot \vec{n}) \quad (3.11)$$

where F is the tracer flux with the unit of $\text{mol} \cdot \text{s}^{-1}$. T is the tracer concentration. (i_0, j_0) and (i_1, j_1) are the starting and ending indices of latitudes and longitudes of the transects in ANHA4 grid. A is the area of the transect grid cells and calculated as “depth grid size” \times “horizontal grid size”.

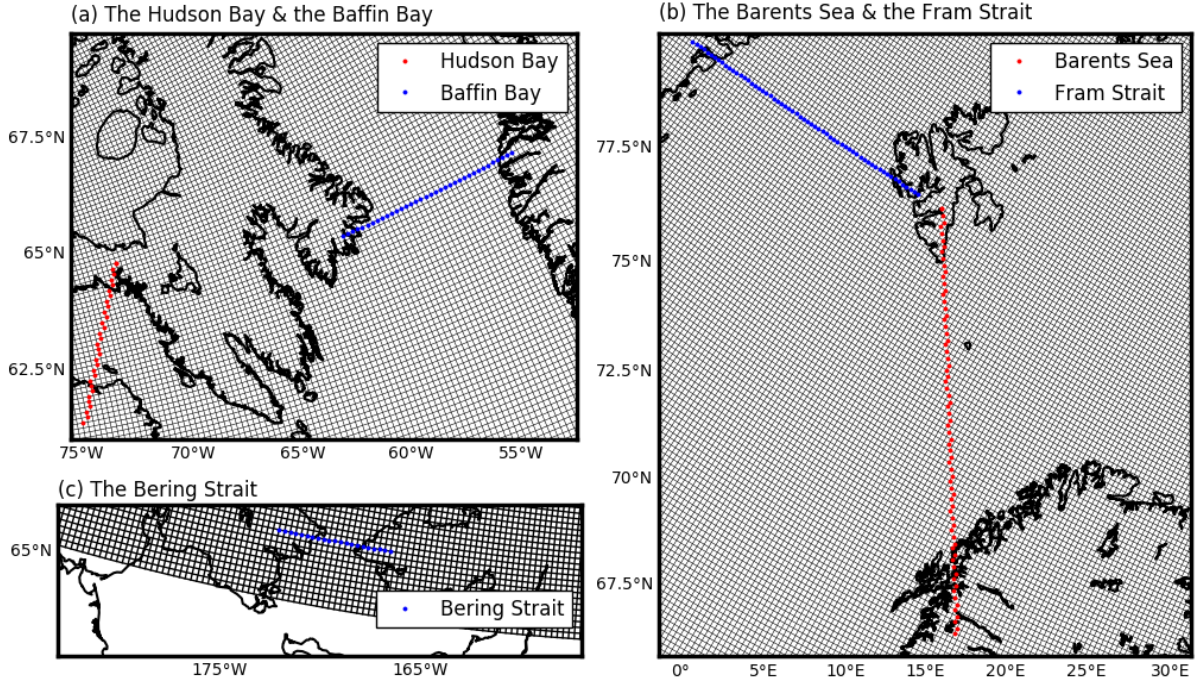


Figure 3.6: The ANHA4 grid based transects in the the Baffin Bay and Hudson Bay (a), Fram Strait and Barents Sea openings (b), and the Bering Strait (c).

The Fram Strait transect was set from the East Greenland coast to the Svalbard; the Barents Sea transect was set from the Svalbard to the Norwegian coast. The Bering Strait transect was built close to the 64°N parallel. The Baffin Bay transect has two parts, one cross the Davis Strait and the other one covers the entrance from the Hudson Bay to the North Atlantic (figure 3.6).

The total input of dissolved Barium is also estimated. The calculation is based on the ANHA4-EXH005 river discharge forcing (section 3.3) and the riverine dissolved Barium parameterization (section 3.2):

$$F_r(Ba_d) = \frac{1}{\rho_0} R \cdot A_h T_r \times 10^{-6} \quad (3.12)$$

Here F_r is the dissolved Barium input from rivers, the unit is $\text{mol} \cdot \text{s}^{-1}$. A_h is the horizontal area of the surface grid cell. Note that, F_r is two dimensional, and it will be summed by the estuary of a certain river or the regional classification (figure 3.2).

3.4.4 Statistical methods

The anomaly of variables was calculated relative to the 2002-2013 monthly mean results. The composite anomaly was calculated as the difference of the average of a timeseries in its high and low phases. Higher than the standard deviation (σ) or lower than the negative standard deviation ($-\sigma$) are defined as high and low phases. The significance test for the composite anomaly is the two-sample t-test. Linear regression with a two-sided t-test was applied for estimating the trend. The Empirical Orthogonal Function (EOF) decomposition [Lorenz, 1956] was applied to the monthly detrended FWC anomalies to investigate the dominate modes of variations. The first three modes were analyzed with composite anomaly of CGRF and ANHA4 variables. The sampling error of the EOF is estimated by the “rule of thumb” [North et al., 1982] with the effective degree of freedom calculated as Bretherton et al. [1999] suggested. The EOF does not contain the information of climatology, seasonal cycle and linear trends. Each EOF mode is shown as a spatial patterns (with the FWC scale) and a normalized Principal Component (PC) (without the FWC scale, and here after simplified as “PC”). Spectral analysis by the Fast Fourier Transform (FFT) based “periodogram” technique was used for analyzing the PC of each mode. In this research, the high spectral powers of the PCs are found in the low frequency bands, and the red noise test requires higher spectral power to pass. Hence, only the red noise confidential intervals will be shown. Pearson correlation was applied for investigating the atmospheric driving factors and the response of modeled tracers. Full details are in appendix B.

3.4.5 Indices applied in the research

The TDS intensity index is calculated as the mean horizontal speed above 130 m in an area from the central Arctic to the Fram Strait. The Beaufort Gyre intensity index is estimated as the sea surface height maximum in the Beaufort Gyre (figure 3.7).

By applying an EOF decomposition to the CGRF sea level pressure in 20°N-90°N, the first three modes can be identified as AO, dipole anomaly and NAO (see appendix D). Among which the dipole anomaly is a newly detected atmospheric teleconnection pattern [Wu et al., 2006]. The positive phase of the dipole anomaly has positive sea level pressure anomaly in the Canada Basin and CAA and negative sea level pressure anomaly on the Eurasian side of the Arctic with strong meridional wind in the TDS region [Watanabe et al., 2006, Wu et al., 2006]. In this research, the impact of dipole anomaly on the surface ocean is quantified by the TDS intensity index. For the rest of modes, the PC of the first mode was applied as the AO index and the PC of the third mode was used as the NAO index. The AO and NAO indices from National Oceanic and Atmospheric Administration (NOAA)-Climate Prediction Center (CPC) [CPC-NOAA, 2016] were also used as they have longer time span. The CGRF and NOAA-CPC indices are both normalized and significantly correlated (AO indices: $R = 0.86$, $p < 0.01$; NAO indices: $R = 0.37$, $p < 0.01$). More details can be found in appendix D.

3.4.6 Linear mixing model

The term “Linear mixing model” means the reverse calculation of the mixing of different end-members. It works well for estimating different freshwater components in the Arctic. The linear mixing model

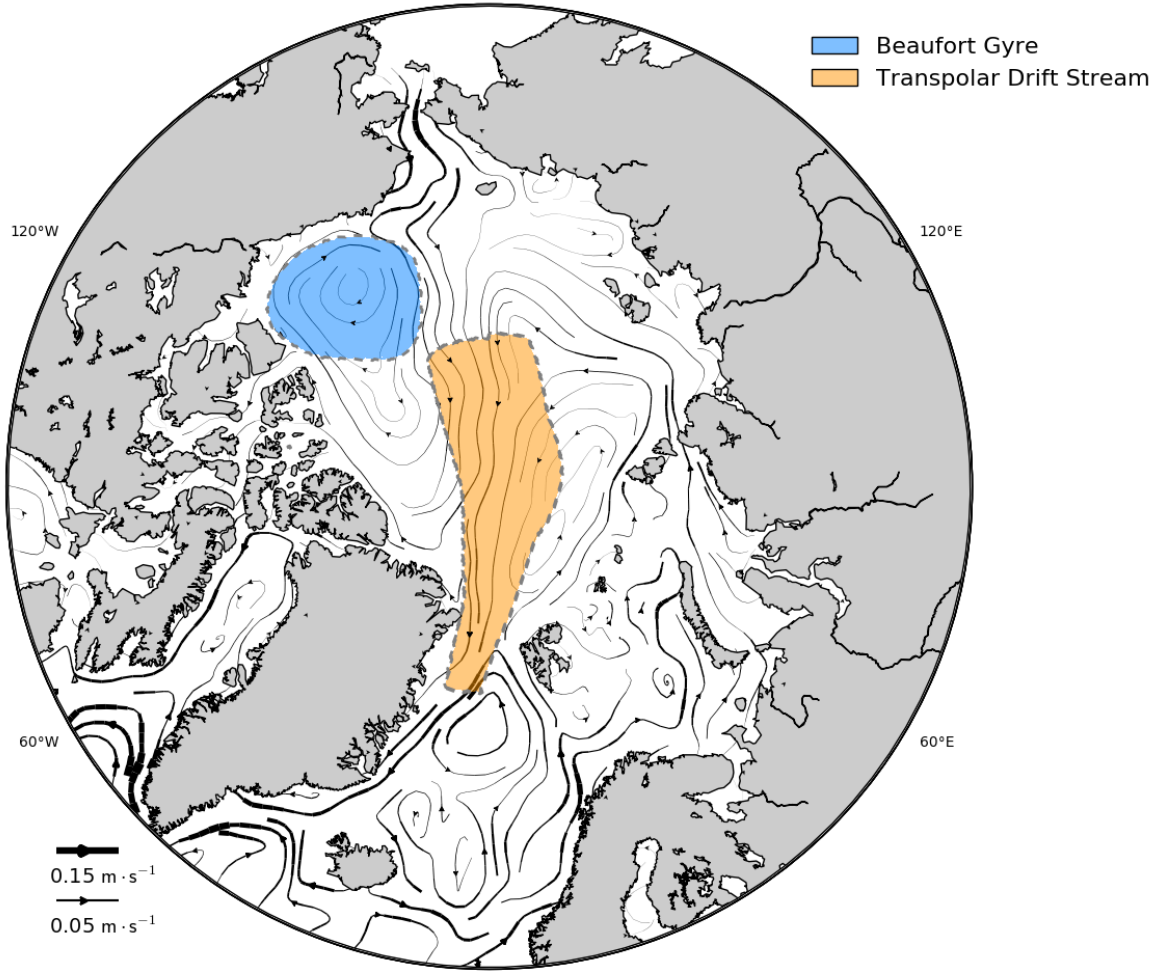


Figure 3.7: The 2002-2013 mean ANHA4-EXH005 velocities above 130 m and regions that define the TDS intensity (orange) and the Beaufort Gyre intensity (cyan) indices.

is used to calculate the fraction of North American and Eurasian runoff in the Beaufort Gyre. In this research, we focused on real ocean tracers, not passive tracers to identify single rivers. Similar to observations, the origin of the freshwater can be estimated through a linear mixing model. Tracers available for the linear mixing model include salinity, dissolved Barium and Oxygen isotope ratio.

$$f_{NA} \begin{bmatrix} S_{NA} \\ Ba_{NA} \\ \delta^{18}O_{NA} \\ 1.0 \end{bmatrix} + f_{EU} \begin{bmatrix} S_{EU} \\ Ba_{EU} \\ \delta^{18}O_{EU} \\ 1.0 \end{bmatrix} + f_i \begin{bmatrix} S_i \\ Ba_i \\ \delta^{18}O_i \\ 1.0 \end{bmatrix} + f_o \begin{bmatrix} S_o \\ Ba_o \\ \delta^{18}O_o \\ 1.0 \end{bmatrix} = \begin{bmatrix} S \\ Ba_d \\ \delta^{18}O \\ 1.0 \end{bmatrix} \quad (3.13)$$

Here the subscript “NA”, “EU”, “i” and “o” means North American runoff, Eurasian runoff, Sea-ice melt water and Ocean water. f is the fraction of each component, the sum of all the fractions should be 1.0, and except f_i , other fractions cannot be negative. The top-three elements in all matrixes in equation (3.13) are the chosen end-member values.

Table 3.3: Tracer end-member settings in Beaufort Sea

Tracer	North American runoff	Eurasian runoff	Sea-ice melt	Ocean
Salinity	0.0	0.0	0-0.4	32.0-34.8
Ba _d [nM]	371.08*	101.67*	0.0*	59.2
$\delta^{18}\text{O}$ [‰]	-19.76*	-19.61*	1.5*	0.0

Symbol “*” means the end-member value is prescribed in the tracer scheme.

The linear mixing model is used in the Beaufort Gyre to analyze the fraction of Eurasian and North American runoff. Given the location, the dissolved Barium and Oxygen isotope ratio end-members of North American runoff are the flow weighted annual mean estimates for the Mackenzie river. The tracer end-members of Eurasian runoff are the mean input of Kolyma and Lena as these two rivers are the big Eurasian rivers that are close to the Beaufort Sea and thus their runoff dominates any Eurasian runoff that is transported into the Beaufort Gyre (e.g. in the simulation study of [Jahn et al., 2010], it takes about six years for East Siberian Sea runoff to reach the western side of CAA). These values were calculated during the parameterization stage and prescribed in the tracer scheme (section 3.2). The sea-ice melt Oxygen isotope ratio end-member value 1.5‰ is consistent with that used in the tracer model. The dissolved Barium end-member value in the ocean is the grid weighted average of the initial field above 130 m. This is close to the observation based end-member set in Taylor et al. [2003] which is 57.0 nM. We assume the ocean end-member value of Oxygen isotope ratio is 0.0‰ as defined by Vienna Standard Mean Ocean Water (VSMOW) (table 3.3).

Note that, sea-ice melt and ocean salinity end-members have ranges, the former is because of the diverse choice by different research, and the latter is because the three tracers in this research cannot separate the Pacific Ocean water from Atlantic Ocean water, so the “ocean” component is considered to have variations and can represent both the Atlantic and Pacific water mass.

Chapter 4

Results

4.1 Climatology and seasonal cycles

The Arctic ocean dissolved Barium and Oxygen isotope ratio were simulated for the period of 2002-2013 using forcing from the atmosphere, ocean and Arctic rivers. This section will consider the temporally averaged results of the two tracers and their seasonal cycle. Together, the climatology and seasonal cycles can explain most of the tracer distribution and provide spatial and temporal insights into the two tracers.

4.1.1 Dissolved Barium

The climatological state of dissolved Barium concentration above 130 m (figure 4.1, a) varies from 40 nM to 90 nM; in river estuaries, the value can be higher than 100 nM. The North American side of the Arctic, including the Canada Basin, part of the Chukchi Sea and the Alpha - Mendeleev Ridge, has high dissolved Barium concentration which reflects the contribution of high Barium concentration rivers like the Mackenzie River. The dissolved Barium concentration is relatively low in the Barents Sea, the Kara Sea and the Nansen Basin, because The West Spitsbergen Current and Norwegian Currents bring low dissolved Barium water into the Arctic. Similarly, West Greenland Current transports the low dissolved Barium concentration water across the Davis Strait and the dissolved Barium value in Baffin Bay is therefore low. Dissolved Barium concentration is higher in the Beaufort Sea than in the Lincoln Sea and the northern part of the CAA due to the larger input of Barium from the Mackenzie River than from the lower Barium concentration and lower flux from the CAA rivers. The dissolved Barium concentration is high in the coastal parts of the East Siberian and Laptev Seas; this is a combined effect of shallow water and river input. Indeed, the volume of the shallow (< 30 m) coastal regions is small and easily flushed by the discharge from the Lena and other high Barium concentration Eurasian rivers. The shallow topography also makes the East Siberian Sea and Laptev Sea water easily modified and therefore these regions have high variabilities

The timeseries of dissolved Barium (figure 4.1, c) has been averaged horizontally over the whole model domain and vertically from the surface to 130 m depth. The dissolved Barium value fluctuates

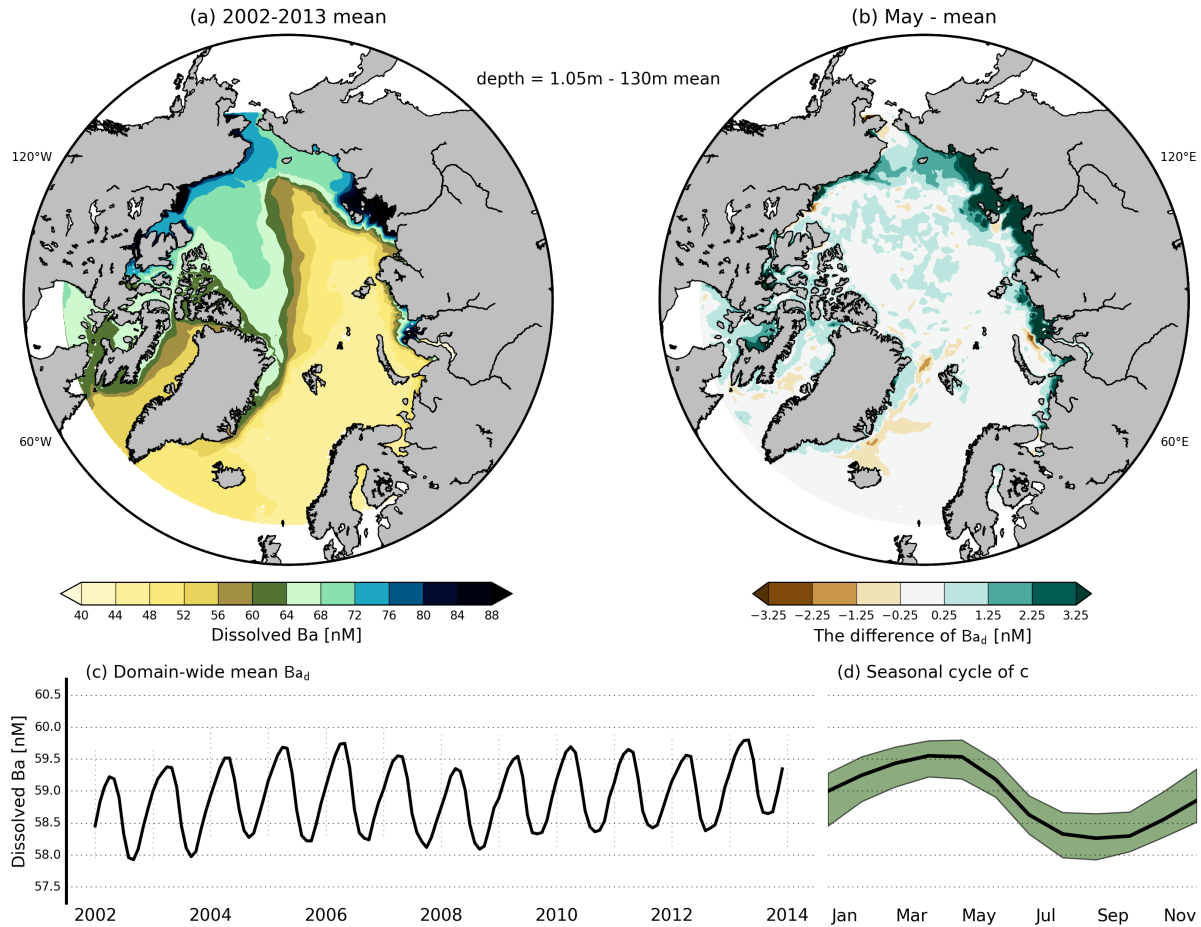


Figure 4.1: Simulated 2002-2013 climatology state of dissolved Barium above 130 m. (a) is the annual mean state. (b) is the difference between the mean state in May and (a). (c) is the domain-wide mean dissolved Barium monthly mean timeseries. (d) is the seasonal cycle of (c).

by 1 nM about the climatological state of 59 nM. The peak of the seasonal cycle of the domain-wide mean dissolved Barium appears in May, and the trough happens in September (d). This peak-to-trough pattern is the effect of both the riverine tracer input and the sea-ice freeze-thaw cycle. In the late spring and early summer, the spring freshet significantly increases the river discharge and brings more Barium into the domain. Then during the July-September period, the dilution effect due to the sea-ice melt plus the decrease of both riverine Barium input (section 3.1) and river discharge make the domain-wide dissolved Barium reach its minimum. After that, from November to April of the next year, riverine Barium input is relatively low and stable, but the increase of sea-ice formation, increases the salinity and also the dissolved Barium concentration.

The positive difference between May and the annual mean dissolved Barium in Arctic river estuaries clearly shows the contribution of riverine dissolved Barium during the spring freshet period (figure 4.1, b) and is consistent with the seasonal cycle result in (figure 4.1, d). The small negative difference offshore during May is due to the sea-ice freeze-thaw cycle. In May, the Arctic is in the early part of the

thaw.

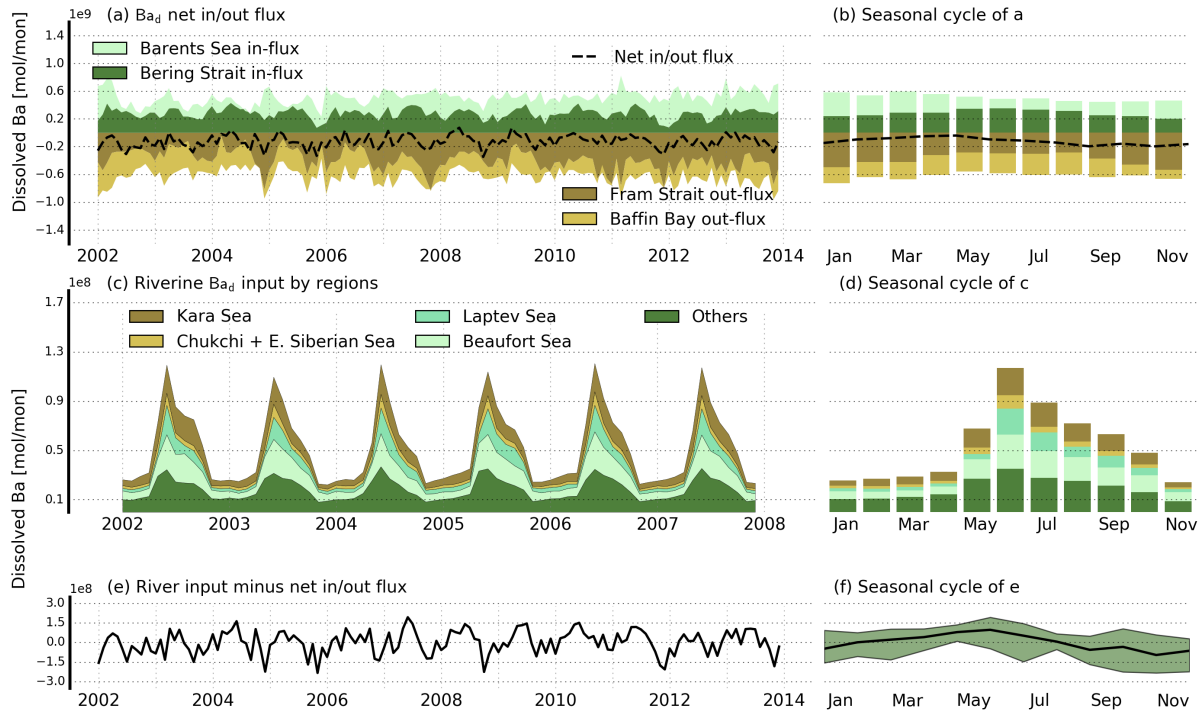


Figure 4.2: Simulated dissolved Barium fluxes through different pathways (a) and their seasonal cycles (b). Negative in (a) means out flux and the black line is the net result. (c) and (d) are simulated riverine dissolved Barium input and its seasonal cycle. (d) shows the time range of 2002-2008, and the 2007-2008 pattern was repeated in the 2009-2013 period. (e) is the riverine dissolved Barium input minus the net in/out flux. (f) is the seasonal cycle of (e). The calculation of (a-d) is based on equation (3.11) and equation (3.12). Rivers input on the southern part of transects (figure 3.5) is small and not considered.

The timeseries of dissolved Barium fluxes through the transects in Bering Strait, Fram Strait, Baffin Bay and Barents Sea (figure 4.2, a) was calculated and summed from surface to bottom. Fram Strait and Baffin Bay dissolved Barium fluxes are negative which reflect the dissolved Barium out flux driven by the TDS and the Labrador Sea Current, respectively. Meanwhile Bering Strait and Barents Sea dissolved Barium fluxes are positive due to net inflows. The net flux is negative, and reveals that, more dissolved Barium goes out of the Arctic Ocean than comes in. The total in-out and net dissolved Barium fluxes do not have a strong seasonality (figure 4.2, b).

The riverine dissolved Barium input (figure 4.2, c) and seasonal cycle (d) were calculated and summed over regions (figure 3.2). From November to April, the dissolved Barium delivered from the rivers is low and stable, then it quickly reaches a peak in June after the spring freshet and gradually decreases from July to October. The high dissolved Barium input in the Beaufort Sea shows the impact of the high dissolved Barium end-member value in the Mackenzie River. The high input in the Laptev Sea reflects the role of high discharge Eurasian rivers like the Lena. Also note that, the peak of riverine Barium input is in June, but the peak of domain-wide averaged dissolved Barium is May. This shift is

because the sea-ice melt water dilutes the surface dissolved Barium in June and makes the model value lower.

Considering the Barium budget of the Arctic as a whole, the total amount of riverine dissolved Barium input is roughly balanced by the net dissolved Barium out flux during the simulation (figure 4.2, e-f). The balance explains the stable dissolved Barium results (figure 4.1) and shows that the model has reached equilibrium state after its 24-year spin-up. The contrast between the strong seasonality in the river input and the weak seasonality in the net Barium fluxes results in the seasonal cycle of dissolved Barium in the Arctic ocean. The weak seasonality that is seen in the net Barium export is primarily due to changes in water flux through the Straits, not in Barium concentration changes.

Table 4.1: Total annual riverine dissolved Barium input in this research and the estimate from Guay and Falkner [1998]

Mackenzie	Ob	Yenisey	Lena	Pechora
This research				
$1.5 \times 10^8 \text{ mol}$	$4.3 \times 10^7 \text{ mol}$	$7.6 \times 10^7 \text{ mol}$	$6.1 \times 10^7 \text{ mol}$	$1.6 \times 10^7 \text{ mol}$
Guay and Falkner [1998]				
$1.6 \times 10^8 \text{ mol}$	$6.8 \times 10^7 \text{ mol}$	$7.8 \times 10^7 \text{ mol}$	$4.0 \times 10^7 \text{ mol}$	$1.3 \times 10^7 \text{ mol}$

Previous observation based estimate of Barium input from Arctic rivers are available Guay and Falkner [1998] for comparison (table 4.1). The model simulation results are similar with larger output from the Lena River and smaller output from the Ob River. Overall the model results are 4% lower mainly due to a 7% lower value for the Mackenzie River.

4.1.2 Oxygen isotope ratio

The surface climatology of Oxygen isotope ratio (figure 4.3, a) varies from -5‰ to 0.5‰ . In the river estuaries, especially along the coast of the East Siberian and the Laptev Seas, Oxygen isotope ratios lower than -10‰ are simulated which reflects the effect of the Eurasian river runoff. The Oxygen isotope ratio in the Greenland Sea, the Barents Sea and the Kara Sea is the highest in the Arctic ocean which shows the contribution of high salinity, high Oxygen isotope ratio water from the North Atlantic. In the Makarov Basin, the Amundsen Basin and Fram Strait, the Oxygen isotope ratio value is about -3.0‰ , lower than the North American side of the Arctic; these low values occur because these regions are in the pathway of the TDS which brings Eurasian runoff into Fram Strait. In Bering Strait and the Chukchi Sea, the high Oxygen isotope ratio reflects the existence of the Pacific inflow.

On an Oxygen isotope ratio versus sea surface salinity plot (figure 4.3, b), most of the results are located in two regions. One can be characterized as a practical salinity range of 34 to 35 and $\delta^{18}\text{O}$ range of 0.5‰ to -0.5‰ . The other one is centered at a salinity of 30 and $\delta^{18}\text{O}$ of -3.0‰ . These two regions represent the Greenland Sea, Barents Sea and Kara Sea water and the Alpha-Mendeleyev Ridge and Makarov Basin Arctic water, respectively (figure 4.3, a). Results with high $\delta^{18}\text{O}$ and low salinity are related to the sea-ice melt water. The low salinity low $\delta^{18}\text{O}$ “tails” are ocean water that has mixed with meteoric water which has very low $\delta^{18}\text{O}$ end-members.

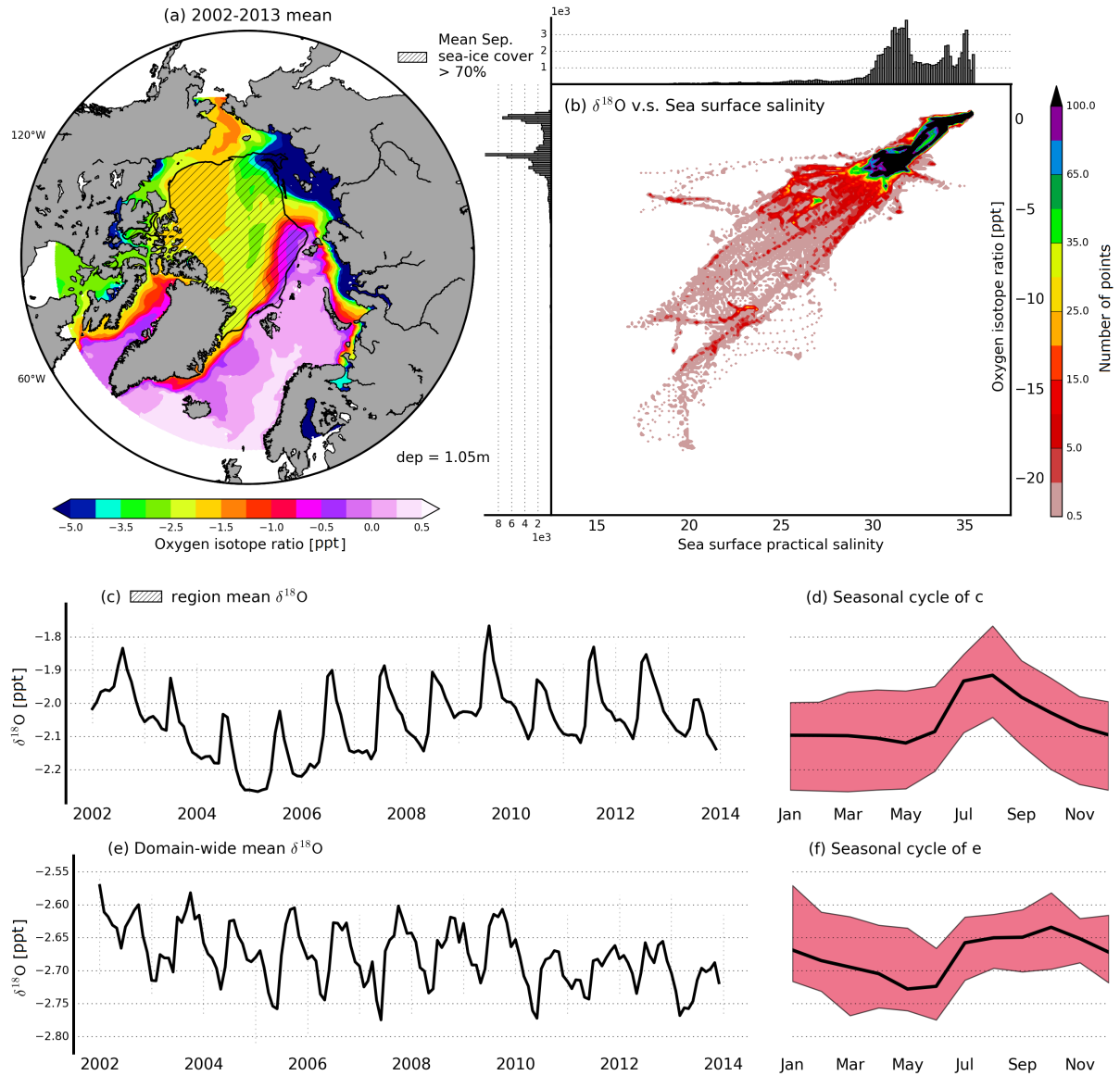


Figure 4.3: Simulated 2002-2013 climatology state of Oxygen isotope ratio at the surface (1.05 m) (a) is the annual mean. (b) is the histogram between the mean surface Oxygen isotope ratio and the sea surface salinity. The shade shows the number of points in each hist bin, the black box indicates the sea-ice melt water. (c) is the Oxygen isotope ratio timeseries that has been averaged in the hatched region. (d) is the seasonal cycle of (c). (e) is the domain-wide mean surface Oxygen isotope ratio. (f) is the seasonal cycle of (e).

The timeseries of Oxygen isotope ratio was averaged horizontally over the region which has 2002-2013 September mean Sea-ice cover larger than 70% (figure 4.3, c). Since September is the sea-ice minimum, sea-ice cover in this month represents the semi-permanent sea-ice covered region. Under the permanent sea-ice, the averaged Oxygen isotope ratio fluctuates by 0.2‰ on a climatological value of $-2.0‰$. The seasonal cycle shows that Oxygen isotope ratio is relatively low and stable during the sea-ice formation period from November to March, and rapidly increases during the summer reaching

its maximum in August. Since sea-ice melt in the tracer model has a higher Oxygen isotope ratio end-member value than meteoric water and Arctic ocean water, the seasonal cycle reflects the impact of sea-ice formation and melt.

The domain-wide mean Oxygen isotope ratio has a larger uncertainty in its seasonality (red shades in figure 4.3, e-f), and the mean state of the domain-wide result is about -2.7‰ , lower than the value under permanent ice. The domain-wide average shows the combined effect of sea-ice variability and meteoric water, especially river runoff. Specifically, during April to June, the spring freshet increases the meteoric water input from Arctic rivers which lowers the Oxygen isotope ratio, but the rising temperature means more sea-ice to melt which increases the Oxygen isotope ratio. During November-March, the decreased river discharge which increases the Oxygen isotope ratio, opposes the sea-ice formation which decreases the Oxygen-18 by fractionation. Therefore, throughout the year, river input and sea-ice melt-formation always counter-act. So when they were both summed up in the (e) timeseries, more small scale perturbations can be found.

4.2 Data model comparisons

4.2.1 Dissolved Barium

Table 4.2: Mean bias and NRSMD of dissolved Barium comparisons

Depth	BGEP	CBL32PZ	NPEO	ARK-XXII/2	HLY0301
Mean bias [nM]					
0-20 m	2.92	5.82	4.25	5.01	1.93
20-60 m	4.00	4.42	9.38	5.05	1.93
60-130 m	-2.48	-5.10	9.34	3.66	4.34
2-4 km	-6.73	-5.77	-	-4.87	-44.01
NRMSD [%]					
0-20 m	8.71	25.12	6.51	14.55	34.94
20-60 m	14.79	28.55	25.11	25.29	32.87
60-130 m	12.26	20.78	29.49	24.72	26.96
2-4 km	47.95	-	-	-	-

Dissolved Barium samples from BGEP (the Beaufort Sea), CBL32PZ (the Chukchi Sea), NPEO (the central Arctic), ARK-XXII/2 (the Nansen Basin and Laptev Sea coast) and HLY0301 (The Nare Strait and Baffin Bay) are compared with the model output and in general show a good agreement on their minimum and maximum ranges (figure 4.4, a-e and h). Both the data and the model output in the Beaufort Sea have the highest mean profiles with strong variations. The BGEP and the CBL32PZ comparisons have the highest overestimation (positive mean bias) in 20-60 m and show an underestimation at 60-130 m and 2-4 km (table 4.2). The NPEO and ARK-XXII/2 comparisons have an overestimation of 4 – 9 nM above 130 m and the ARK-XXII/2 comparison show an underestimation of 4.87 nM at 2-4 km. NPEO observations were only taken down to 400 m, so there is no information in the deep ocean.

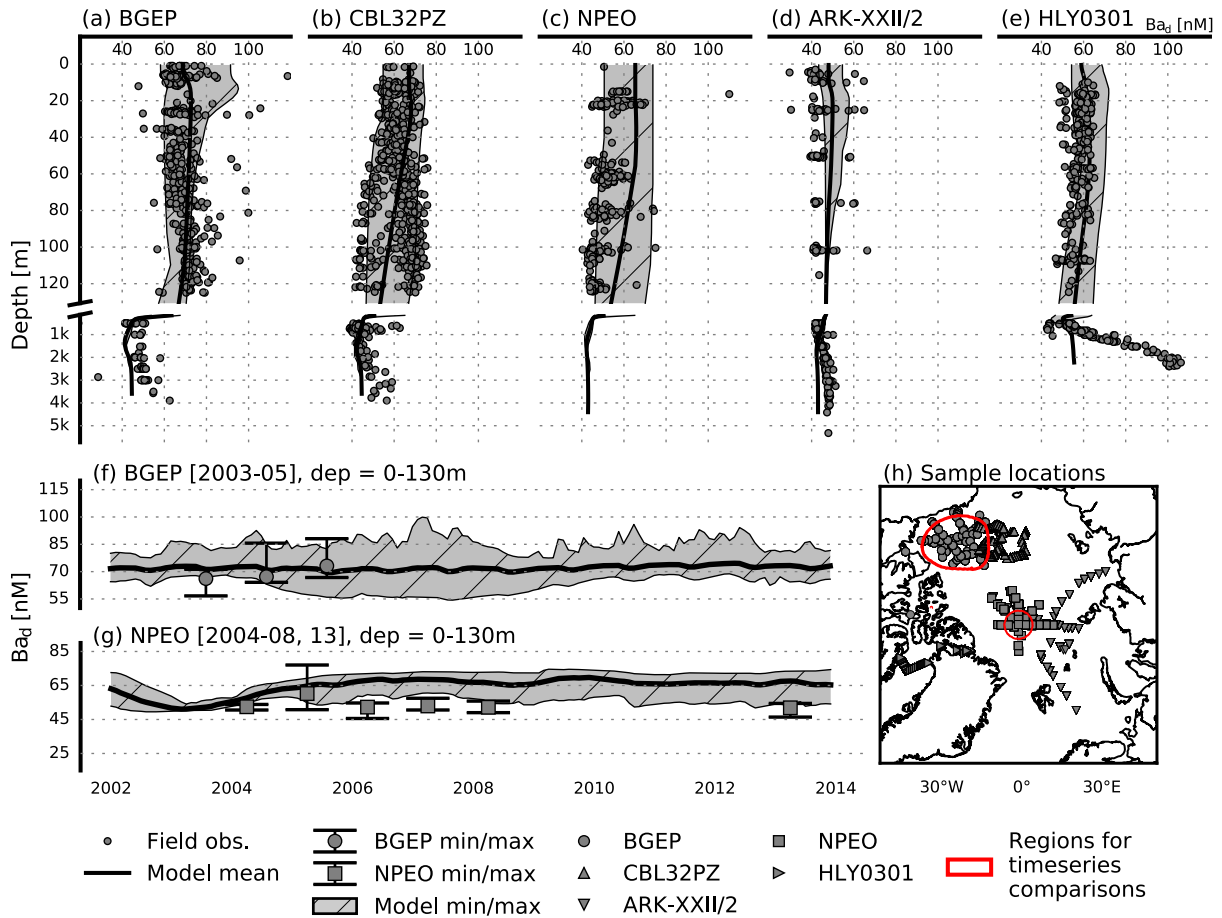


Figure 4.4: The model output of dissolved Barium comparing with BGEF 2003-2005 (a), CBL32PZ 2002 (b), NPEO 2004-2008 and 2013 (c), ARK-XXII/2 2007 (d) and HLY0301 2003 (e) observations. (f) is the timeseries comparison of BGEF data. (g) is the timeseries comparison of NPEO data. (h) shows the locations of all samples. Two red circles are the regions that calculate the model mean, minimum and maximum in (f) and (g).

The HLY0301 comparison has an overestimation on the surface ocean and the mean bias above 60 m is the lowest. In the deep ocean, a strong underestimation can be seen (figure 4.4, e) with the mean bias of 44 nM (table 4.2).

Both the data and model output in the Beaufort Sea have low temporal variation from 2003 to 2005. The comparison of the two is in general good with a slight overestimation of 4 nM in 2003 mean (figure 4.4, f). The timeseries comparison of NPEO data in the central Arctic is good in 2004 and 2005 but overestimation can be seen in 2006-2008 and 2013 with the highest bias of 16 nM in 2013 (figure 4.4, g).

4.2.2 Oxygen isotope ratio

Oxygen isotope ratio results were compared with BGEF (the Beaufort Sea), CBL32PZ (the Chukchi Sea), NPEO (the central Arctic) and HLY0301 (the Nare Strait and Baffin Bay) and in general show

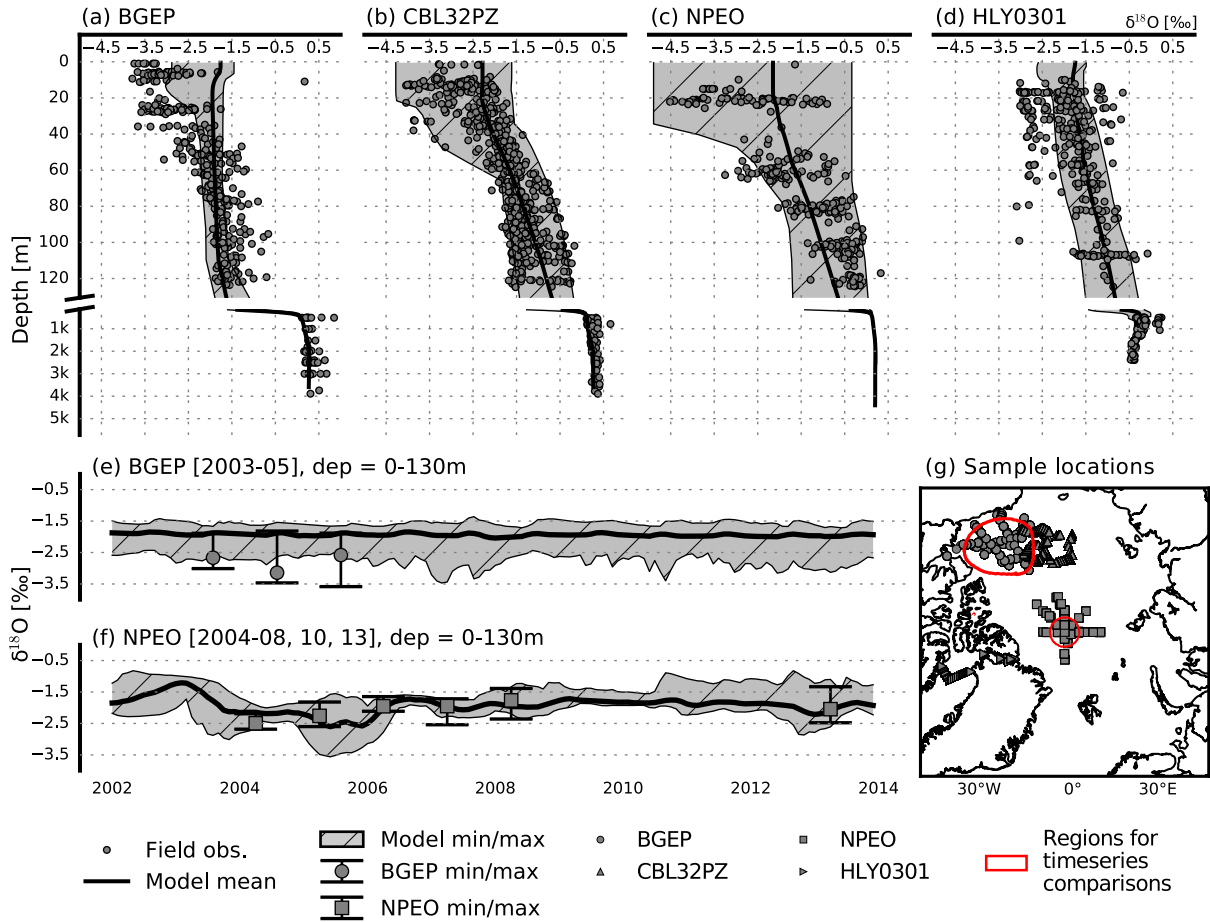


Figure 4.5: Same as figure 4.4 but for Oxygen isotope ratio and without ARK-XXII/2 data.

Table 4.3: Mean bias and NRSMD of Oxygen isotope ratio comparisons

Depth	BGEP	CBL32PZ	NPEO	HLY0301
Mean bias [‰]				
0-20 m	1.11	0.51	0.88	0.41
20-60 m	1.12	0.09	0.47	0.29
60-130 m	0.35	0.14	-0.25	0.08
2-4 km	-0.043	-0.079	-	0.06
NRMSD [%]				
0-20 m	27.57	28.69	15.01	25.58
20-60 m	11.88	19.22	20.30	21.85
60-130 m	6.14	16.69	28.64	8.64
2-4 km	3.62	-	-	-

good agreement (figure 4.5, a-d and g). In the depth range of 0-60 m, an overestimation can be seen in the BGEF comparison with the mean bias of -1.1‰ (table 4.3). The overestimation decreases with increasing depth and shows little impact below 60 m. The comparison in the Chukchi Sea has relatively low model bias; the minimum and maximum of the model output and CBL32PZ data are well matched.

The NPEO data in the central Arctic varies from -4.5% to 0.5% . This high variation is well captured by the model output. The comparison in Baffin Bay with HLY0301 samples shows an overestimation similar to the comparison in the Beaufort Sea but with lower bias. In the deep ocean. The model does better in the 2-4 km deep ocean than at the surface.

The overestimation of about -1.0% at the surface of the Beaufort Sea was found in 2003-2005 in the timeseries comparison (figure 4.5, e), consistent with the overestimation above 60 m in (a). The timeseries comparison of NPEO data in the central Arctic is good, with the model output well captures the observed low values in 2005-2006 and high values in 2006-2007 (figure 4.5, f). By comparing with figure 4.4, f, the model simulates Oxygen isotope ratio better in the central Arctic.

4.3 Linear trends of tracers and Arctic freshwater

The FWC shows a trend over the modeled 12 years. A linear trend was fit to the data (figure 4.6); all other variability is captured in the EOF analysis performed next. The FWC linear trend (figure 4.6, a) is positive in the Beaufort Sea, the East Greenland Sea and the CAA but negative in the Makarov Basin and part of the East Siberian Sea. This contrast between the North American side and Eurasian side of the Arctic is consistent with observed rate of change from 2005 to 2008 [Morison et al., 2012]. The sea surface height (figure 4.6, b) decreases with the FWC. In the Makarov Basin, the negative sea surface height trend and cyclonic surface velocity trend show that Makarov Basin is continuously losing its surface water. In the Canada Basin, East Greenland Sea and CAA, the velocity trend indicates that the eastern side of the Beaufort Gyre and the TDS are intensifying, and simultaneously we can see that the CAA - Baffin Bay transport is weakening as the trend velocity (figure 4.6, a) is out of the CAA and Baffin Bay, against the mean velocity (figure A.2). Dissolved Barium is decreasing in the Makarov Basin (figure 4.6, c), consistent with the decreases of FWC and the sea surface height.

Since dissolved Barium is a tracer of river runoff, decreasing Barium means that the accumulation of Eurasian runoff in Makarov Basin seen in the mean state (figure 4.1, figure A.2) is decreasing. On the North American side of the Arctic, the dissolved Barium is increasing in the eastern Beaufort Sea, Lincoln and East Greenland Seas showing the increased accumulation of runoff water compared to the mean state (figure 4.1, figure A.2). This runoff accumulation is consistent with the intensified Beaufort Gyre and TDS as well as with the FWC increases (figure 4.6). In the CAA, the decreasing Barium but increasing FWC and sea surface imply an accumulation of low dissolved Barium concentration runoff which would come from local CAA river runoff rather than Beaufort Sea originated runoff. Also note that, the positive dissolved Barium trends on the North American side of the Arctic have a larger spatial footprint than the positive trends of FWC. This difference could be related with the shift of Eurasian runoff pathways to the Beaufort Sea due to the cyclonic circulation [Morison et al., 2012] and hence brings more dissolved Barium than usual.

The linear trend of Oxygen isotope ratio is positive in the Makarov Basin, the Laptev Sea, CAA and negative in the East Siberian Sea and Greenland Sea. These patterns are consistent in the opposite sign with dissolved Barium trends and show the decrease and increase of river runoff compared to the mean.

In addition to the linear trends of ANHA4 forcing variables and simulated tracers, a steady increase

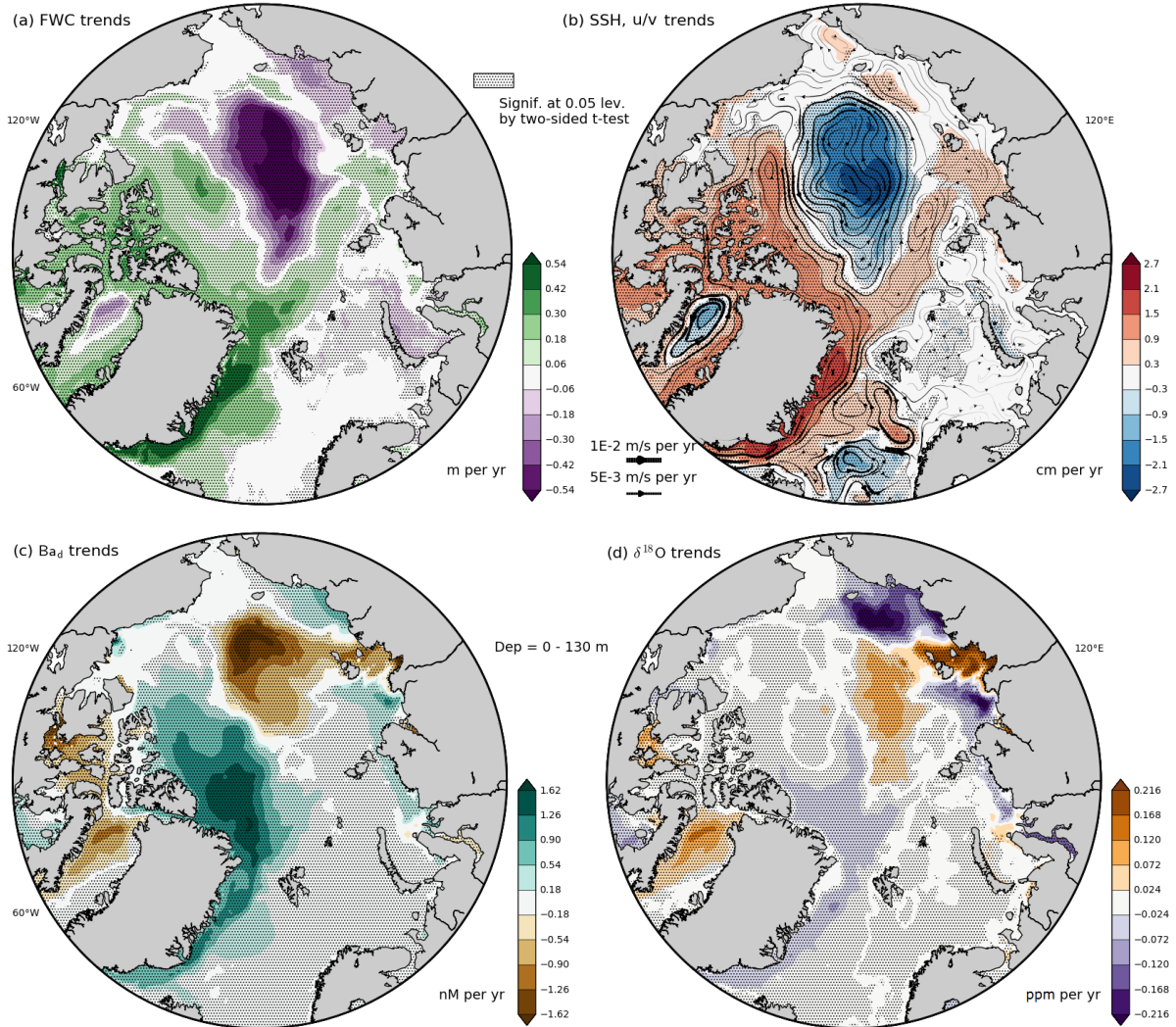


Figure 4.6: The linear trends of FWC (a), sea surface height and ocean velocities (b), dissolved Barium (c) and Oxygen isotope ratio (d). All variables except sea surface height were averaged from 0 to 130 m depth. Dotted regions have trends that have passed a two-sided t-test. Negative/positive sea surface height in (b) delineates regions of cyclonic/anti-cyclonic surface geostrophic flow. The velocity trends shown imply that the eastern side of the Beaufort Gyre and the TDS are intensifying.

of October to next year May AO (winter-spring AO) was found (figure 4.7). From 1950 to 2015, the winter-spring averaged NOAA-CPC AO index shows a steady increase with the slope of 0.009 per year. The CGRF winter-spring averaged AO index from 2002 to 2013 was calculated from CGRF sea level pressure forcing used in the physical model and it agrees with the NOAA-CPC index (see appendix D).

As the AO increases, cyclonic wind stress increases in the East Siberian Sea and Laptev Sea; this causes Ekman divergence which diverges and thus thins the sea-ice. This thinning plays a role on a longer time scale due to the “memory” of sea-ice [Rigor et al., 2002]. Therefore, the linear increase of AO during the simulation period is thought to be the driving factor for the simulated linear trends

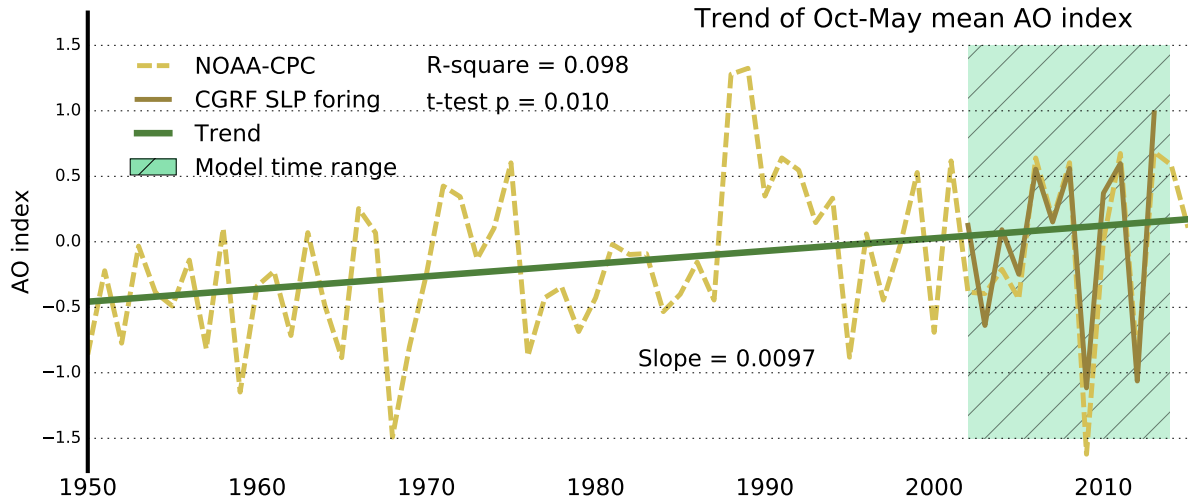


Figure 4.7: The October to next year May averaged AO indices and the linear trend from 1950 to 2015. The orange line is the NOAA-CPC AO index, the brown solid line is the CGRF AO index. The dark green solid line is the result of linear regression with the trend of 0.0097. The R-square is 0.098 and the trend passed 0.01 two-sided t-test.

by producing the Ekman divergence and anomalous cyclonic ocean flow in the Makarov Basin, and the accumulation of surface water in the Beaufort Sea and anticyclonic anomalous wind in the CAA - Baffin Bay region.

4.4 Tracer anomaly patterns and freshwater variability

4.4.1 Mode I: Dipole anomaly

The EOF mode one of FWC (figure 4.8) accounts for 30.7% of the total variance. The spatial pattern has negative FWC anomalies on the northern side of New Siberian Island and in the coastal Laptev Sea, and positive anomalies located in the Beaufort Sea, CAA, the North American side of the central Arctic and extending southward into the East Greenland Sea. The PC of mode one steadily increased from 2002 to 2008 and then decreased, and reaches its negative phase in 2011 winter. The temporal variation of mode one is correlated with the TDS intensity ($r = 0.805$, $p < 0.02$), the latter is calculated as the mean 0-130 m ocean velocity in the hatched region in figure 4.8 (also see section 3.4.5). The spectral power of the PC has a peak at the 1/12 cycle per year frequency band which indicates that mode one may have decadal variabilities. According to the “rule of thumb”, mode one is well separated from its neighbouring modes ([North et al., 1982], section 3.4.4).

In order to determine the atmospheric driving factor of the FWC mode one, the composite anomaly of CGRF and ANHA4 forcing variables was calculated (figure 4.9). The composite anomaly of sea level pressure shows a dipole structure with positive sea level pressure above the Canada Basin, CAA and South Greenland Sea and with negative sea level pressure above the Eurasian side of the Arctic and its marginal seas. The boundary between the two opposite signed anomalies is along a line through the

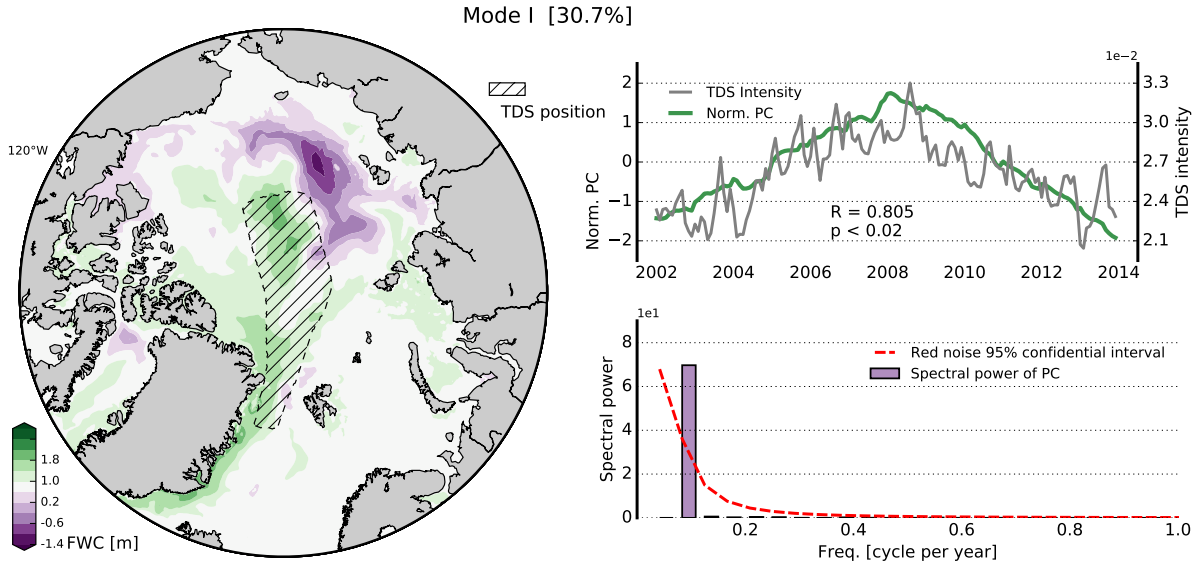


Figure 4.8: The FWC EOF mode one spatial pattern (left), PC (top right green solid line) and the spectral energy of PC (bottom right). The gray line on the top right is the TDS intensity estimated by the mean horizontal speed of surface ocean currents in the hatched region (see section 3.4.5). The red dashed line is the 95% red noise test confidential interval.

Chukchi Sea - central Arctic - Fram Strait. This anomalous pattern has been previously named as the atmospheric dipole anomaly and is independent from other atmospheric teleconnections including AO and NAO [Watanabe et al., 2006, Wu et al., 2006] (see appendix D). During the positive phase of mode one, the dipole pattern in the sea level pressure causes strong meridional wind in the central Arctic, anticyclonic wind with negative wind stress curl in the Canada Basin and cyclonic wind with positive wind stress curl in the Eurasian Basins. Due to the generated surface Ekman flux, the sea surface height drops on the Eurasian side, and rises on the North American side of the Arctic. This sea surface height anomaly pattern creates strong pressure gradients in the central Arctic and intensifies the TDS, which explains the high positive correlation between mode one PC and TDS intensity (figure 4.8). Therefore, considering the dipole structure of sea level pressure anomalies, the meridionality of the wind stress in the central Arctic and the fact that 2007-2008 is the peak of the mode one PC and also a well studied positive dipole anomaly stage [Wang et al., 2009], we suggest the atmospheric dipole anomaly as the driving factor of the mode one.

During the positive phase of the dipole anomaly, the Eurasian oriented freshwater is transported further northeast, freshening the central Arctic. The anomalous anticyclonic flow in the East Siberian Sea causes the river runoff to accumulate. The strong TDS brings more freshwater southward to Fram Strait and stretches the positive FWC anomaly pattern. The anomalous anticyclonic flow, as well as the positive sea surface height in the CAA, blocks and slows down the CAA - Baffin Bay transport, but causes the local CAA runoff to accumulate due to Ekman convergence. Therefore the effect of less Beaufort Sea runoff is compensated by the accumulation of CAA local runoff and no big FWC anomaly can be seen in the CAA.

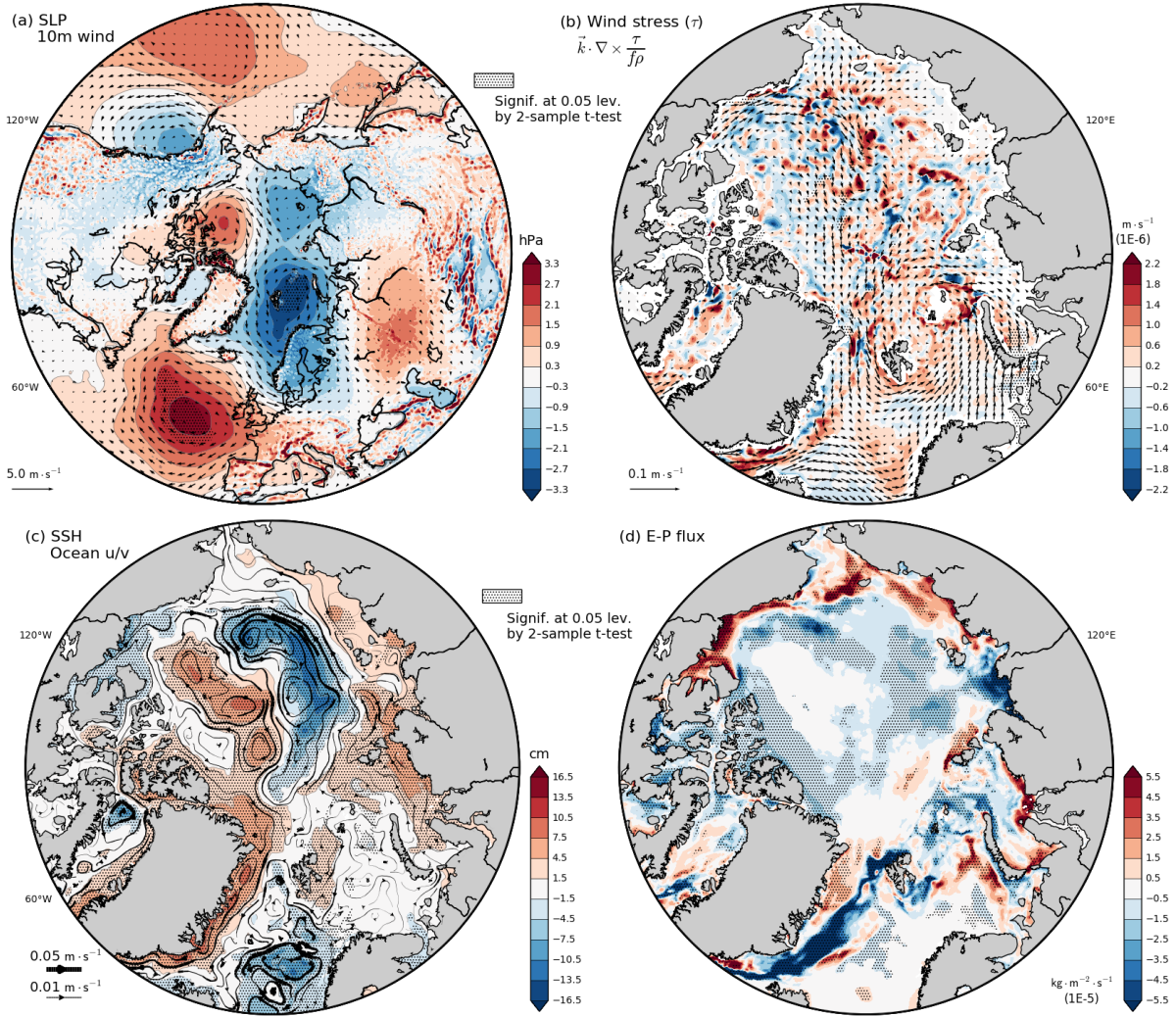


Figure 4.9: The composite anomalies for mode one PC. Composite anomalies are difference between high phase and low phase (section 3.4.4). sea level pressure, 10 m winds (a), wind stress, wind stress curl (b), sea surface height, ocean velocities above 130 m (c) and E-P flux (d). Dotted regions have composite anomalies pass the 0.05 level t-test.

The $E - P$ composite anomaly is negative which indicates strong sea-ice melt on the northern side of the Chukchi Sea and over most of the Eurasian side of the Arctic (figure 4.9, d). This anomalous sea-ice melt is consistent with previous studies, which found that the dipole anomaly enhances oceanic heat flux through Bering Strait and increases the summer sea-ice melt [Wang et al., 2009, Wu et al., 2006].

In mode one, a strong positive anomaly for dissolved Barium shows in the central Arctic, and negative anomalies in the Makarov Basin and CAA (figure 4.10, a). As dissolved Barium is a tracer of runoff water, the negative pattern in the Makarov Basin indicates a reduction in the transport of the East Siberian Sea and Laptev Sea runoff as a response of the eastward anomalous flow along the Russian coast and the anomalous flow from the Laptev Sea to the Makarov Basin (figure 4.10, c). The negative

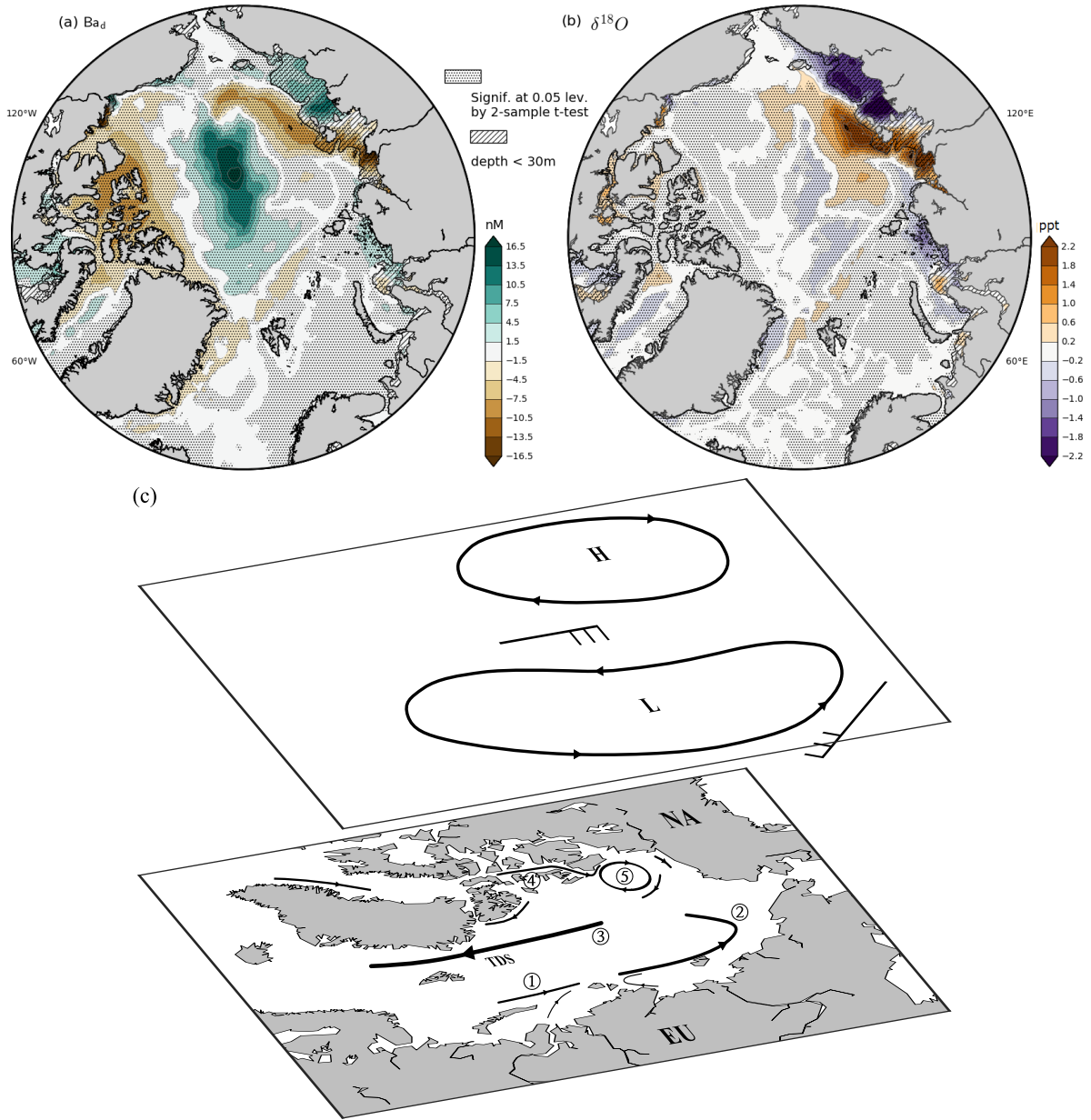


Figure 4.10: The composite anomaly of dissolved Barium (a) and Oxygen isotope ratio (b) in mode one PC and averaged above 130 m. Hatched regions in (a-b) are shallower than 30 m. Dotted regions in (a-b) have composite anomaly pass the 0.05 level two-sample t-test. (c) is the sketch of anomalous flow pattern, both in the lower atmosphere (top plane) and the surface ocean (lower plane). On the upper plane, the dipole anomaly with enhanced high pressure over the Beaufort Sea and enhanced low pressure over the Eurasian Side. Wind barbs show the anomalous winds. On the lower plane, circles show the major anomalous currents; ① and ② transports the Eurasian runoff to the Makarov Basin; ③ is the anomalously strong TDS; ④ indicates the weak CAA - Baffin Bay transport and ⑤ is the intensified Beaufort Gyre.

dissolved Barium anomaly in the CAA and the positive anomaly in the northern Canada Basin indicates that, due to the anomalous anticyclonic flow in the Beaufort Sea and the anomalous flow from CAA channels to the Beaufort Shelf, Beaufort Sea runoff is trapped by the Beaufort Gyre instead of exiting through the CAA - Baffin Bay route. The positive dissolved Barium anomaly in the central Arctic from the Chukchi Sea to the Fram Strait shows the accumulation of runoff water in the strong transport by the anomalously strong TDS.

The composite anomaly for Oxygen isotope ratio shows a positive anomaly in the Laptev Sea, consistent with the negative dissolved Barium anomaly and shows the transport of runoff from the Eurasian marginal seas to the Makarov Basin and the central Arctic. The negative Oxygen isotope ratio anomaly in the coastal East Siberian Sea, concentrated in shallow water, indicates the accumulation of East Siberian Sea runoff. In the Makarov Basin and further north, a negative Oxygen isotope ratio anomaly of less than -0.2‰ can be seen. This anomaly shows the appearance of Eurasian runoff in the central Arctic.

Compared to the positive dissolved Barium composite anomaly in the central Arctic, the footprint of negative Oxygen isotope ratio anomaly is only about half the area, which indicates that, North American river and Eurasian river inputs have about the same total amount input of Barium (see table 4.1). However for Oxygen isotope ratio, which has end-member values of about -20‰ for all Arctic rivers, the Eurasian rivers, which have higher discharge, have a larger impact. This difference also explains the contrast between the positive FWC anomaly and the negative dissolved Barium composite anomaly in the East Greenland Sea. The Oxygen isotope ratio anomaly in the East Greenland Sea is negative, which implies the accumulation of meteoric water (figure 4.10, b). However, the negative dissolved Barium anomaly in the same region implies this meteoric water is not typical, high Barium concentration North American runoff but is more likely to be Eurasian runoff or low dissolved Barium concentration CAA runoff.

4.4.2 Mode II: The interannual effect of NAO

The FWC EOF mode two (figure 4.11) accounts for 14.0% of the total variance. The spatial pattern shows negative FWC anomalies in the East Siberian Sea, on the northern side of the Canada Basin and near New Siberian Island, and positive FWC anomalies in the Chukchi Sea and over part of the Makarov Basin. The PC of mode two underwent a steady increase from 2002 to 2004, switched from the negative to positive phase, then stabilized in the positive phase from 2004 to 2008. In 2008-2010, it went back to its negative phase and then had a steady increase from 2010 to 2013. The temporal variation of the mode two PC has a good positive correlation with the 1-year moving average NOAA-CPC NAO index ($r = 0.378$, $p < 0.1$) and with the 1-year moving average NAO index calculated from the CGRF sea level pressure forcing ($r = 0.495$, $p < 0.05$, appendix D). The spectral power of the PC has peaks at the 1/12 and 1/8 cycle per year frequency bands. Mode two is well separated from its neighbouring modes by the “rule of thumb” ([North et al., 1982], section 3.4.4).

The composite anomaly of sea level pressure has a negative anomaly over the Baffin Bay and the Greenland and Nordic Seas. The negative anomaly is surrounded by two positive anomalies, one located

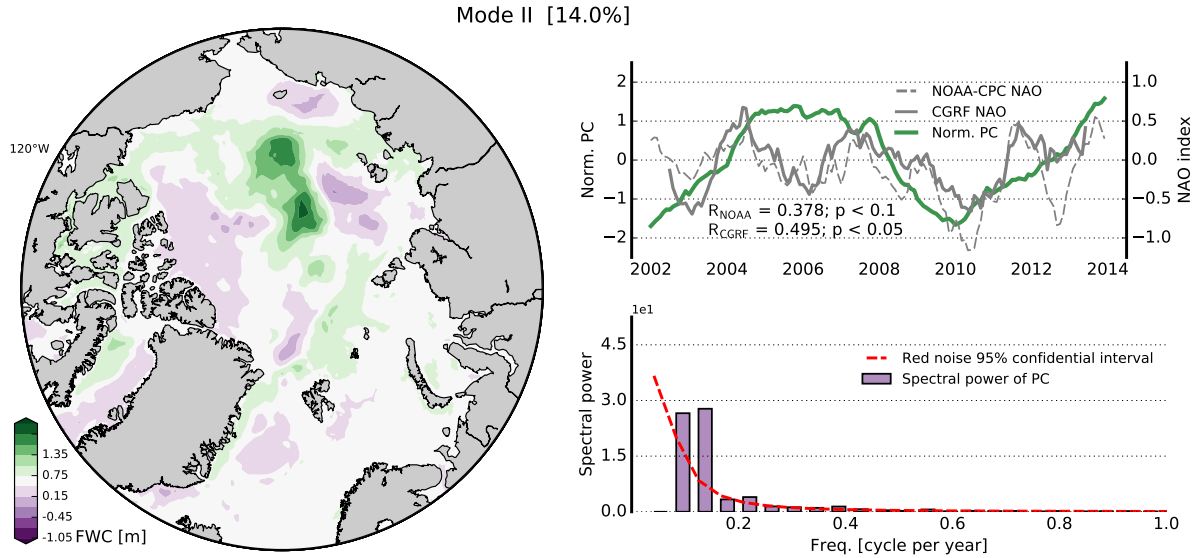


Figure 4.11: The FWC EOF mode two spatial pattern (left), PC (top right green solid line) and the spectral energy of PC (bottom right). On the top right plot, the gray dashed line and gray solid line are the 1-year moving averaged NOAA-CPC NAO and CGRF NAO indices (see section 3.4.5). The red dashed line is the 95% red noise test confidential interval.

over the North Atlantic Ocean and the other one located over the North Pacific Ocean. The composite anomaly of mode two sea level pressure is similar to the NAO pattern [Hurrell, 1995].

The composite anomaly of near surface wind stress curl shows a positive anomaly in the East Greenland Sea, Nansen Basin and Canada Basin during the positive phase of mode two, consistent with the negative sea level pressure. Anticyclonic wind and negative wind stress curl occurs on the Pacific side of the Arctic including the Chukchi Sea and the East Siberian Sea. As a result, due to the surface Ekman flow, the sea surface height is depressed in both the Canada Basin and Nansen Basin, and rises in the Chukchi Sea and the Eurasia marginal seas as shown in the sea surface height composite anomaly (figure 4.12).

Due to the spatial distribution of sea level pressure composite anomaly and the significant positive correlation between mode two PC and NAO indices, NAO is thought to be the atmospheric driver of mode two. During the positive phase of the NAO, the cyclonic anomalous wind on the North American side of the Arctic spins-down the Beaufort Gyre and intensifies the CAA - Baffin Bay transport. Meanwhile the anticyclonic anomalous winds on the Pacific side of the Arctic increase the surface FWC in the Makarov Basin. Also, the anomalous flow pattern along the Eurasian coast brings more East Siberian Sea runoff to the eastern side of the Laptev Sea and then transports it further north, so the pathway of Eurasian marginal sea runoff is also changed. Different from mode one, mode two does not have a large $E - P$ composite anomaly, only a small sea-ice melt signal can be seen near the Eurasian coast.

A positive dissolved Barium anomaly can be seen in the Chukchi Sea, the Makarov Basin, Baffin Bay and the southern part of CAA. Strong negative anomalies are located in the East Greenland Sea, the northern side of the Beaufort Sea and the northwestern side of CAA. The contrast between the

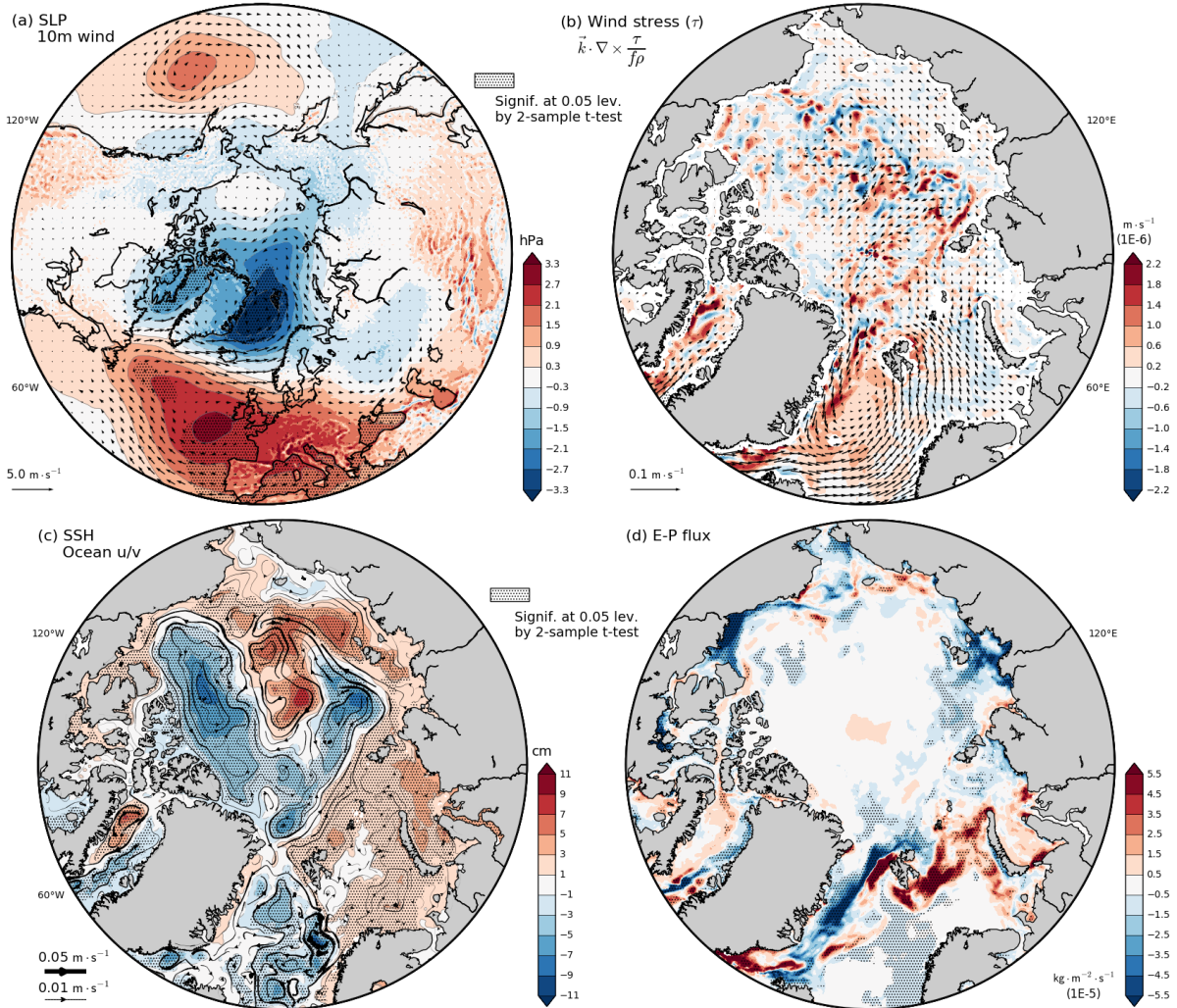


Figure 4.12: Same as figure 4.9, but for mode two

negative dissolved Barium composite anomaly in the Beaufort Sea and the positive anomaly in CAA, especially in Lancaster Sound and Barrow Strait, indicates that the weakening of the Beaufort Gyre during the mode two positive phase encourages more North American runoff to go the CAA - Baffin Bay route which is a reverse of the mode one positive phase (figure 4.10). The positive dissolved Barium composite anomaly in Makarov Basin reveals the transport and accumulation of Eurasian runoff water (figure 4.13).

The composite anomaly of Oxygen isotope ratio mainly shows the change of meteoric water, especially Eurasian runoff, since mode two does not have significant impact on the sea-ice variability. A strong positive anomaly in the East Siberian Sea, and a negative anomaly in the coastal Laptev Sea can be seen. Both are consistent with the dissolved Barium composite anomalies and show the transport of Eurasian marginal seas runoff. Meanwhile, from the Laptev Sea to Fram Strait, the negative Oxygen isotope ratio anomaly which is characterized by the -0.2‰ isoline, shows the accumulation of Eurasian runoff in the Makarov Basin and the change of its pathway to the Fram Strait (figure 4.12).

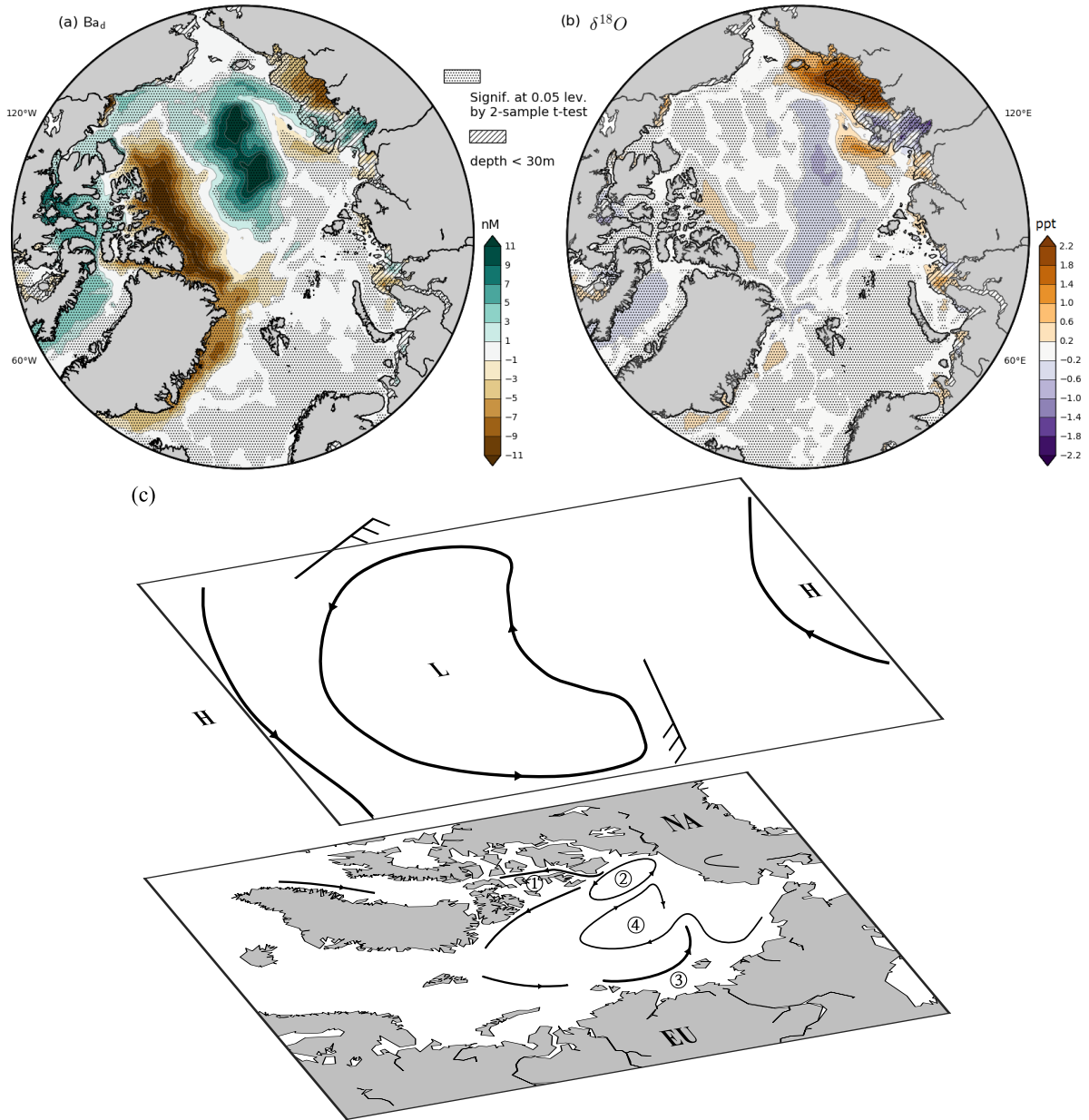


Figure 4.13: Same as figure 4.10, but for mode two. (c) is the sketch of anomalous flow pattern. In the the lower atmosphere (top plane), the NAO-like anomaly with positive pressure over the North Atlantic and enhanced low pressure over the central Arctic/Nansen Basin. In the surface ocean (lower plane), circles show the major anomalous currents; ① and ② are the intensified CAA - Baffin Bay transport with a weak Beaufort Gyre; ③ is the transport of Laptev Sea runoff; ④ is the accumulation of runoff water in the Makarov Basin.

4.4.3 Mode III: The Beaufort Sea high

The FWC EOF mode three (figure 4.14) accounts for 7.8% of the total variance. The spatial pattern shows negative FWC anomalies in the Beaufort Sea and along the East Siberian Sea coast, and positive FWC anomalies in the Canada Basin and the Makarov Basin. Comparing to modes one and two, the

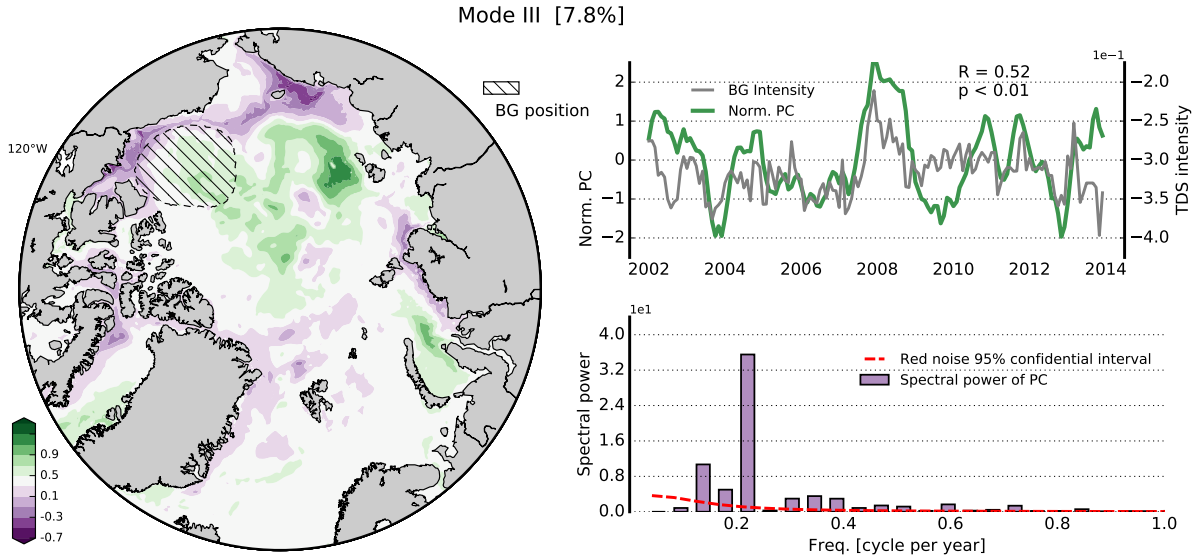


Figure 4.14: The FWC EOF mode three spatial pattern (left), PC (top right green solid line) and the spectral energy of PC (bottom right). The gray line on the top right plot is the Beaufort Gyre intensity estimated as the maximum sea surface height in the Beaufort Sea (see section 3.4.5). The red dashed line is the 95% red noise test confidential interval.

magnitude of the mode three spatial pattern is relatively low, and about half of mode one's. The difference reflects the relative importance of these three modes. The PC of mode three has more short time fluctuations than the previous modes. In general it can be characterized by the peak from winter 2007 to spring-summer 2008 and troughs in winter 2004, fall-winter 2009 and spring 2013. The temporal variation of mode three has a good positive correlation with the Beaufort Gyre intensity ($r = 0.52$, $p < 0.01$) which was estimated as the maximum sea surface height in the hatched region in figure 4.14 (also see section 3.4.5). The spectral power of the mode three PC has a peak at 1/4 cycle per year frequency band and has relatively higher spectral power in 1/2 cycle per year frequency bands than other the two modes. Mode three is well separated from its neighbouring modes by the “rule of thumb” ([North et al., 1982], section 3.4.4).

The composite anomaly of sea level pressure has a large negative anomaly that covers almost the entire Arctic Ocean. Low anomaly centers locate at the Eurasian coast and the southern part of Greenland. In the Beaufort Sea, the negative sea level pressure composite anomaly is relatively weak. An anticyclonic wind stress pattern can be seen in the Arctic, consistent with the sea level pressure anomalies. This anticyclonic wind pattern creates positive sea surface height in the Canada Basin and the Makarov Basin due to Ekman convergence, strongly intensifies the Beaufort Gyre, accumulates freshwater and therefore is considered as the atmospheric driving factor for the FWC mode three. The $E - P$ composite anomaly shows a sea-ice melt signal in the Fram Strait and the Barents Sea, and a sea-ice formation signal in the Beaufort Sea and along the East Siberian Sea coast. The latter is consistent with the negative FWC anomaly pattern (figure 4.15).

A strong positive dissolved Barium anomaly occurs in the Beaufort Sea, North American side of

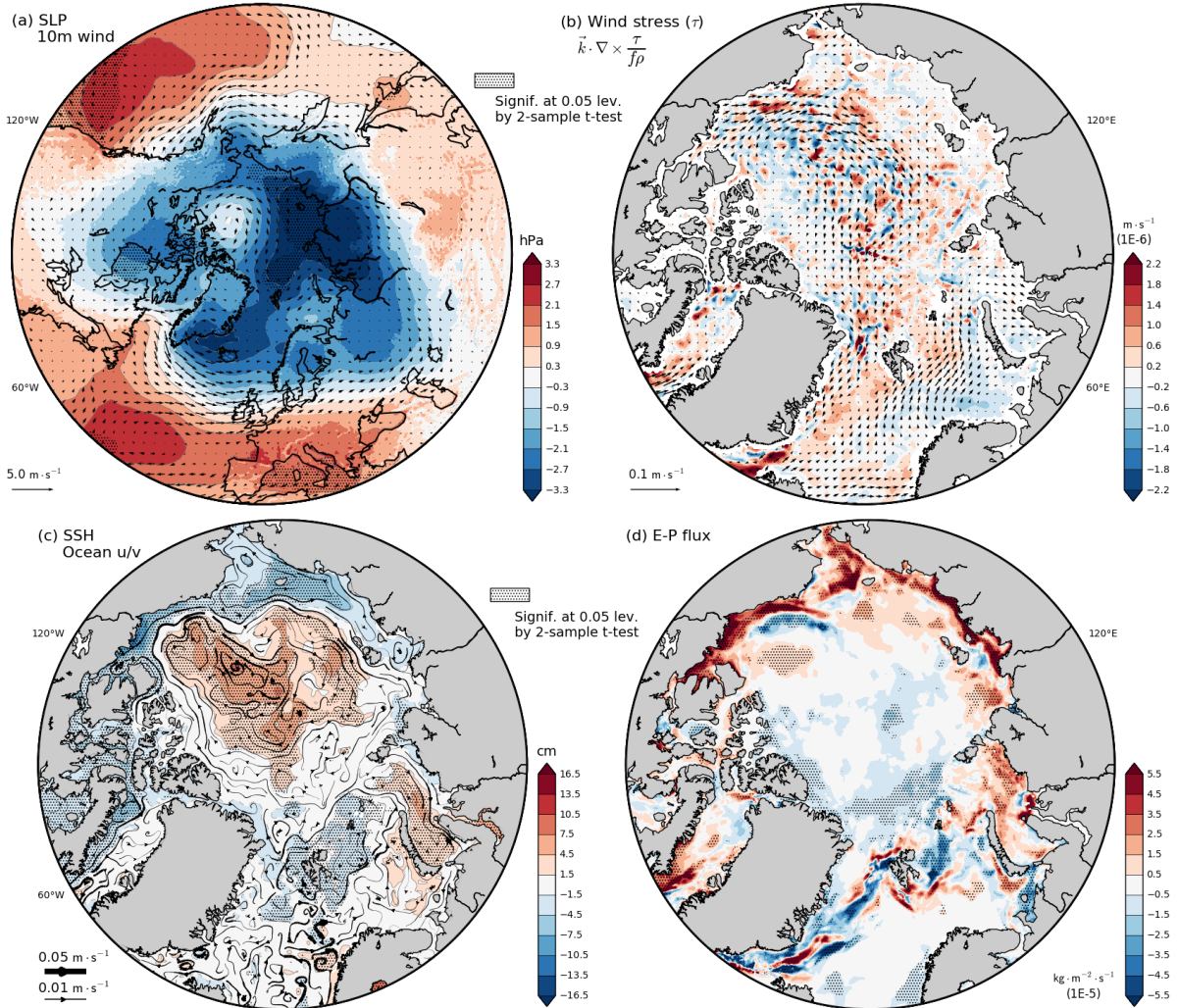


Figure 4.15: Same as figure 4.9, but for mode three

the Arctic, the Lincoln Sea and along the East Greenland coast. Negative dissolved Barium composite anomalies occur in the CAA and the Baffin Bay. On the Eurasian side of the Arctic, the dissolved Barium composite anomaly is scattered with positive anomalies on the northern side of New Siberian Island and negative anomalies in the Laptev Sea and over part of the Mendeleev Ridge. The positive anomaly in the Beaufort Sea and the negative anomaly in the CAA shows the role of an extra strong and extended Beaufort Gyre, which stores extra runoff. This response is the same as mode one (figure 4.10) and the reverse of mode two (figure 4.13). On the Eurasian side, the positive dissolved Barium anomaly on the northern side of New Siberian Island shows the impact of the anticyclonic flow and the westward anomalous flow along the East Siberian Sea coast, produced by the Ekman convergence. The composite anomaly of Oxygen isotope ratio has a positive anomaly on the Eurasia coast, showing the role of sea-ice melt (figure 4.15). Meanwhile its negative anomaly on the northern side of the New Siberian Island and the Kara Sea coast are consistent with the positive dissolved Barium anomaly in figure (figure 4.16, a) and reflect the accumulation of Eurasian runoff.

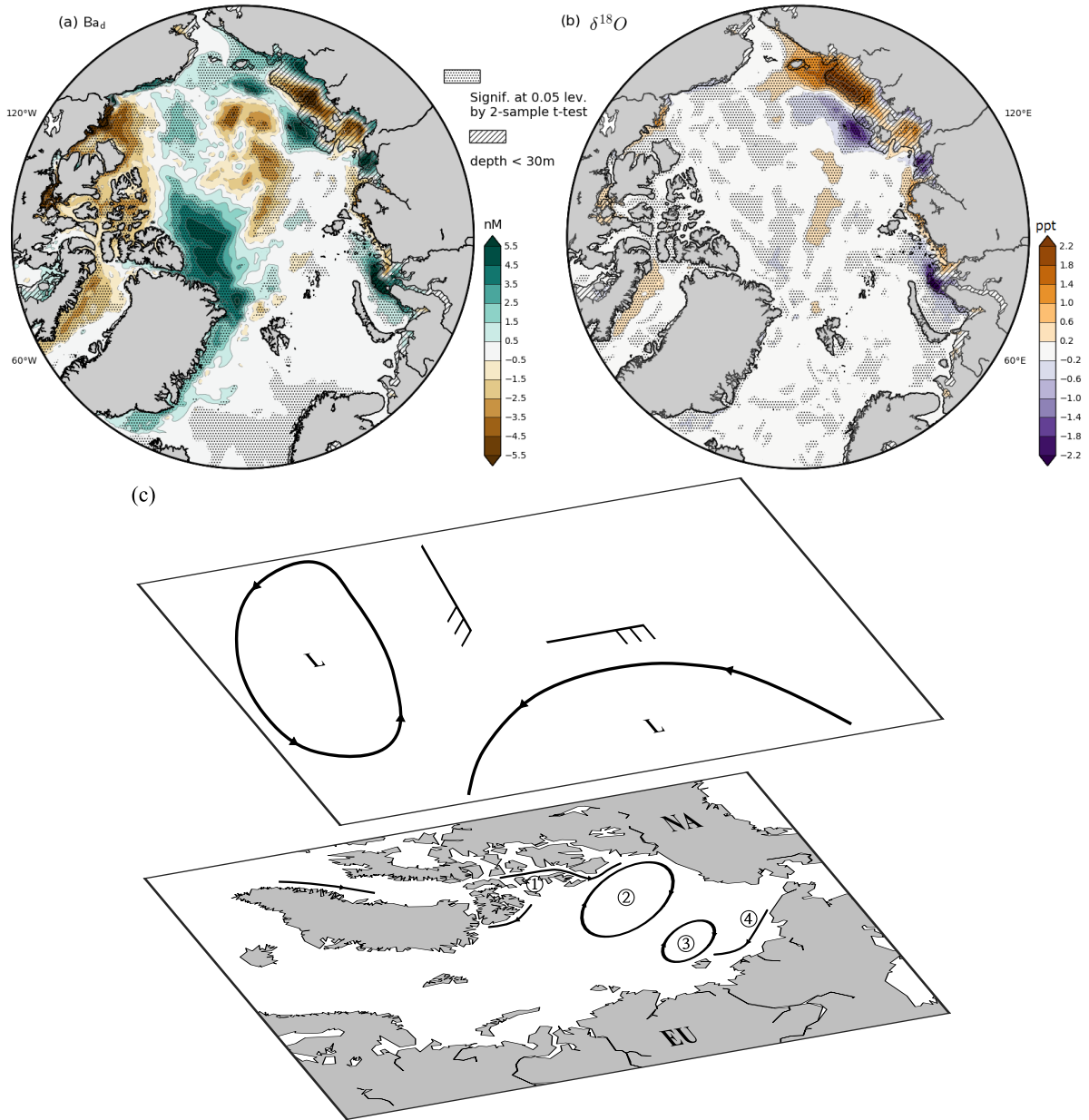


Figure 4.16: Same as figure 4.10, but for mode three. (c) is the sketch of anomalous flow pattern. In the the lower atmosphere (top plane), the enhanced low pressure over the North Atlantic and Eurasian side of the Arctic intensifies the Beaufort Gyre. In the surface ocean (lower plane), circles show the major anomalous currents; ① is the weak CAA - Baffin Bay transport; ② and ③ are the anticyclonic flow in the Beaufort Sea and the northern side of New Siberian Island; ④ is the transport of East Siberian Sea runoff.

4.5 Application: A case study of Beaufort Gyre 2007-2008

The Beaufort Gyre is the biggest freshwater reservoir in the Arctic Ocean [Proshutinsky et al., 2009] and plays an important role in regulating the Arctic climate [Proshutinsky et al., 2002]. According to many studies, freshwater has accumulated in the past few decades in the Beaufort Gyre, and especially

in the 2007-2008 period. Hydrographical observations show that in March-April 2008, the Beaufort Gyre FWC rapidly increased, compared with the 1970s and 1980s winter season climatology in the Polar Hydrographic Climatology (PHC) dataset [McPhee et al., 2009]. The FWC in Beaufort Sea and the southern Canada Basin in 2006-2008 was higher than in 1992-1999 [Rabe et al., 2011]. The Arctic Ocean Model Intercomparison Project (AOMIP) models applying the wind forcing of 2007, all show a similar accumulation of 14m-22m of FWC in the Beaufort Gyre [Proshutinsky et al., 2011]. Finally, at the end of 2008, the Arctic Ocean, predominately, the Canada Basin had gained four times more freshwater water compared to the “Great Salinity Anomaly” period [Morison et al., 2012]. Different theories have been posed to explain the rapid change of freshwater, including the “Flywheel” theory [Proshutinsky et al., 2002], impacts of atmospheric factors like NAO [Condrón et al., 2009] and AO [Morison et al., 2012, Zhang et al., 2003], changes in the Pacific Summer Water (PSW) [Jackson et al., 2011] and the sea-ice decline [McPhee et al., 1998].

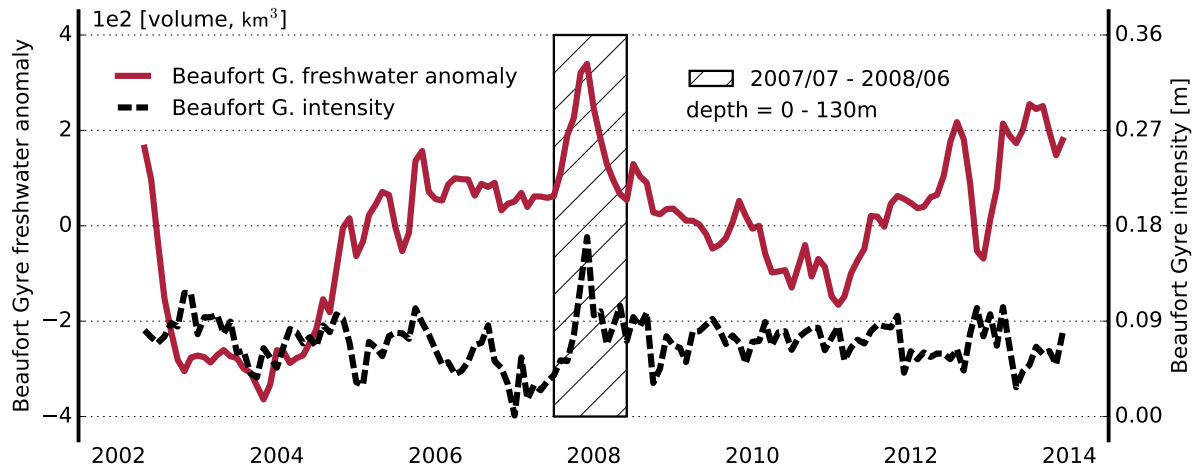


Figure 4.17: The Beaufort Gyre freshwater anomaly above 130 m as volume (red, left axis) and the Beaufort Gyre intensity (black, right axis, see section 3.4.5), the hatched region is the time span of the case study.

The increase of the Beaufort Gyre FWC in 2007-2008 is simulated by the ANHA4-EXH005 experiment (figure 4.17). From summer 2007 to 2008, a significant increase can be seen in both the Beaufort Gyre intensity and its anomaly of freshwater volume above 130 m. The following section will diagnose the increase of Beaufort Gyre FWC by CGRF and ANHA4-EXH005 forcing and the tracer simulation. This case study will provide an example of how the EOF based “idealized” FWC anomaly patterns in section 4.4 can be projected onto a given case, and how the simulated dissolved Barium and Oxygen isotope ratio can be used in the analysis of freshwater components.

4.5.1 Evolution of the FWC anomaly

The evolution of the Beaufort Gyre FWC increase can be divided into three stages: a developing stage (summer 2007), a mature stage (winter 2007- spring 2008) and a vanishing stage (2008 summer), In the developing stage, a dipole-like anomaly pattern is seen with a positive sea level pressure anomaly on

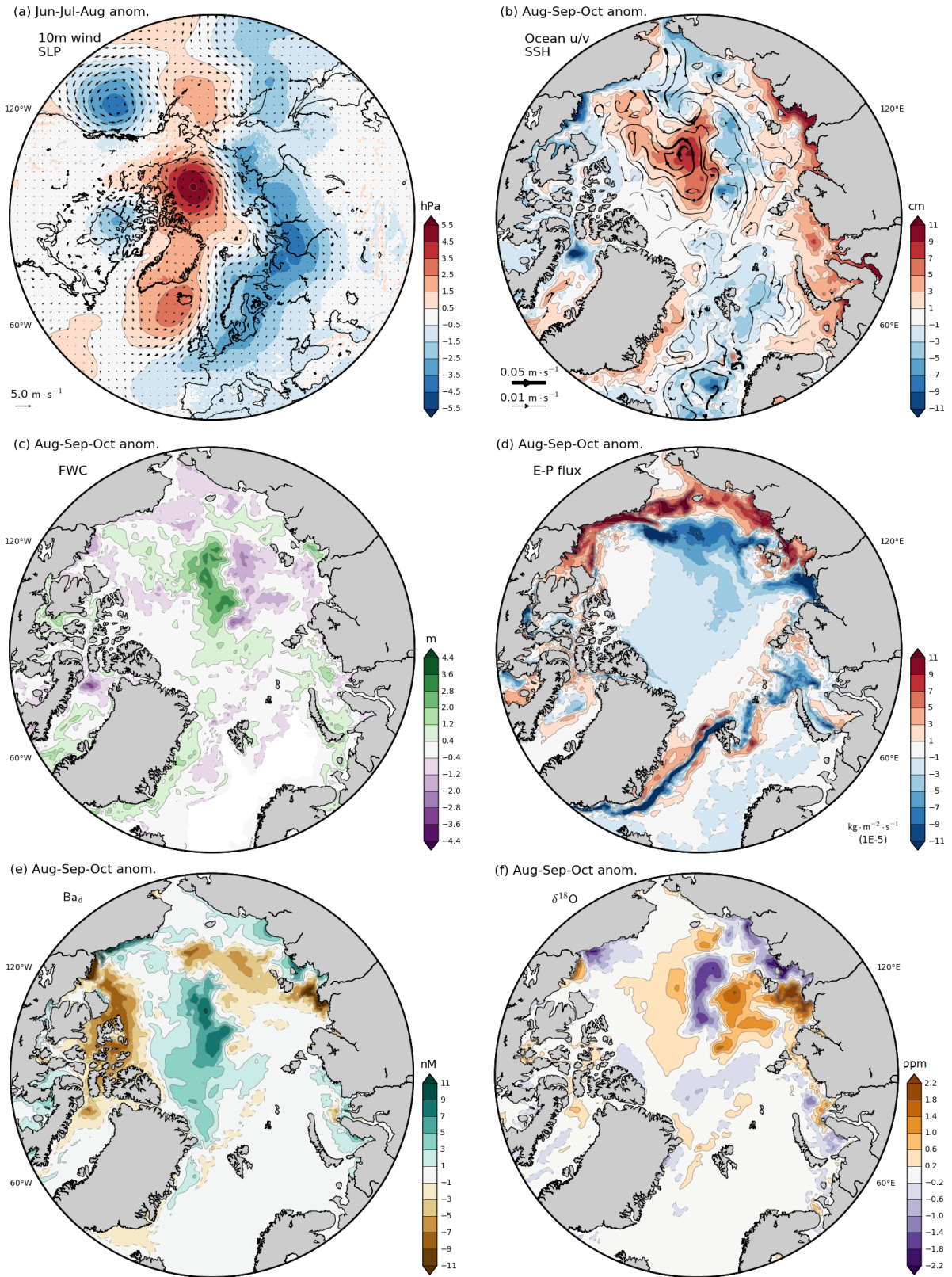


Figure 4.18: 2007 June-August mean sea level pressure and 10 m wind anomaly (a). August-October mean sea surface height, ocean velocities (b), FWC (c), $E - P$ (d), dissolved Barium (e) and Oxygen isotope ratio (f) anomalies.

the North American side of the Arctic, which extends southward to the Greenland Sea and with a negative sea level pressure anomaly on the Eurasian side of the Arctic. Similar to FWC EOF mode one (section 4.4.1), the meridionality of the sea level pressure anomaly creates a strong meridional wind in the central Arctic, and results in surface Ekman transport from Eurasian side to the North American side of the Arctic. This process is consistent with the positive sea surface height anomaly in the central Arctic, and the negative anomaly in the Makarov Basin (figure 4.18). Comparing to the mode one dipole anomaly pattern, 2007 summer has a stronger North American side positive sea level pressure anomaly, but in general, the 2007 anomaly pattern provides the same cyclonic flow in the Makarov Basin and the Eurasian runoff accumulation in the central Arctic. The dipole anomaly has an impact on the Arctic summer sea-ice melt (section 4.4.1) and therefore negative $E - P$ and positive Oxygen isotope ratio anomalies can be seen on the Eurasian side of the Arctic, this sea-ice melt signal also contributes to the increase of FWC.

Thus in the developing stage (2007 summer), the dipole anomaly driven accumulation of Eurasian runoff water in the central Arctic is the most important process. The strong summer sea-ice melt also contributes to the FWC anomaly.

In the mature stage (winter 2007 - spring 2008, figure 4.19), the Beaufort Gyre intensity reaches its peak and so does the Beaufort Gyre FWC. A strong negative anomaly in sea surface pressure occurs over the southern part of Greenland and on the Eurasian side of the Arctic, while in the Canada Basin, the sea level pressure is slightly positive. This sea level pressure anomaly pattern is similar to the atmospheric driving force in FWC mode three (section 4.4.3). An important feature of this pattern is the strong anticyclonic surface wind anomaly in the Canada Basin (figure 4.18 and compare figure 4.15). Under the impact of this anomalous anticyclonic wind, the Ekman convergence raises the sea surface height, strongly intensifies the Beaufort Gyre and makes it extend further into the central Arctic. Since in this case the sea level pressure anomaly in Canada Basin is more positive than for the mode three case, so the intensification of the Beaufort Gyre is stronger (figure 4.19).

During the developing stage (2007 summer), Eurasian runoff water accumulated in the central Arctic due to the dipole-like anomalies. Therefore, in the mature stage, when the Beaufort Gyre is intensified and extends into the central Arctic, its anticyclonic surface circulation and Ekman convergence moves the accumulated Eurasian runoff to the Canada Basin. Indeed a “tail” can be found on the North American side of the positive FWC anomaly, which indicates the effect of Eurasian runoff transport. The positive dissolved Barium anomaly in the Canada basin grows stronger (figure 4.19).

During the mature stage (winter 2007 - spring 2008), the anticyclonic anomalous wind in the Canada Basin intensifies the Beaufort Gyre, makes it extend into the central Arctic where it entrains the pre-existing pool of Eurasian runoff. Therefore, both the FWC and Beaufort Gyre sea surface height reach their maximums.

The increase of the Beaufort Gyre FWC from 2007 to 2008 has two major contributors: the existence of accumulated Eurasian runoff in the central Arctic and a strong Beaufort Gyre. Thus, when either of these two factors are undermined, the situation will become less suitable for the increase of Beaufort Gyre FWC, and it starts to vanish (summer 2008). The magnitude of sea level pressure anomaly during

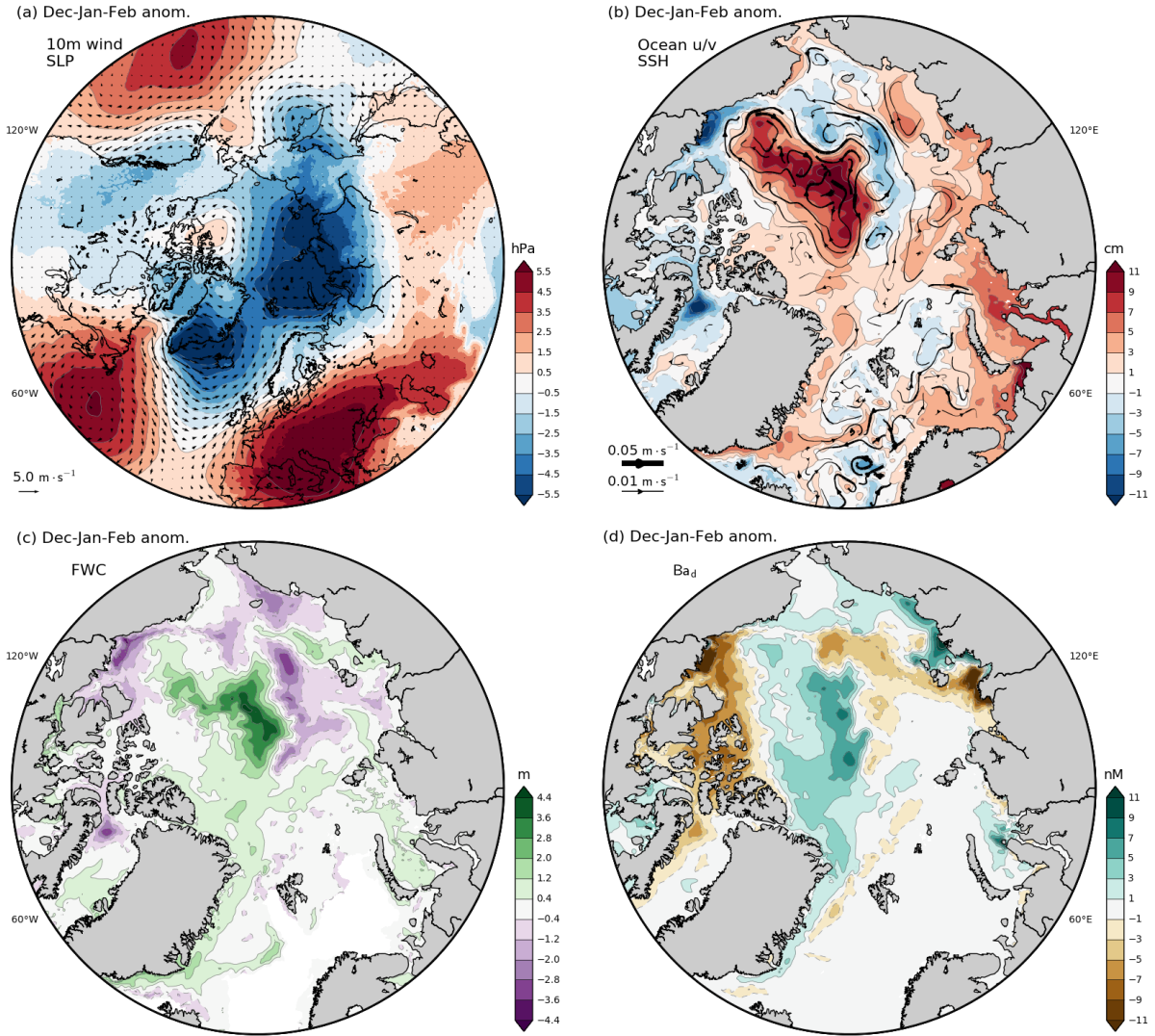


Figure 4.19: Same as figure 4.18, but for December-February mean, no $E - P$ and $\delta^{18}\text{O}$ anomalies.

the vanishing stage is lower than the developing and mature stages (figure 4.20), which means that the sea level pressure in the vanishing stage approaches climatology. In the Canada Basin, a negative sea level pressure anomaly with cyclonic anomalous wind occurred, which indicates that, in the vanishing stage, the atmospheric forcing does not support the growth of the Beaufort Gyre. As a response, the positive sea surface height anomaly in the Canada Basin becomes weaker. During the vanishing stage, a negative sea surface height anomaly can already be seen in the eastern side of the Beaufort Gyre. The positive FWC anomaly which was in the central Arctic during the mature stage has been transported further south toward Fram Strait. The “tail” from the FWC positive anomaly center to the Beaufort Sea can still be seen, but in time, this bulk of Eurasian runoff leaves the control of the Beaufort Gyre. A negative dissolved Barium anomaly can be seen on the eastern side of the Beaufort Gyre, indicating the lack of river runoff.

During the vanishing stage (summer 2008), the atmospheric state is not suitable for the intensifica-

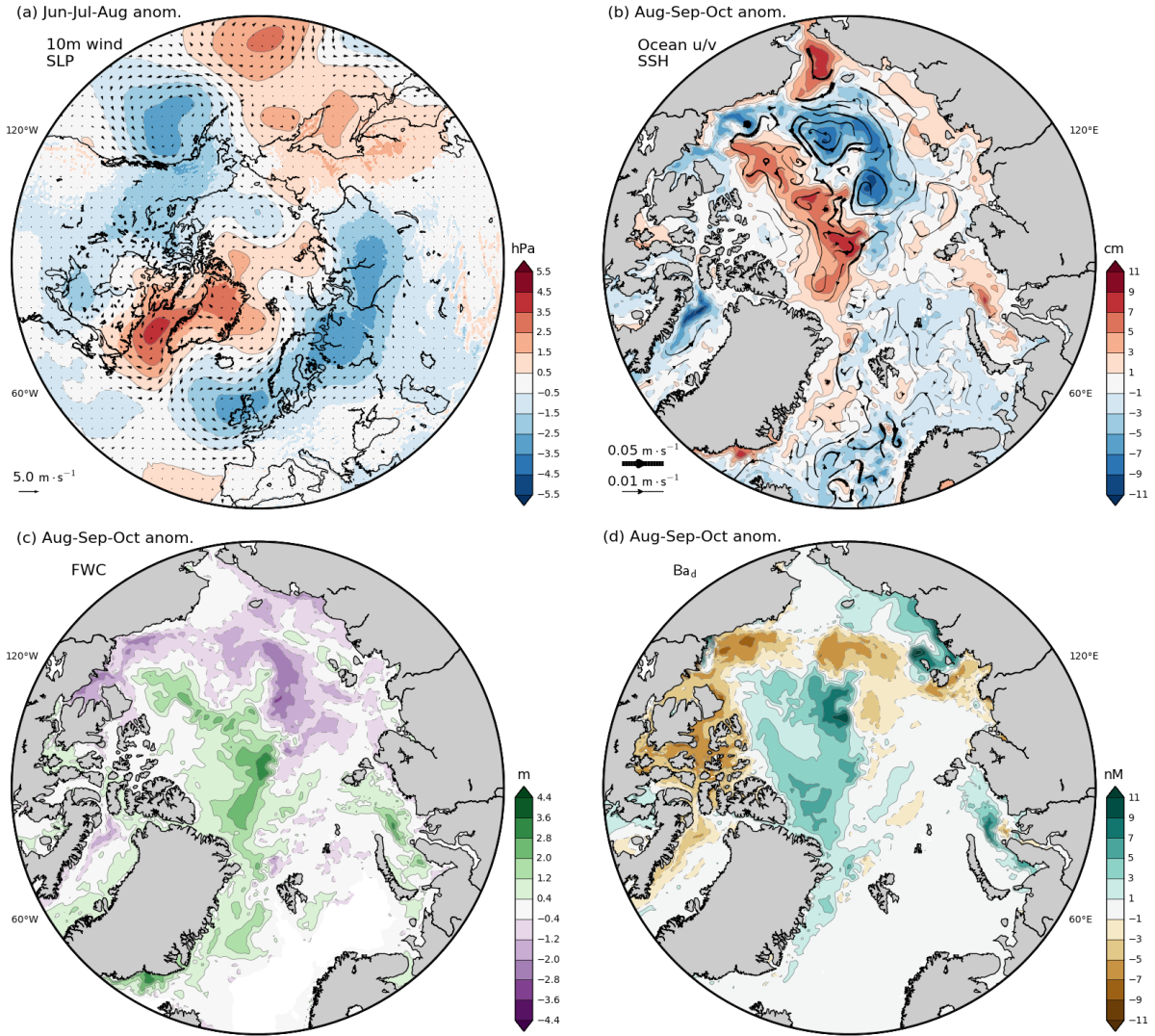


Figure 4.20: Same as figure 4.18, but for 2008 and no $E - P$ and $\delta^{18}\text{O}$ anomalies.

tion of the Beaufort Gyre, so the Beaufort Gyre spins-down and on longer able to hold a large amount of freshwater. The accumulated Eurasian runoff in the central Arctic is gradually transported further south away from the control of the surface circulation of the Beaufort Gyre.

The case study in this section considers both the Ekman transport and the Eurasian runoff, unlike previous studies that considered one or the other [Morison et al., 2012, Proshutinsky et al., 2009]. Previous research stressed the role of the AO [Morison et al., 2012] but in this study we have seen the role of the dipole anomaly on the transport of Eurasian runoff. The variability of Beaufort Gyre FWC is the net result of different atmospheric processes. For this case, the dipole anomaly and anticyclonic anomalous wind in the Canada Basin both play important roles.

4.5.2 Linear mixing model

As discussed above, the increase of Beaufort Gyre FWC in 2007-2008 is due to the increased transport of Eurasian runoff. Based on observations in 2007 and 2008, Alkire et al. [2010] found that Eurasian runoff and Pacific inflow both have a significant contribution to the meteoric water pool in the southern part of Canada Basin in the cold halocline. Also, Brown et al. [2014] found a predominance of Eurasian river source on the particulate organic Carbon in the Canada Basin. So it is no surprise to see Eurasian runoff in the Beaufort Gyre.

Considering that one of the simulated tracers in this research, dissolved Barium is able to separate North American runoff from Eurasian runoff [Guay and Falkner, 1997, 1998], a linear mixing model is applied to estimate the amount and temporal variations of Eurasian and North American runoff fractions. The theory and end-member choices of the linear mixing model was described in section 3.4.6.

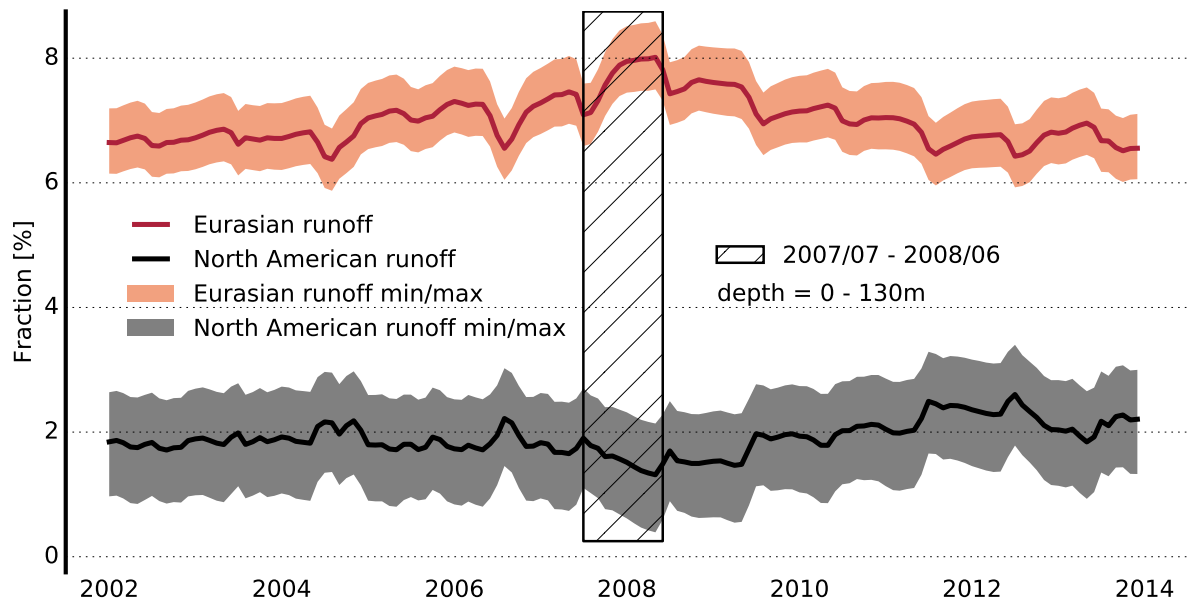


Figure 4.21: The timeseries of Eurasian (red) and North American (black) runoff fractions in the Beaufort Gyre (as defined in figure 3.7) from 0-130 m depth. The shade is the variation range. The time span of the case study is hatched.

According to the linear mixing model results, the North American runoff fraction varies 1% to 3% and reaches its peak in early summer, consistent with the seasonal cycle of riverine water input (figure 4.21). The Eurasian runoff fraction varies from 6% to 9%. It is higher than the North American runoff fraction, reflecting the high discharge of Eurasian rivers. The temporal variability of the Eurasian runoff fraction in Beaufort Sea is opposite the North American runoff and has a minimum each year in the late spring, early summer. The reason for the time lag can be explained by the time for transport of runoff water from the Eurasian marginal seas to the Beaufort Sea.

The range of possible values for the runoff fractions is about 1%. The lower bounds for both runoff fractions come from the lower salinity end-member; the range of sea-ice melt salinity end-member does not have a significant impact on the linear mixing model results. During the 2007-2008 period, espe-

cially during the mature stage of the 2007-2008 event, the Eurasian runoff fraction reaches its maximum which shows the increase of Eurasian runoff in the Beaufort Gyre, consistent with the conclusion for the case evolution study above. Also the fact that Beaufort Sea has a positive Eurasian runoff fraction supports the findings of Alkire et al. [2010].

Chapter 5

Discussion

5.1 Model configuration and operations

In this research, the tracer simulation was done offline using oceanographic variables from the ANHA4-EXH005 experiment. The choice to run offline is possible because dissolved Barium and Oxygen isotope ratio have no effect on the physical state of the ocean, or in other words, they are passive tracers and no tracer - physical ocean interaction needs to be modeled. Technically, since the ANHA4 experiments were run by another research team, the choice of offline simulation significantly reduced the required computational resources. The offline simulation means the tracers behave as a direct response to the ANHA4 forcing. Since the ANHA4 experiments have CGRF atmospheric forcing, the simulated tracer values were also indirectly affected by the CGRF atmosphere. Therefore, the overall simulation framework of this research is: CGRF atmosphere drives ANHA4 ocean, which drives the tracers. Both MY_TRC and ANHA4 need to be forced with river discharge. In this research, the choice of river discharge is consistent between the ANHA4 experiments and the tracer model. Thus there are no conflicts between the ANHA4 riverine freshwater input and MY_TRC tracer input.

5.2 Tracer parameterizations, model output and evaluations

5.2.1 dissolved Barium

The dissolved Barium scheme in this research defined twenty different estuaries since riverine dissolved Barium input only depends on the river borne clay types in the drainage basin which is a very localized feature. A coarse river estuary classification in a fine model grid may result in unrealistic tracer patterns. The classified regions also makes the model able to consider the spatial distribution of estuaries as an area source instead of point source. This is important for simulating rivers with big estuaries, using an area source makes sure that the estuarine tracer gradient will be consistent with the estuarine salinity gradient.

For the reconstructions of the seasonality of riverine dissolved Barium input, the biggest assumption is the “Normalized ensemble seasonal cycle” calculation which characterized the similarity of the sea-

sonal cycle normalized by the mean dissolved Barium concentration and provided reasonable estimates for dissolved Barium values in poorly observed Arctic rivers. A significant feature of the “Normalized ensemble seasonal cycle” calculation is the “drop down” signal which shows the effect of the spring freshet. This signal can also be seen in the observations of Cooper et al. [2008] for dissolved Barium and alkalinity. Thus, the appearance of this “drop down” signal during the late spring early summer, may also have the potential to be generalized in quantifying the river input of other hard-part nutrients.

Dissolved Barium in this research is modeled as conservative with external sources of river input and inflow from the open boundaries. Since the biological Barium cycling is not parameterized, the tracer model is not able to simulate the depletion of dissolved Barium at the surface due to the barite formation and the enrichment in the halocline and deep ocean due to the sinking and the remineralization (section 2.2). This creates bias in the model (section 4.2.1).

The lack of a Barium depletion signal was found in all comparisons with data above 60 m. The Beaufort Sea (BGEP), Chukchi Sea (CBL32PZ), the Nansen Basin and the Kara Sea (ARK-XXII/2) samples show an overestimate of about 4 – 6 nM; in the central Arctic (NPEO), the mode has an large overestimation of 10 nM. The large dissolved Barium overestimate at the 20-60 m depth in the Beaufort Sea and the Chukchi Sea is consistent with intensive biological activities at the the sub-surface Chlorophyll-a maximum Arrigo et al. [2011]. One can calculate the ratio between the Barium depletion and the conservative Barium model output to estimate the relative importance of the biological Barium uptake. The ratio calculated through the Nansen Basin and the Kara Sea (ARK-XXII/2) samples above 60 m is about 15%, in general consistent with the estimate in Roeske et al. [2012]. For the high overestimate in the central Arctic (10 nM mean bias) above 130 m, we should consider that: (1) the NPEO data was observed in April-May, which is not the peak of biological productivity in the Arctic ocean. (2) The sample locations are consistently covered by sea-ice and in the region that has the lowest biological productivity in the Arctic Arrigo et al. [2008]. (3) In the timeseries comparison (figure 4.4, b.2), the overestimate did not show up in 2004 and 2005, but biological modification should be happening every year. (4) The model does well for simulating Oxygen isotope ratio in the central Arctic (figure 4.5), which means the combined effect of sea-ice variability and runoff were properly modeled by the ANHA4 forcing. By considering all the factors, I think this overestimation is neither the effect of localized biological Barium uptake nor too much river runoff, but an advected biological signal, in other words, Eurasian runoff that has passed a productive region. The NPEO’s sample location is under the TDS, which is the major pathway of Eurasian runoff water. If the un-parameterized biological processes make the model overestimate the dissolved Barium on the Eurasian continental shelf, then this bias could be transported to the central Arctic. Due to lack of data, this assumption cannot be directly tested, but previous research indicates that the coastal Kara Sea and the Laptev Sea have strong sea-ice decline in the past decade [Parkinson and Cavalieri, 2008], which benefits the biological productivity [Arrigo et al., 2008], and evidence of Eurasian runoff was found in the halocline of the central Arctic [Alkire et al., 2010] and therefore able to affect the surface dissolved Barium concentration.

The underestimate due to the un-parameterized, biological induced dissolved Barium sinking was found in the Beaufort Sea and the Chukchi Sea in the 60-130 m depth. In the deep ocean (2-4 km)

all comparisons except the HLY0301 Baffin Bay samples show an underestimate of about 5 nM, in general balancing their overestimation at the surface and showing the role of remineralization. The strong underestimate in Baffin Bay (44 nM mean bias) can be explained by the long residence time of deep Baffin Bay water. The lack of ventilation in the deep Baffin Bay accumulates the remineralized Barium and the observed Barium concentration records can be higher than 100 nM.

5.2.2 Oxygen isotope ratio

The parameterization of the riverine Oxygen isotope ratio input uses seven different regions, since comparing with dissolved Barium, the Oxygen isotopes ratio in the Arctic rivers is more uniform. The six defined regions, by the names of their biggest rivers are Kolyma, Lena, Yenisey, Ob, Mckenzie and Yukon. Unique annual mean Oxygen isotope ratio values were applied for each region since observations show river-to-river differences, especially the Ob/Yenisey and Lena [Cooper et al., 2008].

The parameterization of fractionation during the sea-ice freeze-thaw cycle is end-member value based. The sea-ice melt water Oxygen isotope ratio is prescribed as 1.5‰ which is a good estimate for the central Arctic, close to the end-member choice in Östlund and Hut [1984] and Ekwurzel et al. [2001] and leads to good model-observation comparisons in the Amundsen Basin and over the Lomonosov Ridge. In the Canada Basin, 1.5‰ is probably too high when compared with previous research [Macdonald et al., 2002, Yamamoto-Kawai et al., 2008], and this potentially causes the overestimate of Oxygen isotope ratio in the Canada basin. We did not fix this bias since no comprehensive studies about the distribution of Oxygen-18 in the Arctic sea-ice can be found and hence there is no objective way to define the boundary between different sea-ice melt Oxygen isotope ratio end-member values.

5.3 Freshwater, tracers and atmospheric driving factors

The FWC was chosen as the object of the linear trend and EOF decomposition analysis, since the variability of FWC contains the change of all freshwater components and therefore can be explained by the two tracers. In addition, FWC variability reflects the change of near surface atmospheric circulations; directly impacts the stratification of the ocean, is a good representation of the Arctic atmosphere-ocean system and can be more readily compared to previous studies.

The linear trends and first three EOF modes for the FWC were extracted, different atmospheric factors were applied to explain the dynamics of FWC and the tracer patterns. The AO is the most important as the increase of winter-spring AO drives the linear trends of both FWC and tracers. The Dipole anomaly is the second most important factor, as it drives EOF mode one. The interannual signal of NAO is thought to play a role in EOF mode two and the localized anticyclonic anomalous wind in Canada Basin affects mode three. This sequence in general agrees with the EOF calculation of North Hemisphere sea level pressure by other research (e.g. [Thompson and Wallace, 1998], Wu et al. [2006]). The linear trend was removed before the EOF calculations since the Arctic Ocean in 2002-2013 is in a rapidly changing stage with the accelerated hydrological cycle [Carmack et al., 2016]. Removing linear trends a priori also makes all the EOF modes comparable. Indeed, if it is not removed, the linear mode will explain about 60% of the total variance and makes it difficult to separate other modes in the

remaining 40% of total variance. By the rule of thumb [North et al., 1982], in this research, all the three EOF modes were well separated.

5.4 Insights from the Beaufort Gyre case study

The Beaufort Gyre FWC study shows how the statistically based EOF modes and the tracer simulations can be used in a specific case. The rapid increase of the Beaufort Gyre FWC is a well studied topic and different explanations have been used to explain its change in the past decade. Our research shows that from 2007 to 2008 summer, the peak of the Beaufort Gyre FWC is a combined effect of the atmospheric dipole anomaly and an extraordinary strong Beaufort Gyre. The result of the linear mixing model indicates an increase of Eurasian runoff fraction, consistent with Morison et al. [2012]. However different from Morison et al. [2012], here the transport of Eurasian runoff is not due to the increase of the AO but due to the dipole anomaly. Two insights come from this case study: (1) The Eurasian runoff pathways can be modulated by different atmospheric factors, not just the AO. (2) Monitoring the change of Eurasian runoff contributes to the understanding of the disposition of Arctic FWC, and tracers like dissolved Barium and Oxygen isotope ratio can be the key to this effort.

5.5 Summary

An offline simulation with parameterized dissolved Barium and Oxygen isotope ratio was applied to the Arctic Ocean. The two simulated tracers show reasonable climatology and seasonal cycles, agree well with field observations and can be used as a tool for freshwater tracking. The tracer scheme is an example of parameterizing passive tracers by the balance between sources and sinks. The tracer model was applied to investigate the FWC variabilities and the atmospheric factors that drive them. The linear trend and EOF analysis of the physical variables and tracers show the role of the AO, the dipole anomaly, the NAO and the Beaufort Sea anticyclonic anomalous wind. In the case study of the Beaufort Gyre FWC in 2007-2008, the change of the Eurasian runoff pathways by dipole anomaly and the accumulation of Eurasian runoff in the Beaufort Gyre by a strong anticyclonic wind pattern was found. The case study explains the increase of FWC in the Beaufort Gyre from 2007 to 2008 and reveals the power of tracer simulation in the research of Arctic freshwater.

Chapter 6

Conclusions

6.1 Research questions

1. *How can dissolved Barium and Oxygen isotope ratio be simulated in a numeric model?*

Dissolved Barium and Oxygen isotope ratio were modeled as conservative with parameterized sources and sinks. The river input is the most important dissolved Barium source and was parameterized in twenty different regions with seasonal cycles. The estuarine tracer input locations are consistent with the estuarine freshwater input. The riverine input of Oxygen isotope ratio was modeled in a similar way as dissolved Barium but has fewer regions and uses annual mean input. The fractionation of the sea-ice freeze-thaw cycle was modeled for the Oxygen isotope ratio with an uniform end-member and the net sea-ice melt from the physical model. The inflow of the tracer into the Arctic was determined by the open boundary condition.

2. *What is the distribution and statistical features of the simulated tracers and how does the model output compare with field measurements?*

In the climatology, modeled dissolved Barium is high in the estuaries and on the North American side of the Arctic. The domain-wide mean dissolved Barium timeseries has an average of 59 nM and shows the seasonality of river input. The dissolved Barium fluxes through the Arctic Ocean and the flux of riverine input are well balanced. The total riverine Barium inputs of the simulation in the Mackenzie, Lena, Kolyma, Ob, Yenisey and Pechora Rivers are consistent with the estimates in Guay and Falkner [1998]. The model evaluation of dissolved Barium is in general good with overestimation above 60 m and underestimation along the halocline and at 2-4 km depth. The dissolved Barium model bias can be explained by the un-parameterized biological Barium cycling, including the barite formation at the surface, the sinking in the intermediate depth and the remineralization in the deep ocean.

The spatial variability of the modeled climatology of Oxygen isotope ratio is consistent with the distribution of sea surface salinity and is able to separate sea-ice melt water from meteoric water in a $\delta^{18}\text{O}$ -Salinity graph. The domain-wide averaged Oxygen isotope ratio timeseries and seasonal cycle show the mixed effect of meteoric water input and sea-ice melt and formation. In the semi-permanent

sea-ice covered region, the signal of parameterized sea-ice fractionation is stronger and helps confirm that it is properly modeled. The model evaluation of Oxygen isotope ratio is good with overestimation in the Beaufort Sea due to the choice of the sea-ice melt end-member.

3. How does atmospheric variability change the freshwater content in the Arctic ?

The simulated tracer anomalies can explain the FWC variability well by linking to their geochemical behaviors. When a positive dissolved Barium anomaly co-occurs with positive sea surface height and FWC anomalies, it indicates the increase of FWC is due to runoff. The two common regions that dissolved Barium anomalies can be found are the Beaufort Sea - CAA, which indicates the the shift of the pathway of high Barium concentration North American runoff and the Makarov Basin which shows the lose or gain of the East Siberian and Laptev Seas runoff.

The Oxygen isotope ratio anomalies have the information of net sea-ice melt and meteoric water combined. Since the Eurasian rivers together have higher discharge than the North American runoff, the Oxygen isotope ratio anomalies along the Eurasian coast and in the central Arctic usually means the change of Eurasian runoff. The positive Oxygen isotope ratio can also be linked to the increase of sea-ice melt, especially in the Laptev and Kara Seas which was reported to have significant summer sea-ice cover retreat [Parkinson and Cavalieri, 2008].

The linear mixing model is another way of using dissolved Barium and Oxygen isotope ratio to explain the FWC change. This approach was practiced in the case study in 2007-2008 to estimate the Eurasian and North American runoff fractions in the Beaufort Sea. The estimated temporal evolution of the runoff fractions, consistent well with the theory and the observational evidence, confirmed that, simulated dissolved Barium and Oxygen isotope ratio can be used to investigate freshwater end-members in the same manner that observations are used.

6.2 Contributions to the existing knowledge

6.2.1 The Canadian Arctic GEOTRACES Program

This research is the first numeric model simulation of dissolved Barium in the Arctic Ocean and an important part of the Canadian Arctic GEOTRACES Program. The comprehensive, four-dimensional tracer model with implemented geochemical processes, provides a good reference for climatology state of the tracers. The comparison between the model output with GEOTRACES field observations, improves the understanding of the conservative behavior of dissolved Barium and its usability as a tracer of Arctic river runoff; the Oxygen isotope ratio comparison result highlights the end-member difference between the Beaufort Sea side and the Eurasian side sea-ice melt water. All this information will be useful for further tracer model development.

6.2.2 Arctic Ocean freshwater studies

On the scope of Arctic Ocean freshwater science, in previous research, the dipole anomaly was thought to have an impact on the Arctic summer sea-ice cover [Wang et al., 2009]. In this research, the conclu-

sion from Wang et al. [2009] is confirmed with the simulated Oxygen isotope ratio composite anomaly result. However, we found the dipole anomaly also has a significant impact on the redistribution of other freshwater components, including Eurasian and North American runoff.

From summer 2007 to winter 2008, we found that the dipole anomaly, combined with a strong Beaufort Gyre, played an important role in transporting Eurasian runoff into the Beaufort Sea; this result provides new insight on the freshwater storage in the Beaufort Gyre after Morison et al. [2012] identified the role of the AO. On the methodology level, this research brings EOF and spectral analysis into the Arctic Ocean freshwater science, extending data interpretation.

6.3 Future research

Many improvements could be made to provide better tracer simulation results. In the model evaluation, the un-parameterized biological Barium cycling is thought to generate systematic errors in the model results. This problem can be solved by adding the surface barite formation, the sinking of barite with organic particles and the remineralization in the sediments to the tracer scheme. The observation of other biological tracers can help divide the model domain into different categories by the importance of biological induced Barium cycling. The difference between the “modeled as conservative” and “biologically modified” dissolved Barium also provides an estimate of surface Barium depletion. For the Oxygen isotope ratio, more field observations at the edge of Beaufort Sea in summer can help adjusting the parameterization of sea-ice melt fractionation. By incorporating more field observations in the small and poorly observed Arctic rivers in the future, especially in the Eurasian side of the Arctic, the model would have a better estimate of the riverine tracer input. The configuration of the open boundaries in the Bering Strait, the Fram Strait, the Davis Strait and the Barents Sea openings depend on the field observations. If more observations are available in these Arctic Ocean inflow and outflow channels, the model will have a better estimate of the open boundary conditions.

For using simulated freshwater tracers to investigate the variability of the Arctic freshwater, sensitive experiments may provide new insights about how the atmospheric circulations can change the surface Arctic FWC and how the effect of circulation can be tested by the freshwater tracer field observations. Interesting sensitivity experiments include the atmospheric forcing of AO, dipole anomaly and NAO since all these anomaly patterns have different impacts on the Arctic Ocean freshwater. Longer simulations can be prepared to investigate the long-term variabilities of the Arctic freshwater and tracers in the past. In this research, the linear mixing model applied for the simulated tracers cannot separate Pacific water from North Atlantic water and therefore uncertainties remain; in future studies, this problem could be solved by adding tracers for Pacific inflow (e.g. nitrate and phosphate).

Based on the trend of a positive temperature in polar regions, it is believed that the Arctic Ocean will become ice-free in the middle-21st century with a rapid increase of its surface freshwater [Hu and Myers, 2014, Wang and Overland, 2009]. Climate models in the IPCC-AR5 suggest intensified AO and NAO with anthropogenic forcing [IPCC, 2013]. These two teleconnection patterns may play an important role in redistributing surface freshwater in the future. Based on the result in 4.3 and 4.4, AO leads to an increased transport of surface freshwater from the Eurasian side of the Arctic to the Beaufort

Sea, meanwhile the asymmetric NAO leads to an accumulation of freshwater in the Makarov Basin. The interplay of these two patterns will preserve and increase the FWC or salinity gradient between the North American side and the Eurasian side of the Arctic. The response of different freshwater components depends highly on the interactions and down-stream effects which require more on-going research. The tracer model in this research provides an opportunity for projection of the future state. By applying different climate change scenarios, the possible change of the Arctic Ocean freshwater and its tracers in the future can be identified.

Bibliography

- K. Aagaard and E. C. Carmack. The role of sea ice and other fresh water in the Arctic circulation. *J. Geophys. Res.: Oceans (1978–2012)*, 94(C10):14485–14498, 1989. → pages 1, 4, 5, 6
- K. Aagaard and E. C. Carmack. The Arctic Ocean and climate: A perspective. In O. M. Johannessen, R. D. Muench, and J. E. Overland, editors, *The polar oceans and their role in shaping the global environment*, volume 85 of *AGU Geophysics Monograph*, pages 5–20. American Geophysical Union, Washington, D.C., 1994. → pages 1, 6
- K. Aagaard, L. K. Coachman, and E. C. Carmack. On the halocline of the Arctic Ocean. *Deep Sea Res. Part A. Oceanographic Research Papers*, 28(6):529–545, 1981. → pages 1
- K. Aagaard, J. H. Swift, and E. C. Carmack. Thermohaline circulation in the Arctic Mediterranean Seas. *J. Geophys. Res.: Oceans (1978–2012)*, 90(C3):4833–4846, 1985. → pages 1, 3, 5
- E. P. Abrahamsen, M. P. Meredith, K. K. Falkner, S. Torres-Valdes, M. J. Leng, M. B. Alkire, S. Bacon, S. W. Laxon, I. Polyakov, and V. Ivanov. Tracer-derived freshwater composition of the Siberian Continental Shelf and slope following the extreme Arctic summer of 2007. *Geophys. Res. Lett.*, 36(7), 2009. → pages 7
- AGRO. PARTNERS, Arctic-GRO I, Arctic-GRO II constituent data, Arctic Great Rivers Observatory (NSF-1107774). Accessed 2016/04/08. <http://www.arcticgreatrivers.org/data.html>, 2016. → pages 18
- M. Alkire. Small Canadian Arctic River Flows, 2014, NSF Arctic Data Center. Accessed 2015/07/13. <https://arcticdata.io/catalog/#view/doi:10.18739/A2CP8H>, 2015. → pages 18
- M. B. Alkire, K. K. Falkner, J. Morison, R. W. Collier, C. K. Guay, R. A. Desiderio, I. G. Rigor, and M. McPhee. Sensor-based profiles of the NO parameter in the central Arctic and southern Canada Basin: New insights regarding the cold halocline. *Deep Sea Res. Part I: Oceanographic Research Papers*, 57(11):1432–1443, 2010. → pages 50, 51, 53
- K. R. Arrigo, G. van Dijken, and S. Pabi. Impact of a shrinking Arctic ice cover on marine primary production. *Geophys. Res. Lett.*, 35(19), 2008. → pages 7, 53
- K. R. Arrigo, P. A. Matrai, and G. L. Van Dijken. Primary productivity in the Arctic Ocean: Impacts of complex optical properties and subsurface Chlorophyll maxima on large-scale estimates. *J. Geophys. Res.: Oceans*, 116(C11), 2011. → pages 53
- M. P. Bacon and J. M. Edmond. Barium at GEOSECS III in the southwest Pacific. *Earth Planet. Sc. Lett.*, 16(1):66–74, 1972. → pages 6

- J. Bamber, M. den Broeke, J. Ettema, J. Lenaerts, and E. Rignot. Recent large increases in freshwater fluxes from Greenland into the North Atlantic. *Geophys. Res. Lett.*, 39(19), 2012. → pages 17
- L. Bengtsson, K. I. Hodges, S. Koumoutsaris, M. Zahn, and N. Keenlyside. The changing atmospheric water cycle in polar regions in a warmer climate. *Tellus A*, 63(5):907–920, 2011. → pages 3
- R. E. Bernstein, R. H. Byrne, P. R. Betzer, and A. M. Greco. Morphologies and transformations of celestite in seawater: The role of acantharians in Strontium and Barium geochemistry. *Geochim. Cosmochim. Ac.*, 56(8):3273–3279, 1992. → pages 6
- R. E. Bernstein, R. H. Byrne, and J. Schijf. Acantharians: a missing link in the oceanic biogeochemistry of Barium. *Deep Sea Res. Part I: Oceanographic Research Papers*, 45(2):491–505, 1998. → pages 6
- R. Bintanja and F. Selten. Future increases in Arctic precipitation linked to local evaporation and sea-ice retreat. *Nature*, 509(7501):479–482, 2014. → pages 3
- J. K. Bishop. The barite-opal-organic carbon association in oceanic particulate matter. *Nature*, 332(6162):341–343, 1988. → pages 6
- C. S. Bretherton, M. Widmann, V. P. Dymnikov, J. M. Wallace, and I. Bladé. The effective number of spatial degrees of freedom of a time-varying field. *J. Climate*, 12(7):1990–2009, 1999. → pages 21, 76
- K. A. Brown, F. McLaughlin, P. D. Tortell, D. E. Varela, M. Yamamoto-Kawai, B. Hunt, and R. Francois. Determination of particulate organic Carbon sources to the surface mixed layer of the Canada Basin, Arctic Ocean. *J. Geophys. Res.: Oceans*, 119(2):1084–1102, 2014. → pages 50
- W. J. Campbell. The wind-driven circulation of ice and water in a polar ocean. *J. Geophys. Res.*, 70(14):3279–3301, 1965. → pages 9
- E. Carmack, F. McLaughlin, M. Yamamoto-Kawai, M. Itoh, K. Shimada, R. Krishfield, and A. Proshutinsky. Freshwater storage in the Northern Ocean and the special role of the Beaufort Gyre. In R. R. Dickson, J. Meincke, and P. Rhines, editors, *Arctic Subarctic ocean fluxes*, pages 145–169. Springer, Dordrecht, 2008. → pages 5
- E. C. Carmack, M. Yamamoto-Kawai, T. W. Haine, S. Bacon, B. Bluhm, C. Lique, H. Melling, I. V. Polyakov, F. Straneo, M.-L. Timmermans, et al. Freshwater and its role in the Arctic Marine System: Sources, disposition, storage, export, and physical and biogeochemical consequences in the Arctic and global oceans. *J. Geophys. Res.: Biogeosciences*, 121(3):675–717, 2016. → pages 1, 54
- L. H. Chan, D. Drummond, J. M. Edmond, and B. Grant. On the Barium data from the Atlantic GEOSECS expedition. *Deep Sea Res.*, 24(7):613–649, 1977. → pages 6
- J. C. Comiso, C. L. Parkinson, R. Gersten, and L. Stock. Accelerated decline in the Arctic sea ice cover. *Geophys. Res. Lett.*, 35(1), 2008. → pages 7
- A. Condron, P. Winsor, C. Hill, and D. Menemenlis. Simulated response of the Arctic freshwater budget to extreme NAO wind forcing. *J. Climate*, 22(9):2422–2437, 2009. → pages 45
- L. W. Cooper, J. W. McClelland, R. M. Holmes, P. A. Raymond, J. Gibson, C. K. Guay, and B. J. Peterson. Flow-weighted values of runoff tracers ($\delta^{18}\text{O}$, DOC, Ba, alkalinity) from the six largest Arctic rivers. *Geophys. Res. Lett.*, 35(18), 2008. → pages 14, 53, 54

- CPC-NOAA. Teleconnections, AAO, NAO, PNA & AO. Accessed 2015/05/16.
http://www.cpc.ncep.noaa.gov/products/precip/CWlink/daily_ao_index/teleconnections.shtml, 2016.
 → pages 21
- H. Craig and L. I. Gordon. Deuterium and Oxygen 18 variations in the ocean and marine atmosphere. In E. Tongiogi, editor, *Stable Isotopes in Oceanographic Studies and Paleotemperatures*, pages 80–83. Lab. Geol. and Nuclear Sci., Pisa, Italy, 1965. → pages 8
- J. A. Curry, J. L. Schramm, and E. E. Ebert. Sea ice-albedo climate feedback mechanism. *J. Climate*, 8(2):240–247, 1995. → pages 4
- A. Dai and K. E. Trenberth. Estimates of freshwater discharge from continents: Latitudinal and seasonal variations. *J. Hydrometeorol.*, 3(6):660–687, 2002. → pages 3
- A. Dai, T. Qian, K. E. Trenberth, and J. D. Milliman. Changes in continental freshwater discharge from 1948 to 2004. *J. Climate*, 22(10):2773–2792, 2009. → pages 17
- W. Dansgaard. Stable isotopes in precipitation. *Tellus*, 16(4):436–468, 1964. → pages 7
- C. Deser, J. E. Walsh, and M. S. Timlin. Arctic sea ice variability in the context of recent atmospheric circulation trends. *J. Climate*, 13(3):617–633, 2000. → pages 4
- R. R. Dickson, J. Meincke, S.-A. Malmberg, and A. J. Lee. The “great salinity anomaly” in the northern North Atlantic 1968–1982. *Prog. Oceanogr.*, 20(2):103–151, 1988. → pages 1, 6
- T. Dittmar and G. Kattner. The biogeochemistry of the river and shelf ecosystem of the Arctic Ocean: a review. *Mar. Chem.*, 83(3):103–120, 2003. → pages 6
- J. Dymond, E. Suess, and M. Lyle. Barium in deep-sea sediment: A geochemical proxy for paleoproductivity. *Paleoceanography*, 7(2):163–181, 1992. → pages 6
- EC-Wateroffice. Daily Discharge Data for Mackenzie River (East Channel) at INUVIK (10LC002), Wateroffice, Environment Canada. Accessed 2015/04/12.
http://wateroffice.ec.gc.ca/report/report_e.html?mode=Table&type=h2oArc&stn=10LC002&dataType=Daily¶meterType=Flow&year=2015&y1Max=1&y1Min=1, 2016. → pages 13
- J. M. Edmond, E. D. Boyle, D. Drummond, B. Grant, and T. Mislick. Desorption of Barium in the plume of the Zaire (Congo) River. *Neth. J. Sea Res.*, 12(3):324–328, 1978. → pages 7
- B. Ekwurzel, P. Schlosser, R. A. Mortlock, R. G. Fairbanks, and J. H. Swift. River runoff, sea ice meltwater, and Pacific water distribution and mean residence times in the Arctic Ocean. *J. Geophys. Res.: Oceans (1978–2012)*, 106(C5):9075–9092, 2001. → pages 1, 9, 54
- B. K. Esser and A. M. Volpe. At-sea high-resolution chemical mapping: extreme Barium depletion in North Pacific surface water. *Marine chemistry*, 79(2):67–79, 2002. → pages 6
- K. Falkner. Hydrographic cruise 32H120030721, 2003, Clivar & Carbon Hydrographic Data Office (CCHDO). Accessed 2015/07/03. <https://cchdo.ucsd.edu/cruise/32H120030721>, 2014. → pages 18
- K. K. Falkner. Arctic Ocean Barium Concentrations, 1993, version 1.0. UCAR/NCAR - Earth Observing Laboratory. Accessed 2015/07/09. <http://doi.org/10.5065/D64T6GGS>, 2009a. → pages 18

- K. K. Falkner. Hydrographic parameters from Fram Strait and Denmark Strait, 1998, version 1.0. UCAR/NCAR - Earth Observing Laboratory. Accessed 2015/07/08. <https://data.eol.ucar.edu/dataset/106.ARCSS105>, 2009b. → pages 18
- K. K. Falkner. Barium Concentrations and Salinity in Arctic River Estuaries, 1993-1996, version 1.0. UCAR/NCAR - Earth Observing Laboratory. Accessed 2015/07/13. <http://doi.org/10.5065/D6XP7320>, 2009c. → pages 18
- K. K. Falkner, T. Bowers, J. Todd, B. Lewis, W. Landing, J. Edmond, et al. The behavior of Barium in anoxic marine waters. *Geochim. Cosmochim. Acta*, 57(3):537–554, 1993. → pages 6, 7
- K. K. Falkner, R. W. MacDonald, E. C. Carmack, and T. Weingartner. The potential of Barium as a tracer of Arctic water masses. In O. M. Johannessen, R. D. Muench, and J. E. Overland, editors, *The polar oceans and their role in shaping the global environment*, volume 85 of *AGU Geophysics Monograph*, pages 63–76. American Geophysical Union, Washington, D.C., 1994. → pages 1, 6, 7
- M.-A. Foujols, M. Lévy, O. Aumont, and G. Madec. OPA 8.1 tracer model reference manual. Technical report, Institut Pierre Simon Laplace (IPSL), des Sciences de l'Environnement Global, Paris, France, 2000. → pages 11
- J. Galt. A numerical investigation of Arctic Ocean dynamics. *J. Phys. Oceanogr.*, 3(4):379–396, 1973. → pages 9
- D. L. Gilman, F. J. Fuglister, and J. M. Mitchell Jr. On the power spectrum of “red noise”. *J. Atmos. Sci.*, 20(2):182–184, 1963. → pages 77
- C. K. Guay. Barium as a tracer of Arctic halocline and river waters. Master’s thesis, Oregon State University, Corvallis, Oregon, 2 1997. → pages 7
- C. K. Guay and K. K. Falkner. Barium as a tracer of Arctic halocline and river waters. *Deep Sea Res. Part II: Topical Studies in Oceanography*, 44(8):1543–1569, 1997. → pages 7, 50
- C. K. Guay and K. K. Falkner. A survey of dissolved Barium in the estuaries of major Arctic rivers and adjacent seas. *Cont. Shelf Res.*, 18(8):859–882, 1998. → pages vii, 7, 27, 50, 56
- T. W. Haine, B. Curry, R. Gerdes, E. Hansen, M. Karcher, C. Lee, B. Rudels, G. Spreen, L. de Steur, K. D. Stewart, et al. Arctic freshwater export: Status, mechanisms, and prospects. *Global Planet. Change*, 125:13–35, 2015. → pages 5, 6
- S. Häkkinen. An Arctic source for the great salinity anomaly: A simulation of the Arctic ice-ocean system for 1955–1975. *J. Geophys. Res.: Oceans*, 98(C9):16397–16410, 1993. → pages 9
- A. M. Holdsworth and P. G. Myers. The influence of high-frequency atmospheric forcing on the circulation and deep convection of the Labrador Sea. *J. Climate*, 28(12):4980–4996, 2015. → pages 11, 17
- M. M. Holland, C. M. Bitz, M. Eby, and A. J. Weaver. The role of ice-ocean interactions in the variability of the North Atlantic thermohaline circulation. *J. Climate*, 14(5):656–675, 2001. → pages 1, 6
- M. M. Holland, J. Finnis, and M. C. Serreze. Simulated Arctic Ocean freshwater budgets in the twentieth and twenty-first centuries. *J. Climate*, 19(23):6221–6242, 2006. → pages 1, 9

- W. Hsieh. *Machine learning methods in the environmental sciences: Neural networks and kernels*. Cambridge University Press, 2009. → pages 72
- X. Hu and P. G. Myers. Changes to the Canadian Arctic Archipelago sea ice and freshwater fluxes in the twenty-first century under the Intergovernmental Panel on Climate Change A1B climate scenario. *Atmos.-Ocean*, 52(4):331–350, 2014. doi: 10.1080/07055900.2014.942592. → pages 58
- J. W. Hurrell. Decadal trends in the North Atlantic Oscillation. *Science*, 269:676, 1995. → pages 39, 80
- IPCC. *Climate Change 2013: The Physical Science Basis. Contribution of Working Group I to the Fifth Assessment Report of the Intergovernmental Panel on Climate Change*. Cambridge University Press, Cambridge, United Kingdom and New York, NY, USA, 2013. ISBN ISBN 978-1-107-66182-0. doi: 10.1017/CBO9781107415324. URL www.climatechange2013.org. → pages 58
- J. M. Jackson, S. E. Allen, F. A. McLaughlin, R. A. Woodgate, and E. C. Carmack. Changes to the near-surface waters in the Canada Basin, Arctic Ocean from 1993–2009: A basin in transition. *J. Geophys. Res.: Oceans*, 116(C10), 2011. → pages 5, 45
- A. Jahn, L. B. Tremblay, R. Newton, M. M. Holland, L. A. Mysak, and I. A. Dmitrenko. A tracer study of the Arctic Ocean’s liquid freshwater export variability. *J. Geophys. Res.: Oceans*, 115(C7), 2010. → pages 1, 5, 9, 23
- J. H. Jungclaus, H. Haak, M. Latif, and U. Mikolajewicz. Arctic-North Atlantic interactions and multidecadal variability of the meridional overturning circulation. *J. Climate*, 18(19):4013–4031, 2005. → pages 9
- M. B. Klunder, D. Bauch, P. Laan, H. J. W. d. Baar, S. v. Heuven, and S. Ober. Dissolved iron in the Arctic shelf seas and surface waters of the central Arctic Ocean: Impact of Arctic river water and ice-melt. *J. Geophys. Res.: Oceans*, 117(C1), 2012. → pages 6
- R. B. Lammers, A. I. Shiklomanov, C. J. Vörösmarty, B. M. Fekete, and B. J. Peterson. Assessment of contemporary Arctic river runoff based on observational discharge records. *J. Geophys. Res.: Atmospheres (1984–2012)*, 106(D4):3321–3334, 2001. → pages 5, 12
- F. W. Landerer, J. O. Dickey, and A. Güntner. Terrestrial water budget of the Eurasian pan-Arctic from GRACE satellite measurements during 2003–2009. *J. Geophys. Res.: Atmospheres*, 115(D23), 2010. → pages 3
- W. G. Large and S. G. Yeager. Diurnal to decadal global forcing for ocean and sea-ice models: the data sets and flux climatologies. Technical Report NCAR/TN-4601STR, NCAR, Boulder, Colorado, 2004. → pages 17
- A. N. LeGrande and G. A. Schmidt. Global gridded data set of the Oxygen isotopic composition in seawater. *Geophys. Res. Lett.*, 33(12), 2006. → pages 16
- Y. H. Li and L. H. Chan. Desorption of Ba and ²²⁶Ra from river-borne sediments in the Hudson estuary. *Earth Planet. Sc. Lett.*, 43(3):343–350, 1979. → pages 7
- S. Libes. *Introduction to marine biogeochemistry*. Academic Press, Elsevier Inc., 2011. → pages 6
- E. N. Lorenz. Empirical orthogonal functions and statistical weather prediction. Technical Report 1, Massachusetts Institute of Technology, Cambridge, Massachusetts, 12 1956. → pages 21, 74

- R. W. Macdonald, F. A. McLaughlin, and E. C. Carmack. Fresh water and its sources during the SHEBA drift in the Canada Basin of the Arctic Ocean. *Deep Sea Res. Part I: Oceanographic Research Papers*, 49(10):1769–1785, 2002. → pages 9, 54
- G. Madec and the NEMO team. NEMO ocean engine. Technical Report ISSN No 1288-1619, Institut Pierre Simon Laplace (IPSL), des Sciences de l’Environnement Global, Paris, France, 2012. → pages 10
- M. Majoube. Fractionnement en Oxygene-18 et en deuterium entre l’eau et sa vapeur (in french). *J. Chim. phys*, 68(7-8):1423–1436, 1971. → pages 8
- M. Manizza, M. J. Follows, S. Dutkiewicz, J. W. McClelland, D. Menemenlis, C. Hill, A. Townsend-Small, and B. J. Peterson. Modeling transport and fate of riverine dissolved organic Carbon in the Arctic Ocean. *Global Biogeochem. Cy.*, 23(4), 2009. → pages 1, 9
- G. A. Maykut and N. Untersteiner. Some results from a time-dependent thermodynamic model of sea ice. *J. Geophys. Res.*, 76(6):1550–1575, 1971. → pages 9
- M. G. McPhee, T. P. Stanton, J. H. Morison, and D. G. Martinson. Freshening of the upper ocean in the Arctic: Is perennial sea ice disappearing? *Geophys. Res. Lett.*, 25(10):1729–1732, 1998. → pages 45
- M. G. McPhee, A. Proshutinsky, J. H. Morison, M. Steele, and M. B. Alkire. Rapid change in freshwater content of the Arctic Ocean. *Geophys. Res. Lett.*, 36(10), 2009. → pages 1, 45
- G. L. Mellor and T. Yamada. Development of a turbulence closure model for geophysical fluid problems. *Rev. Geophys.*, 20(4):851–875, 1982. → pages 16
- J. R. Miller and G. L. Russell. Projected impact of climate change on the freshwater and salt budgets of the Arctic Ocean by a global climate model. *Geophys. Res. Lett.*, 27(8):1183–1186, 2000. → pages 9
- S.-K. Min, X. Zhang, and F. Zwiers. Human-induced Arctic moistening. *Science*, 320(5875):518–520, 2008. → pages 3
- J. Morison, R. Kwok, C. Peralta-Ferriz, M. Alkire, I. Rigor, R. Andersen, and M. Steele. Changing Arctic Ocean freshwater pathways. *Nature*, 481(7379):66–70, 2012. → pages 5, 32, 45, 49, 55, 58
- H. Mosby. Water, salt and heat balance of the North Polar Sea and of the Norwegian Sea. *Geophys. Norv*, 24(11):289–313, 1962. → pages 5
- P. G. Myers. Impact of freshwater from the Canadian Arctic archipelago on Labrador Sea water formation. *Geophys. Res. Lett.*, 32(6), 2005. → pages 9
- L. Mysak, K. Wright, J. Sedláček, M. Eby, and E. S. M. Group. Simulation of sea ice and ocean variability in the Arctic during 1955–2002 with an intermediate complexity model. *Atmos.-Ocean*, 43(1):101–118, 2005. → pages 9
- G. R. North, T. L. Bell, R. F. Cahalan, and F. J. Moeng. Sampling errors in the estimation of empirical orthogonal functions. *Mon. Weather Rev.*, 110(7):699–706, 1982. → pages 21, 34, 38, 42, 55, 76
- NPEO. North Pole Environmental Observatory, 2000-2015. Accessed 2015/07/08. <http://psc.apl.washington.edu/northpole/Data.html>, 2015. → pages 18
- H. G. Östlund and G. Hut. Arctic Ocean water mass balance from isotope data. *J. Geophys. Res.: Oceans (1978–2012)*, 89(C4):6373–6381, 1984. → pages 9, 54

- C. L. Parkinson and D. J. Cavalieri. Arctic sea ice 1973–1987: Seasonal, regional, and interannual variability. *J. Geophys. Res.: Oceans*, 94(C10):14499–14523, 1989. → pages 4
- C. L. Parkinson and D. J. Cavalieri. Arctic sea ice variability and trends, 1979–2006. *J. Geophys. Res.: Oceans*, 113(C7), 2008. → pages 53, 57
- I. V. Polyakov, A. V. Pnyushkov, R. Rember, L. Padman, E. C. Carmack, and J. M. Jackson. Winter convection transports Atlantic water heat to the surface layer in the Eastern Arctic Ocean. *J. Phys. Oceanogr.*, 43(10):2142–2155, 2013. → pages 1, 6
- A. Proshutinsky and R. Krishfield. Beaufort Gyre Exploration Project, 2003-2005, Woods Hole Oceanographic Institution (WHOI) in collaboration with Fisheries and Oceans Canada at the Institute of Ocean Sciences. Accessed 2015/06/09.
<http://www.whoi.edu/website/beaufortgyre/expeditions>, 2016. → pages 18
- A. Proshutinsky, R. Bourke, and F. McLaughlin. The role of the Beaufort Gyre in Arctic climate variability: Seasonal to decadal climate scales. *Geophys. Res. Lett.*, 29(23):15–1, 2002. → pages 3, 9, 44, 45
- A. Proshutinsky, R. Krishfield, M.-L. Timmermans, J. Toole, E. Carmack, F. McLaughlin, W. J. Williams, S. Zimmermann, M. Itoh, and K. Shimada. Beaufort Gyre freshwater reservoir: State and variability from observations. *J. Geophys. Res.: Oceans (1978–2012)*, 114(C1), 2009. → pages 1, 3, 44, 49
- A. Proshutinsky, Y. Aksenov, J. C. Kinney, R. Gerdes, E. Golubeva, D. Holland, G. Holloway, A. Jahn, M. Johnson, E. E. Popova, et al. Recent advances in Arctic ocean studies employing models from the Arctic Ocean Model Intercomparison Project. *Oceanography*, 2011. → pages 45
- B. Rabe, M. Karcher, U. Schauer, J. M. Toole, R. A. Krishfield, S. Pisarev, F. Kauker, R. Gerdes, and T. Kikuchi. An assessment of Arctic Ocean freshwater content changes from the 1990s to the 2006–2008 period. *Deep Sea Res. Part I: Oceanographic Research Papers*, 58(2):173–185, 2011. → pages 1, 5, 45
- I. G. Rigor and J. M. Wallace. Variations in the age of Arctic sea-ice and summer sea-ice extent. *Geophys. Res. Lett.*, 31(9), 2004. → pages 4
- I. G. Rigor, J. M. Wallace, and R. L. Colony. Response of sea ice to the Arctic Oscillation. *J. Climate*, 15(18):2648–2663, 2002. → pages 33
- T. Roeske, D. Bauch, M. R. V. Loeff, and B. Rabe. Utility of dissolved Barium in distinguishing North American from Eurasian runoff in the Arctic Ocean. *Mar. Chem.*, 132:1–14, 2012. → pages 7, 18, 53
- E. J. Rohling. Oxygen isotope composition of seawater. In S. A. Elias, editor, *The encyclopedia of quaternary science*, volume 2, pages 915–922. Elsevier, Amsterdam, 2013. → pages 7, 8
- P. Schlosser, R. Newton, B. Ekwurzel, S. Khatiwala, R. Mortlock, and R. Fairbanks. Decrease of river runoff in the upper waters of the Eurasian Basin, Arctic Ocean, between 1991 and 1996: evidence from $\delta^{18}\text{O}$ data. *Geophys. Res. Lett.*, 29(9), 2002. → pages 1, 5
- R. W. Schmitt, P. S. Bogden, and C. E. Dorman. Evaporation minus precipitation and density fluxes for the North Atlantic. *J. Phys. Oceanogr.*, 19(9):1208–1221, 1989. → pages 15

- A. J. Semtner Jr. Numerical simulation of the Arctic Ocean circulation. *J. Phys. Oceanogr.*, 6(4): 409–425, 1976. → pages 9
- M. C. Serreze, A. P. Barrett, A. G. Slater, R. A. Woodgate, K. Aagaard, R. B. Lammers, M. Steele, R. Moritz, M. Meredith, and C. M. Lee. The large-scale freshwater cycle of the Arctic. *J. Geophys. Res.: Oceans (1978–2012)*, 111(C11), 2006. → pages 5, 6
- M. C. Serreze, M. M. Holland, and J. Stroeve. Perspectives on the Arctic’s shrinking sea-ice cover. *Science*, 315(5818):1533–1536, 2007. → pages 5
- G. C. Smith, F. Roy, P. Mann, F. Dupont, B. Brasnett, J.-F. Lemieux, S. Laroche, and S. Bélair. A new atmospheric dataset for forcing ice–ocean models: Evaluation of reforecasts using the Canadian global deterministic prediction system. *Q. J. Roy. Meteor. Soc.*, 140(680):881–894, 2014. → pages 17
- M. Steele and T. Boyd. Retreat of the cold halocline layer in the Arctic Ocean. *J. Geophys. Res.: Oceans*, 103(C5):10419–10435, 1998. → pages 5
- M. Steele, D. Thomas, D. Rothrock, and S. Martin. A simple model study of the Arctic Ocean freshwater balance, 1979–1985. *J. Geophys. Res.: Oceans*, 101(C9):20833–20848, 1996. → pages 9
- P. Stoica and R. L. Moses. *Introduction to spectral analysis*, volume 1. Prentice hall Upper Saddle River, 1997. → pages 77
- J. R. Taylor, K. K. Falkner, U. Schauer, and M. Meredith. Quantitative considerations of dissolved Barium as a tracer in the Arctic Ocean. *J. Geophys. Res.: Oceans (1978–2012)*, 108(C12), 2003. → pages 7, 23
- D. W. Thompson and J. M. Wallace. The Arctic Oscillation signature in the wintertime geopotential height and temperature fields. *Geophys. Res. Lett.*, 25(9):1297–1300, 1998. → pages 54, 80
- J.-É. Tremblay and J. Gagnon. The effects of irradiance and nutrient supply on the productivity of Arctic waters: a perspective on climate change. In *Influence of climate change on the changing Arctic and sub-Arctic conditions*, C, pages 73–93. Springer, Dordrecht, 2009. → pages 1, 6
- UNESCO, ICES, SCOR, and IAPSO. Background papers and supporting data on the practical salinity scale 1978. Technical Report 37, UNESCO, Paris, France, 1981. → pages 5
- USGS. Yukon River at Pilot station (15565447), Anchorage Field Office, USGS, in cooperation with National Streamflow Information Program. Accessed 2015/04/12. http://waterdata.usgs.gov/usa/nwis/uv?site_no=15565447, 2016. → pages 13
- M. M. R. Van Der Loeff, R. M. Key, J. Scholten, D. Bauch, and A. Michel. ²²⁸Ra as a tracer for shelf water in the Arctic Ocean. *Deep Sea Res. Part II: Topical Studies in Oceanography*, 42(6): 1533–1553, 1995. → pages 5
- M. Vancoppenolle, S. Bouillon, T. Fichefet, H. Goosse, O. Lecomte, M. Angel, M. Maqueda, and G. Madec. LIM: The Louvain-la-Neuve sea ice model. Technical Report ISSN No 1288-1619, Institut Pierre Simon Laplace (IPSL), des Sciences de l’Environnement Global, Paris, France, 2012. → pages 16
- K. L. Von Damm, J. M. Edmond, B. Grant, C. I. Measures, B. Walden, and R. F. Weiss. Chemistry of submarine hydrothermal solutions at 21°N, East Pacific rise. *Geochim. Cosmochim. Acta*, 49(11): 2197–2220, 1985. → pages 7, 11

- C. Vörösmarty, B. Fekete, M. Meybeck, and R. Lammers. Global system of rivers: Its role in organizing continental land mass and defining land-to-ocean linkages. *Global Biogeochem. Cy.*, 14(2):599–621, 2000. → pages 3
- J. E. Walsh, V. Kattsov, D. Portis, and V. Meleshko. Arctic precipitation and evaporation: Model results and observational estimates. *J. Climate*, 11(1):72–87, 1998. → pages 9
- J. Wang, J. Zhang, E. Watanabe, M. Ikeda, K. Mizobata, J. E. Walsh, X. Bai, and B. Wu. Is the Dipole Anomaly a major driver to record lows in Arctic summer sea ice extent? *Geophys. Res. Lett.*, 36(5), 2009. → pages 4, 35, 36, 57, 58, 80
- M. Wang and J. E. Overland. A sea ice free summer arctic within 30 years? *Geophys. Res. Lett.*, 36(7), 2009. → pages 58
- E. Watanabe, J. Wang, A. Sumi, and H. Hasumi. Arctic dipole anomaly and its contribution to sea ice export from the Arctic Ocean in the 20th century. *Geophys. Res. Lett.*, 33(23), 2006. → pages 21, 35, 80
- A. J. Weaver, J. Marotzke, P. F. Cummins, and E. Sarachik. Stability and variability of the thermohaline circulation. *J. Phys. Oceanogr.*, 23(1):39–60, 1993. → pages 1, 6
- D. White, L. Hinzman, L. Alessa, J. Cassano, M. Chambers, K. Falkner, J. Francis, W. J. Gutowski, M. Holland, R. M. Holmes, et al. The Arctic freshwater system: Changes and impacts. *J. Geophys. Res.: Biogeosciences*, 112(G4), 2007. → pages 5
- R. Woodgate. Hydrographic cruise 32PZ20020819, 2002, Clivar & Carbon Hydrographic Data Office (CCHDO). Accessed 2015/07/03. <https://cchdo.ucsd.edu/cruise/32PZ20020819>, 2015. → pages 18
- R. A. Woodgate and K. Aagaard. Revising the Bering Strait freshwater flux into the Arctic Ocean. *Geophys. Res. Lett.*, 32(2), 2005. → pages 5
- B. Wu, J. Wang, and J. E. Walsh. Dipole anomaly in the winter Arctic atmosphere and its association with sea ice motion. *J. Climate*, 19(2):210–225, 2006. → pages 21, 35, 36, 54, 80
- P. Wu, R. Wood, and P. Stott. Human influence on increasing Arctic river discharges. *Geophys. Res. Lett.*, 32(2), 2005. → pages 9
- H. Xianmin. ANHA4 simulation table. Accessed 2016/11/08. <http://knossos.eas.ualberta.ca/xianmin/anha/anhatable.html>, 2016. → pages 17
- M. Yamamoto-Kawai, N. Tanaka, and S. Pivovarov. Freshwater and brine behaviors in the Arctic Ocean deduced from historical data of $\delta^{18}\text{O}$ and alkalinity (1929–2002 ad). *J. Geophys. Res.: Oceans (1978–2012)*, 110(C10), 2005. → pages 1, 3, 9, 16
- M. Yamamoto-Kawai, E. Carmack, and F. McLaughlin. Nitrogen balance and Arctic throughflow. *Nature*, 443(7107):43–43, 2006. → pages 6
- M. Yamamoto-Kawai, F. A. McLaughlin, E. C. Carmack, S. Nishino, and K. Shimada. Freshwater budget of the Canada Basin, Arctic Ocean, from salinity, $\delta^{18}\text{O}$, and nutrients. *J. Geophys. Res.: Oceans (1978–2012)*, 113(C1), 2008. → pages 1, 9, 15, 16, 54
- J. Zhang, R. Letolle, J. M. Martin, C. Jusserand, and J. M. Mouchel. Stable Oxygen isotope distribution in the Huanghe (Yellow River) and the Changjiang (Yangtze River) estuarine systems. *Cont. Shelf Res.*, 10(4):369–384, 1990. → pages 8

- X. Zhang, M. Ikeda, and J. E. Walsh. Arctic sea ice and freshwater changes driven by the atmospheric leading mode in a coupled sea ice-ocean model. *J. Climate*, 16(13):2159–2177, 2003. → pages 9, 45
- K. Zickfeld, A. Levermann, M. G. Morgan, T. Kuhlbrodt, S. Rahmstorf, and D. W. Keith. Expert judgements on the response of the Atlantic meridional overturning circulation to climate change. *Climatic Change*, 82(3-4):235–265, 2007. → pages 6

Appendix A

Climatology fields of the physical model

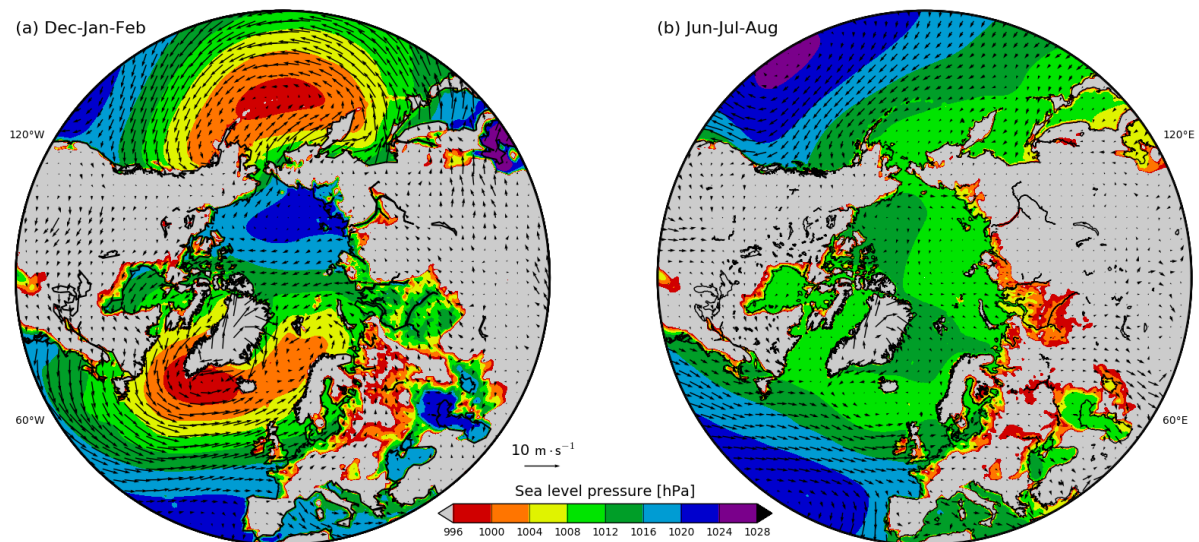


Figure A.1: CGRF 2002-2013 mean winter (DJF) and summer (JJA) sea level pressure and 10m-wind.

The winter mean of CGRF sea level pressure over the north hemisphere correctly shows the location of the Icelandic Low and the Aleutian Low with cyclonic 10m-wind (figure A.1, a). In the central Arctic a strong Beaufort high can be characterized by the 1020hPa isoline as the northward extension of the Siberian High. The summer mean CGRF sea level pressure has lower pressure gradients in the north hemisphere with a weak Icelandic Low (figure A.1, b). The Aleutian Low disappears and the central Arctic is covered by a weak anticyclonic wind pattern.

The 12-year mean ANHA4-EXH005 sea surface height is in general less than zero in the Arctic (figure A.2, a). The sea surface height on the North American side of the Arctic is higher than on the Eurasian side of the Arctic. Sea surface height maxima can be found in the Bering Strait and the Beaufort Sea meanwhile the East and South Greenland Seas have sea surface height minima. The 0-130m averaged ANHA4 ocean velocities follow the sea surface height isolines and show the TDS and

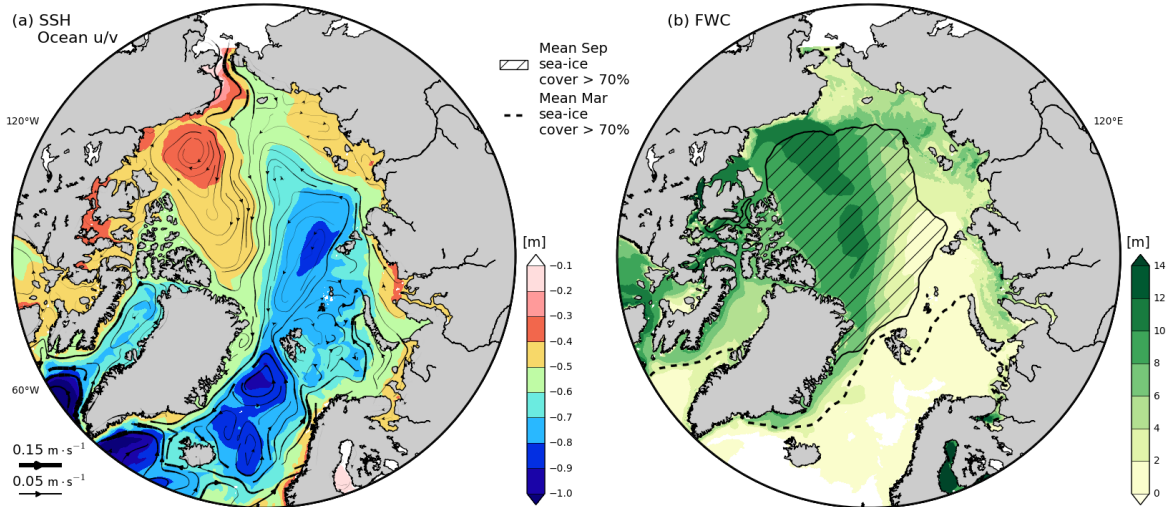


Figure A.2: ANHA4-EXH005 2002-2013 mean sea surface height, ocean velocities (a) and FWC relative to the 34.8 salinity (b) above 130m. The dashed line in (b) is the isoline of 2002-2013 mean March sea-ice larger than 70%; the hatch is the mean September sea-ice larger than 70%.

the Beaufort Gyre. Other major currents including the Labrador Sea current in the Baffin Bay, the West Spitsbergen Current near the Svalbard and the Bering Strait inflow are also reproduced.

The climatology of ANHA4-EXH005 FWC shows similar distributions as the sea surface height, with high FWC on the North American side and low FWC on the Eurasian side of the Arctic (figure A.2, b). The high FWC along the Eurasian marginal coast indicates the contribution of the Eurasian rivers and the zero FWC in the Barents Sea and the Greenland Sea means that the salinity above 130m is equal or higher than the 34.8 reference. By comparing the regions with mean sea-ice cover larger than 70% in March and September, significant ice loss can be seen in the Eurasian continental shelves, the Chukchi Sea and part of the Beaufort Shelf. Since September is the sea-ice minima, the sea-ice cover in this month also represents the semi-permanent sea-ice covered region.

Appendix B

Statistical methods

This appendix contains information about the statistical methods which were used in the research. Other calculations (average, weighted average, anomaly, normalization etc.) are assumed known and not documented.

B.1 Correlation

In this research, all correlations between two variables, \mathbf{X} and \mathbf{Y} , were calculated as the traditional ‘‘Pearson product-moment correlation’’:

$$R = \frac{E[(\mathbf{X} - \bar{\mathbf{X}})(\mathbf{Y} - \bar{\mathbf{Y}})^T]}{\sqrt{E(\mathbf{X}^2) - E(\bar{\mathbf{X}})^2} \sqrt{E(\mathbf{Y}^2) - E(\bar{\mathbf{Y}})^2}} \quad (\text{B.1})$$

Here E means expectation and overline means average. t-statistics can be applied to test the significance of R with the null case that \mathbf{X} and \mathbf{Y} have zero correlation.

$$T = R \sqrt{\frac{N}{1 - R^2}} \quad (\text{B.2})$$

Here N is the degree of freedom. A traditional estimate of N is $n - 2$. However for the time series with strong autocorrelations, $n - 2$ is over optimistic, so in this research, N is estimated based on the effective sample size (n^*) [Hsieh, 2009]:

$$n^* = n \left[\sum_{l=-L}^L (\rho_{xx}^l \rho_{yy}^l + \rho_{xy}^l \rho_{yx}^l) \right]^{-1} \quad (\text{B.3})$$

Here ρ_{xx}^l and ρ_{yy}^l are l -lagged autocorrelations of \mathbf{X} and \mathbf{Y} . ρ_{xy}^l and ρ_{yx}^l are cross-correlations. L is the maximum lag which usually can be no larger than $n/3$, in this research, $L = n/4$. The critical value of T is obtained from the Student’s t-distribution with $n^* - 2$ degrees of freedom and $1 - \alpha$ significance. The null case can be rejected if $|T|$ is larger than the critical value:

$$t_{\alpha/2, N} \leq |T| \quad (\text{B.4})$$

B.2 Composite anomaly

Composite anomaly means the difference of the average of a variable in the high and low phases of a timeseries (t). In this research, composite anomaly was applied to examine the correspond change of CGRF, ANHA4 variables and modeled tracers in three EOF mode PCs. The criteria for the high and low phase is the standard deviation of the timeseries (σ).

$$X = \bar{X}_i - \bar{X}_j, \quad \begin{array}{l} i \in \{t, t > \sigma_i\} \\ j \in \{t, t < -\sigma_i\} \end{array} \quad (\text{B.5})$$

The two-sample t-test examines if the mean of the two phases are equal. The null case of the t-test is the two phases are the same (high phase and low phase have no statistical difference), the t-statistics is given as:

$$T = \frac{\bar{X}_i - \bar{X}_j}{\sqrt{S_1^2/N_1 + S_2^2/N_2}} \quad (\text{B.6})$$

Here N is the degrees of freedom and assumed to be the sample size (n). The critical value of T is obtained by Student's t-distribution with $n - 2$ degree of freedom and $1 - \alpha$ significance. The null case can be rejected if $|T|$ is larger than the critical value:

$$t_{\alpha/2, n-2} \leq |T| \quad (\text{B.7})$$

B.3 Linear regression and trends

In this research, linear regression was used to investigate the trend of ANHA4 variables, modeled tracers and AO indices. In all the cases, the regression was done by least squares method.

B.3.1 Least squares method

Assuming independent variable x and dependent variable y with sample size n , the linear regression model is given as follows:

$$y = kx + b + \varepsilon \quad (\text{B.8})$$

Least squares method calculates trend k and offset b to make the square sum of the error [equation (B.9)] reach the global minimum.

$$R^2 = \sum_{i=1}^n (y_i - kx_i - b)^2 \quad (\text{B.9})$$

Since R^2 is a function of k and b , its extremum is where the partial derivative equals zero:

$$\begin{cases} \frac{\partial R^2}{\partial k} = 0 \\ \frac{\partial R^2}{\partial b} = 0 \end{cases} \Rightarrow \begin{cases} nk + b \sum_{i=1}^n x_i = \sum_{i=1}^n y_i \\ k \sum_{i=1}^n x_i + b \sum_{i=1}^n x_i^2 = \sum_{i=1}^n x_i y_i \end{cases} \quad (\text{B.10})$$

k and b can therefore be solved as equation (B.11) shows.

$$b = \frac{\bar{y} \left(\sum_{i=1}^n x_i^2 \right) - \bar{x} \left(\sum_{i=1}^n x_i y_i \right)}{\sum_{i=1}^n x_i^2 - n\bar{x}^2} \quad k = \frac{\left(\sum_{i=1}^n x_i y_i \right) - n\bar{x}\bar{y}}{\sum_{i=1}^n x_i^2 - n\bar{x}^2} \quad (\text{B.11})$$

B.3.2 Significance test

Student's t test can be used to examine the regression parameters and Fisher's F test can be used for testing the general fitness of the regression. In this research, the objectiveness of the linear regression is calculating the trend, hence only t-test for the trend was applied.

The null case of the t-test is: the true slope of x , k_0 is zero (no linear relation), and the t-statistics is:

$$T = (k - k_0) \sqrt{\frac{(n-2) \sum_{i=1}^n (x_i - \bar{x})^2}{\sum_{i=1}^n (y_i - \bar{y})^2}} \quad (\text{B.12})$$

Here k is the slope calculated by least square method. The critical value of T is obtained by the Student's t-distribution with $n - 2$ degrees of freedom and $1 - \alpha$ significance. The null case can be rejected if $|T|$ is larger than the critical value:

$$t_{\alpha/2, n-2} \leq |T| \quad (\text{B.13})$$

B.4 Empirical Orthogonal Function (EOF)

EOF is a data analysis method that extracts important patterns from the input. In this research, EOF is used for investigating the variability of FWC and to calculate AO and NAO indices (see appendix D).

B.4.1 Spatial pattern and principal component

This section briefly summarizes the idea of EOF and procedures for calculating the spatial pattern and Principal Component (PC) of EOF modes. The math derivation here is abbreviated and detailed discussion can be seen in Lorenz [1956] and other text books.

Assuming anomaly data \mathbf{X} is distributed over m different grids and n different times. It can be written as vectors:

$$\mathbf{X}_t = \begin{bmatrix} x_{1t} \\ x_{2t} \\ \vdots \\ x_{mt} \end{bmatrix}, t = 1, 2, \dots, n \quad (\text{B.14})$$

If we define m different grids as m dimensions, \mathbf{X}_t can then be expressed by m different orthogonal base vectors (\mathbf{V}_k):

$$\mathbf{X}_t = \sum_{k=1}^m \alpha_k(t) \mathbf{V}_k \quad (\text{B.15})$$

However, the relative importance of these base vectors is not the same, since the projections of \mathbf{X}_t onto \mathbf{V}_k , the weighting parameters $\alpha_k(t)$ are not the same. Hence, some base vectors may explain the majority of \mathbf{X}_t , but some contribute little. In an extreme example, if $\alpha'_k(t) = 0$, then \mathbf{V}'_k can be totally ignored. The goal of EOF analysis is to choose base vectors which explain the highest variation of \mathbf{X}_t , reduce the dimensionality of the system and identify important patterns.

In case of the first mode, equation (B.15) can be written with an error term:

$$\mathbf{X}_t = \alpha_1(t) \mathbf{V}_1 + \boldsymbol{\varepsilon}_t \quad (\text{B.16})$$

The first base vector satisfies the condition that the expectation of the variance of error reaches its global minimum:

$$E_1 = \frac{1}{n} \sum_{t=1}^n \boldsymbol{\varepsilon}_t^T \boldsymbol{\varepsilon}_t = \overline{\boldsymbol{\varepsilon}_t^T \boldsymbol{\varepsilon}_t} \quad (\text{B.17})$$

By using the method of Lagrange multipliers with constant λ , equation (B.17) changes into:

$$\begin{aligned} F(\mathbf{V}_1) &= E_1(\mathbf{V}_1) + \lambda_1 (\mathbf{V}_1^T \mathbf{V}_1 - 1) \\ \frac{\partial F}{\partial \mathbf{V}_1} &= -2E(\mathbf{X}_t \mathbf{X}_t^T) \mathbf{V}_1 + 2\lambda_1 \mathbf{V}_1 = 0 \end{aligned} \quad (\text{B.18})$$

Since \mathbf{X} is anomaly field, $E(\mathbf{X}_t \mathbf{X}_t^T)$ is known as the covariance matrix ($\boldsymbol{\Sigma}$). The solution of equation (B.18) is an eigenvalue problem:

$$\boldsymbol{\Sigma} \mathbf{V}_1 = \lambda_1 \mathbf{V}_1 \quad (\text{B.19})$$

It can be proven that E_1 reaches a global minimum with the highest eigenvalue λ_1 . Then, the mode one spatial pattern is the eigenvector (\mathbf{V}_1), the PC at time t is $\mathbf{X}_t^T \mathbf{V}_1$ and the eigenvalue (λ_1) indicates the relative importance of the mode one.

When it calculates the EOF mode two, the contribution of mode one will be removed from equation (B.15), so on for the other modes.

Due to the property of eigenvalues, the spatial pattern and PC can change signs and multiply with constants. In this research, $\alpha(t)$ is normalized and \mathbf{V} contains the magnitude, that is, it is multiplied by the standard deviation of \mathbf{X} .

B.4.2 Explained variance

The total variance of the original data \mathbf{X} is the trace of its covariance matrix $\mathbf{\Sigma}$. As a real-symmetric matrix, the trace of $\mathbf{\Sigma}$ equals to the sum of its eigenvalues:

$$\text{Tr}\mathbf{\Sigma} = \sum_{k=1}^m \lambda_k \quad (\text{B.20})$$

The explained variance of i th mode is the ratio of its eigenvalue to the sum of all eigenvalues:

$$\lambda_i \left(\sum_{k=1}^m \lambda_k \right)^{-1} \quad (\text{B.21})$$

The accumulated contribution of the first I modes is the sum of their explained variance:

$$\sum_{k=1}^I \lambda_k \left(\sum_{k=1}^m \lambda_k \right)^{-1} \quad (\text{B.22})$$

B.4.3 Rule of thumb

The rule of thumb [North et al., 1982] can be used to investigate the sampling error of EOF modes:

$$\delta\lambda_k = \lambda_k \sqrt{\frac{2}{N}} \quad (\text{B.23})$$

According to the rule, two neighboring modes are considered to be well separated if their difference is larger than the sampling error:

$$\lambda_k - \lambda_{k+1} > \delta\lambda_k \quad (\text{B.24})$$

The N in equation (B.23) is the sample number (n) in [North et al., 1982], but other research suggests that, it is better to have N as the effective degrees of freedom (N^*). In this research, N^* is calculated as Bretherton et al. [1999] suggested:

$$N^* = \left(\sum_{k=1}^n \lambda_k \right)^2 / \sum_{k=1}^n \lambda_k^2 \quad (\text{B.25})$$

Bretherton et al. [1999] also proved that, if eigenvalues drop down geometrically, then the accumulated contribution of first N^* modes should be roughly 86% (may have small uncertainty since N^* can be a non-integer). Also note that, Rule of thumb examines the “separation” of neighboring modes, if two modes do not pass the test, then they are not well separated, but they can still have physical explanations.

B.4.4 Spectral analysis

Power spectrum also known as Power Spectral Density (PSD) is power values of a signal as a function of frequency. In this research, power spectrum was calculated for the PCs of EOF modes to examine the frequency band of their major variabilities. A Fast Fourier Transform (FFT) based “periodogram” technique was applied for the estimation of power spectrum.

Suppose signal t is sampled at n different times, with a uniform spacing of Δt , then the power spectrum of t can be roughly represented by its periodogram, which is the square of the magnitude of the signal’s FFT:

$$G(f) = \frac{\delta t}{n} \left| \sum_{k=0}^{n-1} x_k e^{-i2\pi k \delta t f} \right|^2, \quad f < \frac{1}{2\Delta t} \quad (\text{B.26})$$

Here G is the periodogram, frequency f should be lower than the Nyquist frequency $1/2\Delta t$. Different from typical signal processing problems, here Δt is one month, and the unit of frequency is “cycles per month”.

Since the spectral powers of random processes are not strictly zero, a test should be made for investigating the significance of the periodogram. The null case of the test is the time series t is a noise signal. The type of noise includes “white noise” and “red noise”. White noise follows zero mean normal distribution and red noise is the first order Auto-Regressive (AR) process. The statistics of the two noise types obey the χ^2 distribution with N^* degrees of freedom.

$$\chi_w^2 = N^* \frac{G(f_k)}{G(f)}, \quad N^* = 2n \quad (\text{B.27})$$

$$\chi_r^2 = N^* \frac{G(f_k)}{G(f)L}, \quad L = \frac{1 - \rho_1^2}{1 + \rho_1^2 - 2\rho_1 \cos(2f_k\pi)} \quad (\text{B.28})$$

Here L is the standard red noise spectrum [Gilman et al., 1963]. $\overline{G(f)}$ is the mean of spectral power in the interval $[f_1, f_m]$, f_k means k ’s frequency, ρ_1 is the 1st-lagged autocovariance of t . In this research, since PCs are standardized timeseries, ρ_1 is also the lag-one autocorrelation. When testing the entire spectrum, χ^2 -statistics have n different values. If for frequency f_k , χ^2 -statistics is larger than $\chi^2(\alpha, N^*)$, the null case will be rejected, $G(f_k)$ has $1 - \alpha$ significance.

Periodogram has spectral leakage due to numeric operations. Smoothing or using window functions (e.g. Bartlett’s method, Welch’s Method) can partially reduce the leakage [Stoica and Moses, 1997], but since the power spectrum in this research is only calculated for qualitative analysis (e.g. which frequency band has the highest spectral power), no adjustment has been made.

Appendix C

The derivation of wind stress curl

In a spherical coordinate system with radius ($R\hat{r}$), zenith angle (ϕ) and azimuthal angle (θ), the radial component of the curl of a vector \vec{F} is:

$$\text{curlz}(\vec{F}) = \nabla \times \vec{F} \cdot \hat{r} = \frac{1}{R \sin \phi} \left[\frac{\partial}{\partial \phi} (F_\theta \sin \phi) - \frac{\partial F_\phi}{\partial \theta} \right] \quad (\text{C.1})$$

The zenith and azimuthal angles can be converted into latitude (φ) and longitude (λ):

$$\varphi = \frac{\pi}{2} - \phi, \quad \lambda = \theta \quad (\text{C.2})$$

Then the curl equation can be rewritten as:

$$\text{curlz}(\vec{F}) = \frac{1}{R \cos \varphi} \left(F_\lambda \sin \varphi - \frac{\partial F_\lambda}{\partial \varphi} \cos \varphi + \frac{\partial F_\varphi}{\partial \lambda} \right) \quad (\text{C.3})$$

The curl can be discretized with grid spacing ($\Delta x, \Delta y$), and equation (C.3) can be rewritten as follows:

$$\text{curlz}(\vec{F}) = \frac{\Delta F_\varphi}{\Delta x} - \frac{\Delta F_\lambda}{\Delta y} + \frac{F_\lambda}{R} \tan \varphi \quad (\text{C.4})$$

Appendix D

Atmospheric tele-connection patterns and CGRF indices

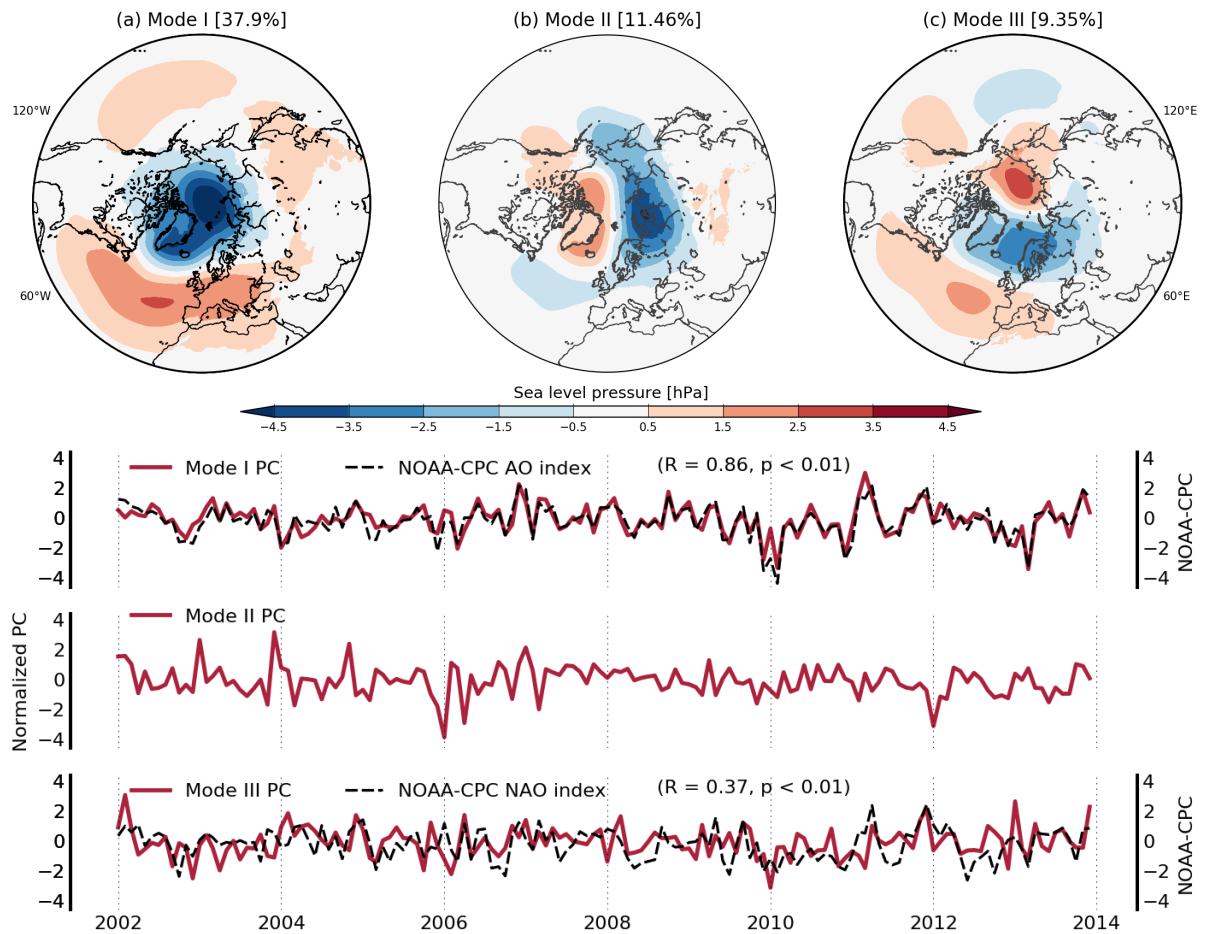


Figure D.1: Spatial patterns of sea level pressure EOF modes (a-c), timeseries in dark red are the PCs. NOAA-CPC AO and NAO indices were plotted as black dashed lines.

An EOF decomposition was applied to the CGRF sea level pressure from 20°N to 90°N (figure D.1). Mode one accounts for 37.9% of the total variance and its spatial distribution shows an annular distribution with negative sea level pressure anomaly in the Arctic and positive sea level pressure anomaly in the mid-latitudes, consistent with the definition of AO [Thompson and Wallace, 1998]. The PC of mode one has a significant positive correlation ($R = 0.86$, $p < 0.01$) with the NOAA-CPC AO index, which was calculated based on the NCEP-NCAR 1000hPa geo-potential height anomalies from 1948 to the present.

Mode two accounts for 11.46% of the total variance and its spatial pattern shows negative sea level pressure anomaly above the Eurasian side of the Arctic and positive anomaly above the North American side of the Arctic with strong meridionality above the TDS region. This spatial distribution is consistent with the description of the dipole anomaly [Wang et al., 2009, Watanabe et al., 2006, Wu et al., 2006] and is independent from the other atmospheric teleconnections.

Mode three accounts for 9.35% of the total variance with positive sea level pressure anomalies in both the North Atlantic and the Pacific side of the Arctic and with a negative sea level pressure anomaly centered in the Greenland Sea, consistent with the definition of NAO near the surface [Hurrell, 1995]. The PC of the mode three has a significant correlation with the NOAA-CPC NAO index ($R = 0.37$, $p < 0.01$), the latter was estimated from the standardized 500hPa Geo-potential height from 1948 to the present.